UNIVERSITÀ DEGLI STUDI FIRENZE

PhD in
Physics and Astronomy

CYCLE XXXVIII

COORDINATOR Prof. Giovanni Modugno

Development of a Spatial Light Modulator-based test-bed for sequential simulation of wide field adaptive optics systems:

Toward the validation of MORFEO's reconstruction and control algorithms

Academic Discipline (SSD) FIS/05

Doctoral Candidate
Dr. Bellone de Grecis Edoardo

Supervisor
Prof. Busoni Lorenzo

Coordinator
Prof. Giovanni Modugno

Academic Years 2022/2025

Abstract

Ground-based astronomical observations in the visible and near-infrared are limited by atmospheric turbulence, which can be compensated using Adaptive Optics (AO) systems. The effect of the turbulence on observations increases with the telescope diameter, making compensation crucial for current 8-m and future 40-m class telescopes. The *European Extremely Large Telescope* (ELT) will rely on the *Multi-conjugate adaptive Optics Relay For ELT Observations* (MORFEO) to address this challenge. However, MORFEO faces new and challenging issues, that need to be tested and prototyped before its integration and troubleshooting on sky. Furthermore, realising a realistic telescope simulator for ELTs is complex due to optical constraints, requiring the development of simplified test-beds to assess the performance and critical aspects of the upcoming AO facilities. In this context, this work was aimed at developing a test-bed that reduces complexity and still allow to assess the performance and critical aspects of MORFEO reconstruction and control algorithms. To do so, we broke down the complex Multi-Conjugate AO (MCAO) process into a simpler, sequentially executed Single-Conjugate AO (SCAO) test-bed. This hybrid approach of using hardware alongside simulation enables a reliable system validation by addressing problems close to those in the real system (like wavefront sensor noise, alignment, and sensor imperfections), compared to pure end-to-end simulations. To reproduce the atmospheric disturbance and compensation on our test-bench, we used a 1920×1152 XY Phase Series Spatial Light Modulator (SLM) manufactured by Meadowlark Optics. The high spatial resolution makes the SLM a promising phase modulator for reproducing atmospheric phase screens on ELT's complex pupil in our laboratory test-bed. However, such devices are known to have limitations that prevents from a full phase modulation. Thus, a careful characterisation of the SLM is required to quantify its impact on the sequentially executed MCAO loop. This project established a solid experimental reference, needed for the testing MORFEO's control and reconstruction strategies, defining a road map for hardware-in-the-loop simulations.

Contents

Introduction

Atmospheric turbulence is one of the main limitations affecting ground-based astronomical observations in the visible (VIS) and near-infrared (NIR). It causes spatial and temporal fluctuations in the atmospheric refractive index that introduce aberrations in the wavefront of the electromagnetic field we receive from the astronomical source. The result is a loss of angular resolution in the acquired images, making them seeing-limited rather than diffraction-limited. At a fixed wavelength, the effect of the turbulence on observations increases with the telescope diameter, making compensation crucial for current 8-m and future 40-m class telescopes. Adaptive Optics (AO) is a widely used technique to compensate for atmospheric turbulence and restore the image quality close to the diffraction limit of the telescope. AO systems consist in a wavefront sensor (WFS), to measure the wavefront distortions in the direction of reference stars (Guide Star, GSs), and a wavefront corrector, typically a deformable mirror (DM), to perform real-time compensation of the sensed aberrations.[1]

The most commonly used AO system in current observatories is the Single-Conjugate Adaptive Optics (SCAO) system: it is the simplest AO configuration with only a single guide star, wavefront sensor and deformable mirror. Such a system provides high correction performance within a narrow field of view ($\sim \pm 3\, arcsec$, in the VIS and $\sim \pm 20\, arcsec$ in the NIR), as long as the GS is close to the science target. However, the performance of SCAO systems are limited by the *anisoplanatism* effect, which leads to the deterioration of the correction as the angular separation between the science target and the GS increases. This is because the correction applied to the GS is also applied in all directions of the field of view, while wavefronts coming from different direction of the field of view pass through distinct regions of atmospheric turbulence than those encountered by the GS and measured by the WFS. As a result, the Point Spread Function (PSF) shows an elongated shape along the direction of the GS, resulting in an non-uniform correction on a wider field of view. [2]

To overcome the *anisoplanatism* effect and provide a uniform correction in a wider field of view, Multi-Conjugate Adaptive Optics (MCAO) systems have been developed. Such systems rely on multiple DMs conjugated at different altitudes to compensate the atmospheric turbulent volume, while the sensing and tomographic reconstruction of the turbulence is performed by multiple GSs with associated WFSs. MCAO systems provide uniform correction with diffraction-limited images over a wide field of view ($\sim 1' \times 1'$). [3]

The upcoming *Multi-conjugate adaptive Optics Relay For ELT Observations* (MORFEO) [4] is a post-focal AO module for ESO's 40-m Extremely Large Telescope (ELT) [5]. MORFEO is designed to support the NIR spectro-imager MICADO

[6], available on the first light, and a second instrument to be defined, providing a diffraction-limited correction over a field of view of $\simeq$1 *arcmin*, in a wide range of atmospheric conditions. MORFEO has recently passed the final phase design and it will use 12 WFSs and 3 DMs. For the tomographic sensing, the WFSs can simultaneously observe up to 6 Laser Guide Stars (LGS) and 3 Natural Guide Stars (NGS); while wavefront correction is performed by the ELT's adaptive M4, conjugated at 600 m, and 2 post-focal DMs, conjugated at 6 and 18 km, respectively. MORFEO is being developed by an European consortium led by INAF (the Italian National Institute for Astrophysics), with the Arcetri Astrophysical Observatory in Florence playing a major role in its design and implementation. [7]

However, the complexity of such a system introduces significant challenges, especially in designing and validating reconstruction and control algorithms. One major limitation of MCAO systems is represented by *unseen modes* [8], where wavefronts from different atmospheric layers cancel each other out in the direction of the WFSs (resulting in no correction), but not in the direction of the science camera, leading to a degradation of the image quality. To overcome this problem, MORFEO will implement a Minimum-Mean-Square-Estimator (MMSE) tomographic reconstructor [9], based on an *a priori* estimation of turbulence and noise statistics, which will be included in a Pseudo-Open Loop Control (POLC) [10]. To date, few MCAO systems, like GEMS [11], are operational on sky, relying on similar reconstruction strategies [12].

Furthermore, developing realistic telescope simulators for MORFEO and any other next-generation AO-assisted instrument for extremely large telescopes (ELTs) is complex due to the optical constraints imposed by the Lagrange invariant. This principle sets a fundamental limitation on how telescope optics can be rescaled in a laboratory test-bench. For instance, MORFEO's technical field of view is $\sim$150 arcseconds over a 40 m pupil: if this system were scaled down to a 40 mm pupil, the equivalent field of view would be about 42 degrees, which is impractical to reproduce on an optical bench. As a result, it is challenging to create a fully accurate rescaled simulator for ELT AO systems.

For all these aspects, it is crucial to develop simplified test facilities that reduce complexity and still allow to assess the performance and critical aspects of the next AO facilities on ELTs, before their integration and troubleshooting on sky.

In this context, the present work is dedicated to the development of an Spatial Light Modulator-base test-bed that reduces complexity and still allows to assess the performance and critical aspects of MORFEO reconstruction and control algorithms. To do so, we break down the complex MCAO process into a simpler and sequentially executed SCAO test-bed, coupling end-to-end simulation to the real hardware in the loop. This project, in collaboration with the AO group of the Arcetri Astrophysical Observatory, is part of the MORFEO test facilities for the validation of its reconstruction and control algorithms. Recent advancements in Liquid Crystal on Silicon (LCoS) [13] devices have led to the widespread use of reflective phase-only nematic Spatial Light Modulators (SLMs) in AO applications. The high spatial resolution, with thousands of pixels, makes the SLM a promising phase modulator for reproducing atmospheric turbulence and compensation on ELT's complex pupil. This makes them valuable tools for testing and characterisation of upcoming AO facilities for ELTs in laboratory test-beds.

In Chapter 1, we provide a general overview of the fundamentals of adaptive optics for astronomical observations. Particularly, we describe the required steps and elements to measure and compensate for atmospheric disturbance, and restore diffraction-limited resolution. Finally, we discuss the classical and next generation of AO facilities, highlighting their benefits, differences and limitations in AO-assisted observations. To conclude, we provide a brief description of the MORFEO module and its critical and complex aspects in the reconstruction and control system.

In Chapter 2, we present the SLM-based optical testbed designed and developed with the aim to perform hybrid (hardware alongside simulations) wide field AO loops by means of a classical AO setup, to test MORFEO's reconstruction and control algorithms. Finally, we provide a description of the hardware equipment and software tools adopted for the present test facility.

In Chapter 3, we describe the methods and analysis performed to characterise the overall test-bench and its key elements. Particularly, we present the in-depth characterisation of the SLM, aimed to maximise its phase modulation response and quantify its intrinsic limitations and impacts in AO simulations. In addition, we show the analysis performed to characterise the SHWFS, to quantify its response and source of bias and noise. Furthermore, we quantify the static aberrations present on the testing setup, due to the residual misalignment and integration of the bench. Finally, we describe the configuration and calibration adopted to perform prototype AO loops simulations.

Finally, Chapter 4 provides a description of the test and loops performed to prototype the SLM-based test bench control loop, and validate the hardware alongside numerical simulations of the reproduced AO loop.

Chapter 1

Adaptive Optics for Astronomy

Even in the most suitable astronomical sites, ground-based astronomical observations in the visible (VIS) and Near-infrared (NIR) can be strongly limited by atmospheric turbulence. It locally causes random spatial and temporal fluctuations in the atmospheric refraction index, inducing distortions (i.e. aberrations) in the wavefront of the electromagnetic field that we receive from the astronomical source. This leads to the degradation of the telescope resolving power (image quality), resulting in blurry images on the acquired science target, setting challenging constraints on the scientific return.

The first idea for compensating for atmospheric turbulence was proposed by Babcock [14] in the 1950s, leading to the fundamental concepts of Adaptive Optics (AO) systems. These systems are aimed to recover the best image quality in an optical system affected by this kind of time-depending aberrations: the basic principle foresees a real time compensation of the wavefront distortion measured by a wavefront sensor (WFS) and corrected by means of a deformable mirror (DM); then a feedback control is used to update the DM's shape based on the temporal evolution of the atmospheric turbulence. After nearly forty years of technological advances, the first AO system for astronomy was finally realised [15], setting a new road map of ground-based astronomical VIS and NIR observations. Since then, multiple AO architectures have been explored and developed, enabling the restoration of angular resolution in increasingly larger and more complex telescopes. The next-generation of 40m telescope facilities will deliver a gain in the angular resolution of a factor ≈ 5 compared to the actual 8m-class telescopes at the same observing wavelength. This broadens the frontiers of scientific research, allowing astronomers to look at a deeper and sharper targets in the universe.

Several science cases drive the employment and development of the next generation of AO-assisted instruments. High-precision astrometry plays the main role among the science drivers. For instance, the Multi-AO Imaging CamerA for Deep Observations (MICADO) [6] on the Extremely Large Telescope (ELT) [5], will benefit from the Multi-conjugate adaptive Optics Relay For ELT Observations (MORFEO, formerly known as MAORY)[4], which will deliver diffraction-limited resolution over a wide field of ~ 1 arcmin. Moreover, Exoplanetary detection and characterisation play a significant role: current extreme-AO facilities, such as Spectro-Polarimetric High-contrast Exoplanet REsearch (SHPERE) [16] at the Very Large Telescope

(VLT) [17] and the upgraded Gemini Planet Imager (GPI 2.0) [18] at Gemini South [19], demonstrate the remarkable capabilities of the AO systems to provide high-contrast imaging, while the Mid-infrared ELT Imager and Spectrograph (METIS) [20] at ELT is aimed at extending this to the thermal-IR regime for direct imaging and atmospheric studies of exoplanets. Finally, spatially resolved spectroscopy of galaxies and star-forming regions will be detected by the High Angular Resolution Monolithic Optical and Near-infrared Integral field spectrograph (HARMONI) [21], which is a first-light integral-field spectrograph designed to exploit MORFEO's compensation.

In this chapter, we introduce the basic principles of AO in astronomical observations. In Sec.1.1, we describe the theory of statistics of turbulence-induced wavefront distortions. In Sec.1.2, we summarise the fundamentals of the classical AO system. Finally, in Sec.1.3, we introduce the concept of multi-conjugate AO (MCAO) and its difference with classical AO reconstruction, and providing a brief overview of the MORFEO module.

1.1 Atmospheric turbulence statistics

The optical turbulence represents a crucial role in the design of an AO system. In the following sections, we refer to [22], [23], and [24], where we describe the key elements for a statistical description of the atmospheric turbulence, introducing the main parameters used for its characterisation.

1.1.1 Distortions in the aberrated wavefront

The optical effects of atmospheric turbulence are caused by local thermodynamic variations of the air that produce fluctuations in the atmospheric layers' refractive index. These fluctuations are responsible for the aberrations introduced on a flat wavefront coming from an astronomical source that passes through the Earth's atmosphere.

In order to quantify the behaviour of the wavefront aberrations, we begin with a statistical description of air refractive index fluctuations, considering the difference between its value $n(\mathbf{r})$ at a point $\mathbf{r}$ and its value $n(\mathbf{r}+\boldsymbol{\rho})$ at a point with distance $\rho = |\boldsymbol{\rho}|$. From Tatarski [6], we define the variance of the difference between the two values as

$$D_n(\rho) = \left\langle |n(\mathbf{r}) - n(\mathbf{r}+\boldsymbol{\rho})|^2 \right\rangle = C_n^2 \, \rho^{2/3} \,, \tag{1.1}$$

where $D_n(\rho)$ is the index structure function and $\langle \cdot \rangle$ represents an ensemble average. As shown in Figure 1.1, C_n^2 represents the index structure coefficient and gives a measure of the local amount of inhomogeneities, which depends on the atmospheric altitude. As a first-order approximation, the process can be considered as homogeneous (i.e. it depends only on the separation ρ, not on the position $\mathbf{r}$) and isotropic (i.e. it depends on the modulus of the distance $\boldsymbol{\rho}$).

If we consider a monochromatic plane wave propagating through the atmosphere, the wavefront phase at the position $\boldsymbol{r}$ on a surface that is perpendicular to the propagation direction z can be described as follows:

$$\varphi(\boldsymbol{r}) = k \int n(\boldsymbol{r}, z)\, dz\,, \tag{1.2}$$

where k is the wave number $k = 2\pi/\lambda$ and λ is the wavelength.

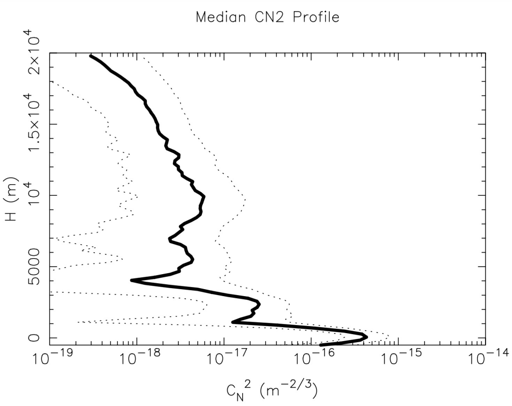

Figure 1.1. Example of median vertical profile of C_n^2 (solid line) on the Mt. Graham summit related to 43 nights, from Masciadri et al. [25]. The dotted lines are the first and third quartiles. The patterns as a function of the atmospheric altitude show that the major strength of the turbulence is located in the ground layers.

However, what we are really interested in is not the absolute value of the wavefront phase, but rather in its difference between a point x on a telescope's entrance aperture and a nearby point at a distance $\boldsymbol{\xi}$, with $\xi = |\boldsymbol{\xi}|$. Then, the variance of the difference is defined as the structure function of the phase and it can be expressed as:

$$D_\varphi(\xi) \;=\; \langle|\varphi(\boldsymbol{x}) - \varphi(\boldsymbol{x}+\boldsymbol{\xi})|^2\rangle \approx 2.91\, k^2 \int C_n^2(z)\, dz\; \xi^{5/3}\,, \tag{1.3}$$

where z is the distance along the propagation axis. Typically, the atmosphere is considered as a medium stratified made of parallel layers. Thus, C_n^2 is only a function of the height h from the ground and the Eq.(1.3) becomes:

$$D_\varphi(\xi) \approx 2.91\, k^2 (\cos\gamma)^{-1} \int C_n^2(h)\, dh\; \xi^{5/3}\,, \tag{1.4}$$

where γ is the angular distance of the source from zenith and $\cos(\gamma)^{-1}$ is the air mass.

The structure function of the phase can be described through a characteristic scale length called Fried parameter r_0, and written as:

$$D_\phi(\xi) \approx 6.88 \left(\frac{\xi}{r_0}\right)^{5/3}, \tag{1.5}$$

with

$$r_0 \approx \left[0.423\, k^2 (\cos\gamma)^{-1} \int C_n^2(h)\, dh\right]^{-3/5}. \tag{1.6}$$

The Fried parameter defines the typical size scale over which the turbulent wavefront is coherent. The smaller r_0 is, the stronger the turbulence. From Eq.(1.6), we want to stress that r_0 increases with the wavelength of the radiation ($r_0 \sim \lambda^{6/5}$) and with the airmass ($r_0 \sim cos\gamma^{3/5}$).

From Fried's parameter stems the usual definition of *seeing*, that is approximately the typical full-width half-maximum (FWHM) for a point source image affected by atmospheric turbulence:

$$\epsilon \simeq \frac{\lambda}{r_0}. \tag{1.7}$$

As an example, for a seeing value of $\epsilon = 1$ arcsec (typical of good astronomical sites), r_0 in the visible band V ($\lambda = 500$ nm) is about 10 cm, and about 50 cm in the near infrared K band ($\lambda = 2200$ nm). It is worth noting that, in the absence of atmospheric turbulence, a telescope with a pupil diameter D could reach an image quality at the diffraction-limit, corresponding to an image size of

$$\theta_{DL} \simeq \frac{\lambda}{D}. \tag{1.8}$$

Thus, diffraction and seeing effects set limits on ground-based telescopes' angular resolution, providing an effective resolution given by the following convolution:

$$\theta_{res} = \epsilon * \theta_{DL}. \tag{1.9}$$

However, since $r_0 \ll D$, the ratio between image size in seeing-limited conditions and in diffraction-limited conditions is D/r_0, that is, in the range 20-100 for current and future 8-40 m telescopes. This gives a quick idea about the importance of seeing compensation in order to recover ground-based telescopes' diffraction limit resolution and explains why adaptive optics is becoming an essential part of current and future instrumentation.

Related to r_0, there are two additional parameters used to characterise turbulence: the isoplanatic angle θ_0

$$\theta_0 \approx 0.057\, \lambda^{6/5} \cos^{8/5}\gamma \left[\int_0^\infty h^{5/3} C_n^2(h)\, dh\right]^{-3/5}, \tag{1.10}$$

that represents the Fried parameter r_0 but in an angular scale; and the coherence time τ_0

$$\tau_0 \approx 0.057\, \lambda^{6/5} \cos^{3/5}\gamma \left[\int_0^\infty |v(h)|^{5/3} C_n^2(h)\, dh\right]^{-3/5}, \tag{1.11}$$

that quantifies temporal correlation of the wavefront phase distortions introduced by the turbulence, where $v(h)$ is the wind speed at the altitude h. Eq.(1.11) can be also expressed as follows:

$$\tau_0 \approx 0.31\, \frac{r_0}{v_m}, \tag{1.12}$$

where v_m is the average wind speed defined as the following weighted mean:

$$v_m = \left[\frac{\int C_n^2(h)\, v(h)^{5/3}\, dh}{\int C_n^2(h)\, dh}\right]^{3/5}. \tag{1.13}$$

It is worth noting that the parameter r_0 weights equally the turbulence at all heights in the atmosphere, while θ_0 and τ_0 take into account the variations of turbulence and wind speed with height as well. Typical values are few arcseconds for θ_0 and few milliseconds for τ_0 in V band.

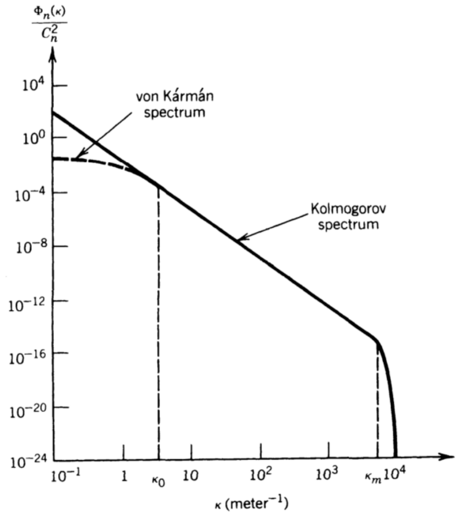

Figure 1.2. PSD models of the air refractive index fluctuations from Goodman [26]. The solid line is the Kolmogorov while the dashed line is Von Karman spectrum.

Kolmogorov provided the first mechanical structure of turbulence [27]. Its model assumes that energy is added to the system in the form of large-scale disturbances, the outer scale L_0. These then break down into smaller structures until they finally dissipate due to the air viscosity, stopping the turbulent power. Particularly, Kolmogorov describes the power spectral density (PSD) for the air refractive index fluctuations with the following:

$$\Phi_n(\kappa) \approx 0.033\, C_n^2\, \kappa^{-11/3}\,, \tag{1.14}$$

where Φ_n is the PSD of air refractive index fluctuations, κ is the spatial wavenumber $\kappa = 2\pi/l$, with l the scale size of turbulence. The spectrum is held within the inertial range for which $l \in (l_0, L_0)$, where L_0 and l_0 are the outer and inner scale of turbulence, respectively. For $l < l_0$ (i.e. $\kappa > \kappa_m$, with $\kappa_m = 2\pi/l_0$), the energy loss due to viscous forces results in a rapid drop in $\Phi_n(\kappa)$ was included by Tatarski [22], providing the new expression:

$$\Phi_n(\kappa) \approx 0.033\, C_n^2\, \kappa^{-11/3}\, e^{-\kappa^2/\kappa_m^2}\,, \tag{1.15}$$

where $\kappa_m = 2\pi/l_0$. However, Eq.(1.14) and Eq.(1.15) are not valid to model the spectrum of the index of refraction fluctuations for $\kappa \to 0$, due to the non-integrable pole at $\kappa = 0$. To get rid of this problem, an additional expression of the model, known as the Von Karman spectrum, is often assumed:

$$\Phi_n(\kappa) \approx \frac{0.033\, C_n^2}{\left(\kappa^2 + \kappa_0^2\right)^{11/6}}\, e^{-\kappa^2/\kappa_m^2}\,, \tag{1.16}$$

where $\kappa_0 = 2\pi/L_0$. Figure 1.2 shows the Kolmogorov and Von Karman PSD models.

After conversion factors, the following expression of the PSD of the wavefront phase distortions under the Kolmogorov model can be derived from Eq.(1.14):

$$\Phi_\phi(f) \approx 0.00969 \left(\frac{2\pi}{\lambda}\right)^2 C_n^2 \, f^{-11/3} \, , \tag{1.17}$$

where the spatial frequency $f = \kappa/2\pi$ has been considered.

Finally, the latter equation can be modified to derive the analogous expression of PSD of wavefront phase distortions under the Von Karman's model and written as:

$$\Phi_\phi(f) \approx 0.00969 \left(\frac{2\pi}{\lambda}\right)^2 C_n^2 \, (f^2 + f_0^2)^{-11/6} \, , \tag{1.18}$$

where $f_0 = \kappa_0/2\pi$.

1.1.2 Modal expansion of wavefront aberrations

Wavefront aberrations induced by atmospheric turbulence are commonly described through their expansion in a series of orthogonal functions. Zernike polynomials represents one of the main series (in AO often referred to as modal base) used to describe the wavefront distortions on a telescope pupil, due their mathematical properties. Although these polynomials are defined on an circular pupil, most optical telescopes have complex pupil geometries, due segmented mirrors, non-negligible central obscuration, and spiders. In that case, a more complex modal expansion of the wavefront (e.g., annular Zernike modes [28] and Karhunen–Loève modes [29][30]) is required. Hereafter, for clarity, we restricted the discussion to the unobstructed circular pupil. To note that in the following, the wavefront phase is expressed in units of radians and corresponding induced optical path difference, in meters, is given by:

$$OPD = \frac{\lambda}{2\pi} \, \phi \, . \tag{1.19}$$

Zernike polynomials Z_j are two-dimensional orthogonal functions defined on the unitary circle and, using polar coordinates (r, θ), can be used to represent the wavefront phase on an telescope circular pupil, without any obstruction. Hereafter, we adopt the Noll's notation [31] of these modal basis, that are defined as:

$$Z_j(r,\theta) = \begin{cases} \sqrt{n+1}\, R_n^m(r)\, \sqrt{2}\, \cos(m\theta), & j \text{ even}, \, m \neq 0 \\ \sqrt{n+1}\, R_n^m(r)\, \sqrt{2}\, \sin(m\theta), & j \text{ odd}, \, m \neq 0 \\ \sqrt{n+1}\, R_n^m(r), & m = 0 \, . \end{cases} \tag{1.20}$$

From the latter equation, we can note that each Zernike polynomial is defined by 3 indexes: the index j progressively counts the polynomials and every j is a function of 2 positive integers n and m that represent the radial and azimuthal degree of the polynomial, respectively. These 2 integers satisfy the following conditions:

$$\begin{matrix} m \leq n \\ n - |m| \;\; even \end{matrix} \quad .$$

Furthermore, the radial part $R_n^m(r)$ is given by

$$R_n^m(r) = \sum_{s=0}^{(n-m)/2} \frac{(-1)^s (n-s)!}{s![(n+m)/2-s]![(n-m)/2-s]!} r^{n-2s} \,. \tag{1.21}$$

Figure 1.3 and Figure 1.4 provide the ordering and a visual representation of the first 15 Zernike modes (from Z_1 to Z_{15}), respectively.

n ↓ / $m\rightarrow$	0	1	2	3	4
0	$Z_1 = 1$ Piston				
1		$Z_2 = 2r\cos\theta$ $Z_3 = 2r\sin\theta$ Tip/tilt			
2	$Z_4 = \sqrt{3}(2r^2-1)$ Defocus		$Z_5 = \sqrt{6}r^2\sin 2\theta$ $Z_6 = \sqrt{6}r^2\cos 2\theta$ Astigmatism (3rd order)		
3		$Z_7 = \sqrt{8}(3r^3-2r)\sin\theta$ $Z_8 = \sqrt{8}(3r^3-2r)\cos\theta$ Coma		$Z_9 = \sqrt{8}r^3\sin 3\theta$ $Z_{10} = \sqrt{8}r^3\cos 3\theta$ Trefoil	
4	$Z_{11} = \sqrt{5}(6r^4-6r^2+1)$ Spherical		$Z_{12} = \sqrt{10}(10r^4-3r^2)\cos 2\theta$ $Z_{13} = \sqrt{10}(10r^4-3r^2)\sin 2\theta$ Astigmatism (5th order)		$Z_{14} = \sqrt{10}r^4\cos 4\theta$ $Z_{15} = \sqrt{10}r^4\sin 4\theta$ Ashtray

Figure 1.3. Ordering table of Zernike polynomials from Noll [31]. Even values of j correspond to the symmetric modes defined by cos(mθ), while odd values correspond to the antisymmetric modes given by sin(mθ). For a given n, the modes with the lowest values of m are ordered first.

Using Eq.(1.20), the orthogonality on the unitary circle can be expressed as follows:

$$\int_0^{2\pi}\int_0^1 W(r)\, Z_j(r,\theta)\, Z_{j'}(r,\theta)\, r dr d\theta = \delta_{jj'} \tag{1.22}$$

where $\delta_{jj'}$ is Kronecker delta and $W(r)$ is the pupil function, defined as:

$$W(r) = \begin{cases} 1/\pi, & r \leq 1 \\ 0, & r > 1 \end{cases} \tag{1.23}$$

Furthermore, Fourier Transform (FT) of the Zernike polynomials are defined. If $Q_j(f,\phi)$ is the FT of $Z_j(r,\theta)$, such that:

$$W(r)\, Z_j(r,\theta) \;=\; \int d\boldsymbol{f}\; Q_j(f,\phi)\, e^{-2\pi i\,\boldsymbol{f}\cdot\boldsymbol{r}} \,, \tag{1.21}$$

using Eq.(1.20) the FT can be written as:

$$Q_j(f,\phi) \;=\; \sqrt{n+1}\,\frac{J_{n+1}(2\pi f)}{\pi f} \times \begin{cases} (-1)^{(n-m)/2}\, i^m\, \sqrt{2}\cos(m\varphi), & \text{even } j,\ m \neq 0, \\ (-1)^{(n-m)/2}\, i^m\, \sqrt{2}\sin(m\varphi), & \text{odd } j,\ m \neq 0, \\ (-1)^{n/2}, & m = 0\,. \end{cases} \tag{1.24}$$

where $J_l(x)$ is the l-th order Bessel function of the first kind.

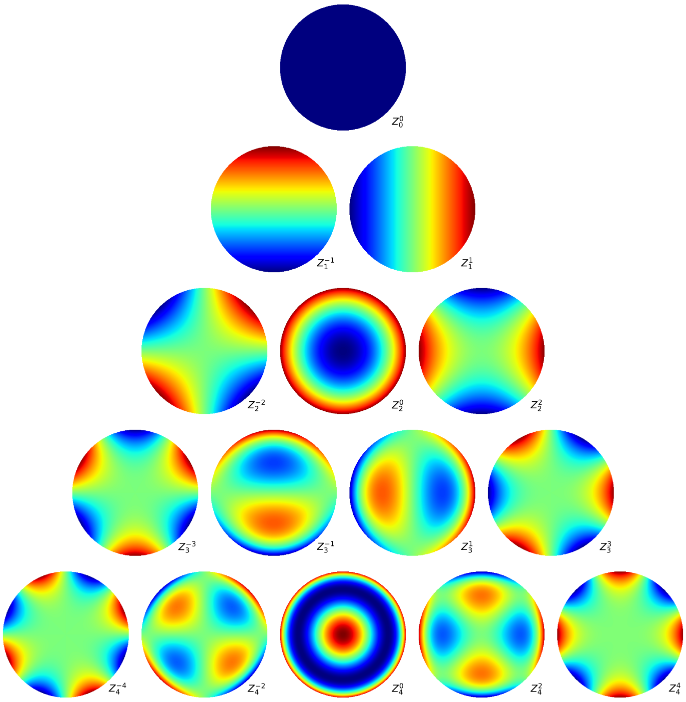

Figure 1.4. First 15 Zernike modes: the shown modes are the corresponding visual representation of the polynomials in Figure1.3. The polynomials are numerically computed using the python package ARTE, available on GitHub.

Any arbitrary wavefront on a circular aperture of a give radius R can be decomposed into a series Zernike polynomials. So, if $\phi(r, \theta)$ is an arbitrary function describing a wavefront phase, its zernike modal expansion over a circle of radius R is given by::

$$\phi(R\rho, \theta) = \sum_{j=1}^{\infty} a_j \, Z_j(\rho, \theta) \, . \tag{1.25}$$

with $\rho = r/R$ and where the expansion coefficients a_j are defined as:

$$a_j = \int_0^1 \int_0^{2\pi} W(r) \, \phi(R\rho, \theta) \, Z_j(\rho, \theta) \; d\boldsymbol{\rho} \, . \tag{1.26}$$

As we are dealing with random wavefront fluctuations, we describe the statistical properties of the Zernike polynomials. The covariance of the Zernike coefficient a_j can be expresed as:

$$\left\langle a_j^* \, a_{j'} \right\rangle = \int d\boldsymbol{\rho} \int d\boldsymbol{\rho}' \, W(\rho) \, W(\rho') \, Z_j(\rho, \theta) \, Z_{j'}(\rho', \theta') \, \langle \phi(R\rho) \, \phi(R\rho') \rangle \, . \tag{1.27}$$

where the coefficient a_j are considered as Gaussian random variables with zero mean. The latter equation can be written in the Fourier space as follows:

$$\left\langle a_j^* \, a_{j'} \right\rangle = \frac{1}{R^2} \iint d\boldsymbol{f} \, d\boldsymbol{f}' \; Q_j^*(f) \, \Phi(f/R, f'/R) \, Q_{j'}(f') \, \delta(f - f') \, , \tag{1.28}$$

where $\Phi(f)$ is given by Eq.(1.17). Using Eq.(1.17) in Eq.(1.28), the covariance of Zernike coefficients on a pupil of diameter D can be expressed as follows:

$$\left\langle a_j^* \, a_{j'} \right\rangle = c_{jj'} \left(\frac{D}{r_0}\right)^{5/3} . \tag{1.29}$$

where the analytic expression for the coefficients $c_{jj'}$ was derived by Noll [31] as follows:

$$c_{jj'} \simeq \frac{0.046}{2^{5/3}\pi} \sqrt{(n+1)(n'+1)} \, (-1)^{(n+n'-2n)/2} \, \delta_{mm'} \int df \; f^{-8/3} \, \frac{J_{n+1}(2\pi f) \, J_{n'+1}(2\pi f)}{f^2}, \tag{1.30}$$

and the integral is tabulated:

$$\int df \; f^{-8/3} \, \frac{J_{n+1}(2\pi k) \, J_{n'+1}(2\pi k)}{k^2} = \frac{\Gamma(-14/3) \, \Gamma\left(\frac{n+n'-14/3+3}{2}\right)}{2^{14/3} \, \Gamma\left(\frac{-n+n'+14/3+1}{2}\right) \, \Gamma\left(\frac{n-n'+14/3+1}{2}\right) \, \Gamma\left(\frac{n+n'+14/3+3}{2}\right)} \tag{1.31}$$

for $n \neq 0$, where $\Gamma(x)$ is the Euler Gamma function. The latter integral diverges for null values of n and n'. This means that the variance of a constant wavefront phase (in AO commonly referred as piston) diverges, under the assumption of an infinite outer scale L_0. Thus, Eq.(1.29) and Eq.(1.30) demonstrated that only Zernike terms with the same azimuthal degree show correlation. Figure 1.5 shows the variance of the Zernike coefficients as a function of the Zernike index j: its shows that low-order modes accounts for the most of the error, where the global Tilt (Z_2 and Z_3) contributes to the 87% of the variance.

Thus, the variance of the Zernike coefficients allows us to quantify the phase variance of the wavefront (i.e. the mean square wavefront phase fluctuation) as follows:

$$\sigma^2 = \left\langle \int W(r) \, \phi^2(r,\theta) \, d\boldsymbol{r} \right\rangle = \sum_{j=2} \left\langle a_j^2 \right\rangle . \tag{1.32}$$

The series in Eq.(1.32) excludes the piston term ($j = 1$), since we are interested in the deviation from the mean surface and, as seen, its variance diverges. Furthermore, the phase piston has no effect on the image formation and it does not represent any optical aberration.

As a consequence, for an ideal AO system designed to compensate for the first J modes, the corrected phase is given by:

$$\phi_C \; = \; \sum_{j=1}^{J} a_j \, Z_j \tag{1.33}$$

and the associated mean square residual error (reminding that $\langle a_j \rangle = 0$) is given by:

$$\sigma_J^2 = \int d\rho \, W(\rho) \, \left\langle [\phi(R\rho) - \phi_C(R\rho)]^2 \right\rangle = \left\langle \phi^2 \right\rangle - \sum_{j=1}^{J} \left\langle |a_j|^2 \right\rangle = \sum_{j=J+1}^{\infty} \left\langle a_j^2 \right\rangle . \tag{1.34}$$

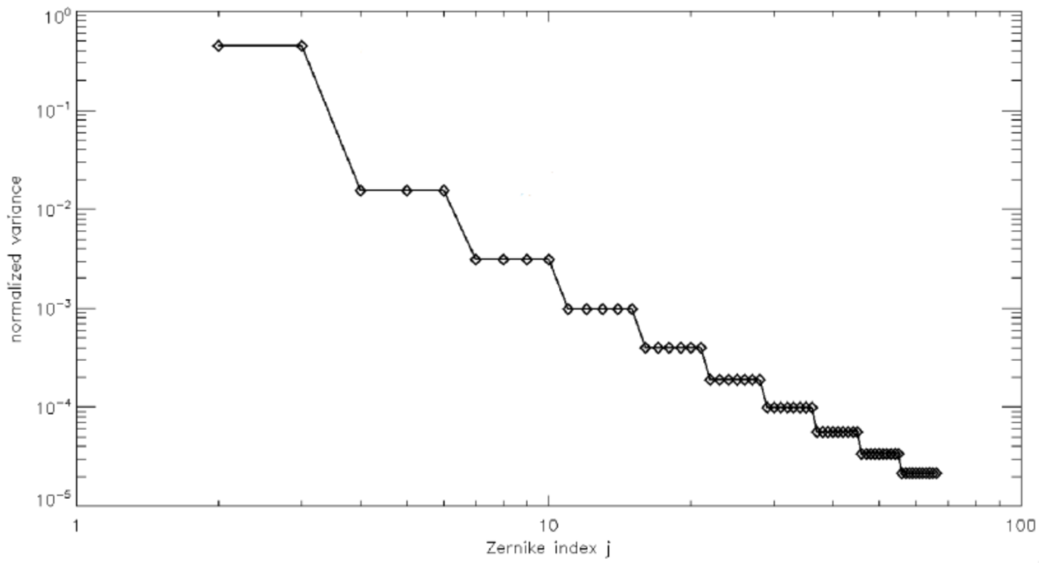

Figure 1.5. Variance of Zernike modes normalized to $(D/r_0)^{5/3}$ as a function of the Zernike Polynomial's index j. The plot shows that most of the atmospheric turbulence is concentrated in the first Zernike modes: about 87% of the total variance can be fitted by the Tip and Tilt modes, and the next radial order (focus and astigmatism) accounts for another 8%. The variance is computed assuming the Kolmogorov model of wavefront phase distortions. From [24]

.

The table in Figure 1.6 shows the values of the mean residual error.

In the table of the latter figure, Noll provides the following expression for the total variance in seeing-limited conditions over a pupil of diameter D:

$$\sigma_{SL}^2 = 1.0299(D/r_0)^{5/3}\,. \tag{1.35}$$

To quantify this variance, for an 8 m telescope with a 1 arcsec seeing in V band (r_0 = 10 cm), the total wavefront deformation is about 3 μm RMS. For an ELT (D = 40 m) in K band (r_0 = 50 cm) σ_{SL} is even larger, of the order of >10 μm RMS. Furthermore, Noll provides an approximate expression for larger values of J in the latter equation and is given by:

$$\sigma_J^2 = \sum_{j=J+1}^{\infty} \langle a_j^2 \rangle \simeq 0.2944 J^{-\sqrt{3}/2}(D/r_0)^{5/3}\,. \tag{1.36}$$

This expression gives a very rough idea about the number of modes that have to be corrected in an AO system to reach a given performance. As a rule of thumb, the image appears to be diffraction-limited (i.e. its size is $\theta_{DL} = \lambda/D$) when the residual wavefront deformation is about 1 rad RMS, i.e. $\lambda/2\pi$, a few hundreds nm RMS at the considered wavelengths in the examples above. To continue with the numerical examples, using Eq.(1.36), to obtain a residual of 1 rad for an 8-m telescope with r_0 = 10 cm in V-band one needs to correct about 1000 Zernike modes.

To conclude this section, Zernike Polynomials are a special set of orthonormal functions and are widely used in AO. Furthermore, this modal base is remarkably

$\Delta_1 = 1.0299\,(D/r_0)^{5/3}$	$\Delta_{12} = 0.0352\,(D/r_0)^{5/3}$
$\Delta_2 = 0.582\,(D/r_0)^{5/3}$	$\Delta_{13} = 0.0328\,(D/r_0)^{5/3}$
$\Delta_3 = 0.134\,(D/r_0)^{5/3}$	$\Delta_{14} = 0.0304\,(D/r_0)^{5/3}$
$\Delta_4 = 0.111\,(D/r_0)^{5/3}$	$\Delta_{15} = 0.0279\,(D/r_0)^{5/3}$
$\Delta_5 = 0.0880\,(D/r_0)^{5/3}$	$\Delta_{16} = 0.0267\,(D/r_0)^{5/3}$
$\Delta_6 = 0.0648\,(D/r_0)^{5/3}$	$\Delta_{17} = 0.0255\,(D/r_0)^{5/3}$
$\Delta_7 = 0.0587\,(D/r_0)^{5/3}$	$\Delta_{18} = 0.0243\,(D/r_0)^{5/3}$
$\Delta_8 = 0.0525\,(D/r_0)^{5/3}$	$\Delta_{19} = 0.0232\,(D/r_0)^{5/3}$
$\Delta_9 = 0.0463\,(D/r_0)^{5/3}$	$\Delta_{20} = 0.0220\,(D/r_0)^{5/3}$
$\Delta_{10} = 0.0401\,(D/r_0)^{5/3}$	$\Delta_{21} = 0.0208\,(D/r_0)^{5/3}$
$\Delta_{11} = 0.0377\,(D/r_0)^{5/3}$	
$\Delta_J \sim 0.2944\,J^{-\sqrt{3}/2}\,(D/r_0)^{5/3}$ (For large J)	

Figure 1.6. Mean square residual error when J modes are perfectly compensated. Δ_J corresponds to σ_J^2 of the Eq.(1.34). The table is taken from Noll [31].

notable as its low-order modes are directly related to the main aberrations of optical systems, such as out of focus, Tilt, astigmatism that can be introduced in the path because of misalignment in the instrument's optics. For instance, Z_2 is called *Tilt* as its only optical effect is to shift laterally the PSF, while Z_4 is called *defocus* because such a wavefront will produce a defocused image. However, despite their remarkable mathematical properties, Zernike modes have practical limitations in AO: high-order modes concentrate energy at high spatial frequencies and close to the edge of the pupil, resulting in residuals that cannot be fully compensated for by a phase corrector. Therefore, in practice, a Karhunen–Loève (KL) basis [32] is preferred. This is optimised for the turbulence statistics and the geometry and implementation of the phase compensator.

1.1.3 Temporal spectrum of wavefront aberrations

To complete the description of the wavefront distortion induced by the atmospheric turbulence, we must take into account its temporal evolution. In this section, we follow Conan et al.[33] in order to describe the derivation of temporal power spectra of wavefront distortions, in which the temporal PSD of phase-related quantities (e.g. Zernike coefficients) is defined.

Hereafter, we assume the Kolmogorov model and consider the case of a plane wave and a single turbulent layer. To derive the basic equations used to compute the PSD of a phase-related quantity $G(\boldsymbol{r}, t)$, where $\boldsymbol{r}$ is the spatial coordinate vector (x, y) and t the time, we start by defining its spatial covariance as follows:

$$B_G(\boldsymbol{\rho}) = \langle\, G(\boldsymbol{r}, t)\; G(\boldsymbol{r} + \boldsymbol{\rho}, t)\,\rangle\,, \tag{1.37}$$

that leads, relying on Parseval's theorem, to its spatial power spectrum W_G

$$W_G(\boldsymbol{f}) = \int B_G(\boldsymbol{\rho})\; e^{2\pi i\, \boldsymbol{f}\cdot\boldsymbol{\rho}}\, d\boldsymbol{\rho}, \tag{1.38}$$

where $\boldsymbol{f}$ is the spatial frequency vector (f_x, f_y). Since a phase-related quantity can be expressed as the convolution of the phase ϕ with a spatial function $M_G(\boldsymbol{r})$, as

$$G(\mathbf{r}, t) = \int M_G(\mathbf{r} - \boldsymbol{\rho})\, \phi(\boldsymbol{\rho}, t)\, d\boldsymbol{\rho} = M_G(\boldsymbol{\rho}) * \phi(\mathbf{r}, t)\,, \tag{1.39}$$

the spatial power spectrum W_G can be computed as follows:

$$W_G(\boldsymbol{f}) = |\widetilde{M}_G(\boldsymbol{f})|^2\, W_\phi(\boldsymbol{f})\,, \tag{1.40}$$

where $\widetilde{M}_G(\boldsymbol{f})$ is the FT of M_G and $W_\phi(\boldsymbol{f})$ is the spatial power spectrum of wavefront phase distortions from Eq. (1.14). The spatial PSD $W_G(\boldsymbol{f})$ can be related to the one-dimensional temporal PSD $w_G(\nu)$, where ν is the temporal frequency:

$$w_G(\nu) = \frac{1}{v} \int_{-\infty}^{+\infty} W_G\left(\frac{\nu}{v}, f_y\right)\, df_y\,, \tag{1.41}$$

where we assumed a wind speed v along the x axis and adopt the Taylor's frozen flow hypothesis, for which the whole phase screen is propagated at the wind speed v without changing shape. Substituting Eq.(1.40) into Eq.(1.41) and replacing W_ϕ with its expression in Eq.(1.14), the temporal PSD can be written as follows:

$$\begin{aligned} w_G(\nu) &= \frac{1}{v} \int_{-\infty}^{+\infty} \left|\widetilde{M}_G(\tfrac{\nu}{v}, f_y)\right|^2 W_\phi(\tfrac{\nu}{v}, f_y)\; df_y \\ &= 0.00969 \left(\frac{2\pi}{\lambda}\right)^2 \frac{C_n^2\, dh}{v} \int_{-\infty}^{+\infty} \left|\widetilde{M}_G(\tfrac{\nu}{v}, f_y)\right|^2 \left[(\tfrac{\nu}{v})^2 + f_y^2\right]^{-11/6} df_y\,, \end{aligned} \tag{1.42}$$

In the following, we provide a summary of the results related to the temporal PSD of the wavefront phase and the Zernike modes.

Wavefront phase

In this case, the function G is directly the phase:

$$G(\boldsymbol{r}) = \phi(\boldsymbol{r})\,. \tag{1.43}$$

Then, after the integration of Eq. (1.42), the temporal phase PSD can be expressed as follows:

$$w_\phi(\nu) \propto \frac{C_n^2\, dh}{v} \left(\frac{\nu}{v}\right)^{-8/3}, \tag{1.44}$$

Thus, the final result shows that the temporal PSD is a $-8/3$ power law of temporal frequency.

Zernike modes

To derive the temporal PSD in the case of Zernike modes, the function G is defined as follows:

$$G(\mathbf{r}) = Z_j(\mathbf{r}) * \phi(\mathbf{r}, t)\,. \tag{1.45}$$

In this case, $\widetilde{M}_G$ is the FT of the Zernike polynomial, as seen in Eq.(1.24). After substitutions, we can retrieve the expression of the temporal PSD for the Zernike modes, derived in Roddier et al.[34] and written as follows:

$$w_\phi(\nu) \propto \frac{1}{v}\int df_y \left(\nu^2/v^2 + f_y^2\right)^{-17/6} \left| J_{n+1}\left(\frac{2\pi}{v}\sqrt{\nu^2 + v^2 f_y^2}\right)\right|^2 \times \begin{cases} \cos^2(m\theta), & \text{even } j,\ m \neq 0, \\ \sin^2(m\theta), & \text{odd } j,\ m \neq 0, \\ 1, & m = 0\,, \end{cases} \tag{1.46}$$

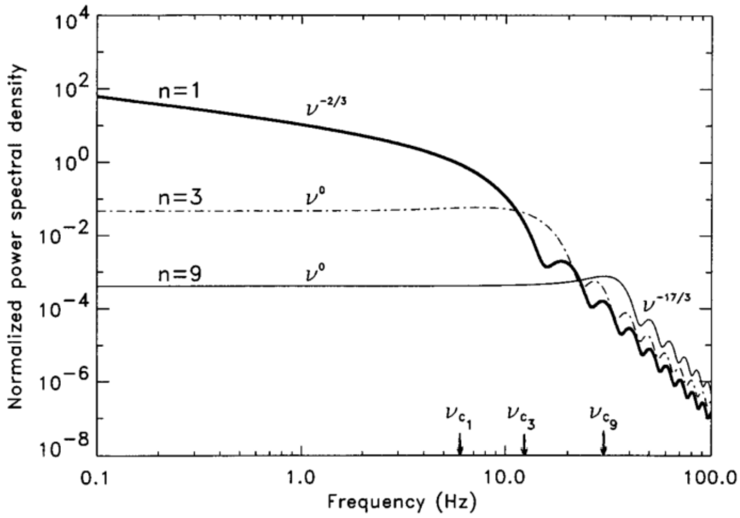

Figure 1.7. Mean temporal power spectrum of Zernike polynomials with $n = 1, 3, 9$, from Conan et al. [33]. The ratio v/D is 10 Hz. The power laws and the cutoff frequencies are shown.

As a result, the temporal PSD of Zernike modes shows the following remarkable properties that are shown in Figure 1.7:

- the spectra are characterised by a cutoff frequency that depends on the radial degree of the Zernike polynomial and on the wind speed to aperture size ratio:

$$\nu_c \approx 0.3\,(n+1)\,\frac{v}{D}\,; \tag{1.47}$$

- at high temporal frequencies, all the spectra follow a $\nu^{-17/3}$ law;

- the behaviour at low frequencies strongly depends on the Zernike mode: both Tip and Tilt follow a $\nu^{-2/3}$ law, radially symmetric polynomials (such as defocus, Z_4, and spherical aberration, Z_{11}) follow ν^0, the 7th and 8th mode (two comas, Z_7 and Z_8) follow a ν^0 and ν^2 law respectively. The other modes have a 0, 4/3 and 2 power laws;

- for radially symmetric polynomial, the spectra does not depend on the wind direction, while for other modes the behaviour at low frequencies is affected by wind changes.

1.2 Basics of adaptive optics systems

As seen so far, AO is aimed at recovering the best image quality in an optical system affected by time-dependent wavefront aberrations induced by the atmospheric turbulence. Figure 1.8 shows a simplified working scheme of an AO system. The basic principle of such a system foresees the measurement and real-time compensation of the wavefront distortion. Particularly, the turbulence-induced wavefront distortions are measured by means of a WFS, whose signals are analysed by a real-time computer (RTC). The RTC computes the required correction and sends the corresponding commands to a Deformable Mirror (DM), that changes its shape in order to flatten the wavefront. Since the atmospheric turbulence rapidly evolves in time scales τ_0, the entire AO feedback control loop must have a frequency response comparable to the typical atmospheric turbulence decorrelation time, requiring a fast frame rate of typically ~1kHz [24][2].

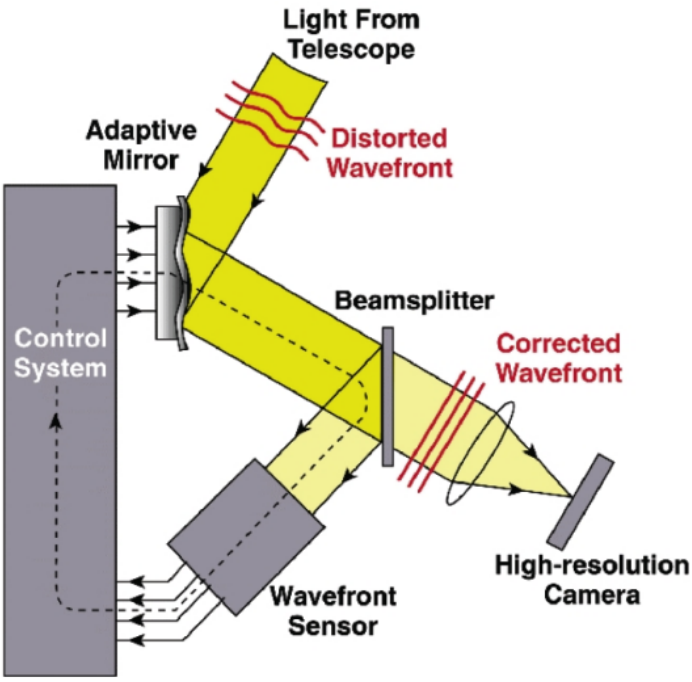

Figure 1.8. A simplified operational scheme of an AO system. The light collected by the telescope is directed to the DM, which reflects it toward a beam splitter. The flux is then split between WFS and the science path. The WFS measures the turbulent wavefront from a reference source (a Guide Star (GS)), while the RTC analyses the measured signals. Then, the RTC computes the the required commands to compensate for the disturbance and sends them to the DM. Finally, the DM changes its shape to flatten the wavefront, which is observed again by the scientific camera as a diffraction-limited image. Credits to Claire E. Max.

The reference target, in AO typically referred to as Guide Star (GS), whose wavefront is analysed by the WFS, must be a bright and point-like source in order to minimise the error in the WFS measurements. However, depending on the operative conditions of AO-assisted astronomical observations, such a Natural Guide Star

(NGS) is not often available in a narrow Field Of View (FOV) centred on the science target. In the context of AO, this is a part of the so-called sky coverage problem [35]. For this reason, Laser Guide Stars (LGS) have been proposed [36] [37] and are employed, providing an artificial bright GS reproduced relying on the scattering of laser radiation through the atmospheric particles. The most common LGSs are generated through resonance scattering of the sodium in the atmosphere, involving the use of a laser source at 589 nm to excite atoms in the atmospheric sodium layer at $\sim$ 90 km. Another commonly used LGS is the one reproduced through Rayleigh scattering from air molecules, which sends the scattered light back to the telescope from altitudes up to $\sim$15 km. However, the need for LGSs to compensate for the lack of bright NGS in the science FOV comes with strong limitations and side-effects. Among the others, one of the main limitations of LGSs is the inability to determine atmospheric Tip-Tilt modes, often referred to Tip-Tilt indetermination [38]. Particularly, LGSs are unable to provide a useful signal for Tilt correction since the upward propagation of the laser beam is usually unknown. In the simplest case, where the same telescope is used for both projecting and sensing the laser beacon, the light encounters the same Tilt in both upward and downward directions, and the LGS will appear motionless. For this reason, Tip-Tilt measurements need at least the use of one NGS, which can be of fainter magnitudes. Furthermore, since the light from an LGS comes from a finite distance, the wavefront coming from the LGS do not cross the same turbulent volume as in the case of a wavefront received from a NGS. This is the so-called "cone effect" that represents another major constraint in using LGS, as will be discussed in Sec.1.2.5.

To conclude, from the discussion so far, it is clear that AO requires a multidisciplinary approach: it requires competences in disparate field, from atmospheric turbulence theory, geometrical and diffractive optics, control theory and system engineering, among the others. In the following, we provide a description of the key elements of an AO system aimed to measure, reconstruct and compensate for the turbulent wavefront distortions.

1.2.1 Wavefront sensors

WFS are designed to the measure of the wavefront phase. However, at optical or near infrared wavelengths (500 - 2500 nm), it is not possible to directly sample the phase of the electromagnetic wave, as its frequency is too high (600 - 120 THz). Therefore, the measurement working principle is often aimed to convert the wavefront phase $\varphi(\vec{r})$ (or typically its spatial gradient $\nabla\varphi(\vec{r})$) into intensity variation in a measured image, by means of a detector. All wavefront sensors have to provide the following essential features:

- a spatial sampling of the pupil on a number of points high enough to provide an accurate wavefront reconstruction. At first-order, the spatial sampling required to sense (and correct) atmospheric turbulence is set by the Fried parameter, $r_0(\lambda)$. It represents the degree of freedom of the AO system (typically referred as *number of subapertures*, N_{sub}), which is defined as $N_{sub} \approx (D/r_0(\lambda))^2$, where D is the pupil diameter;

- a temporal sampling fast enough to be capable of following the aberration evolution with the needed accuracy. Each measurement $s(\vec{r}, t)$ in the pupil point $\vec{r}$ and at the time t will actually be a temporal average over a given integration period T:

$$s(\vec{r}, t) = \frac{1}{T} \int_t^{t+T} \varphi(\vec{r}, \tau) d\tau \, ; \tag{1.48}$$

- a wide dynamical range, i.e. the interval between $\min(\varphi(\vec{r}))$ and $\max(\varphi(\vec{r}))$ over which the measurement is reliable. Outside this range, the sensor saturates and is not capable of discriminating between different inputs;
- to make the best use of the few photons available in a typical astronomical application. This typically pushes the design to be broadband and noise insensitive;
- a good linearity response and accuracy.

In the following, we describe the main aspects and working principle of the most commonly used WFSs in AO systems: the Shack-Hartmann WFS [39] and the Pyramid WFS (PyWFS)[40][41].

Shack-Hartmann WFS

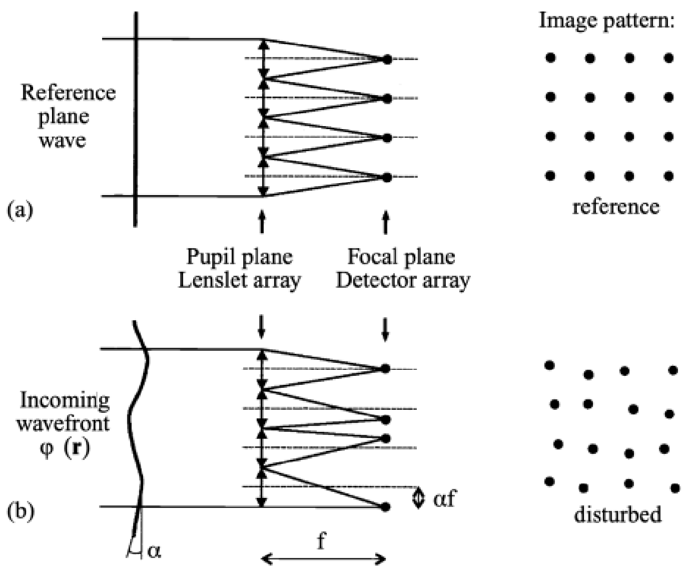

Figure 1.9. Scheme of the SHWFS. Top panel: If the wavefront is flat, each lenslet forms an image of the source in its focal plane along the lens axis. Bottom panel: if the wavefront is locally tilted by an angle α, the lenslet forms an image of the source at a distance αf from the focus, with f the focal length of the lenslet. From [24].

The working principle of the Shack-Hartmann WFS (SHWFS) is to use a lenslet array placed in a conjugate pupil plane, to sample the incoming wavefront. With reference to Figure 1.9, if the wavefront is flat, each lens of the lenslet array forms an on-axis image of the source in its focal plane. In contrast, if the wavefront is aberrated, each lenslet receives, at first-order, a locally tilted wavefront that results in an off-axis image in its focal plane. The slope of the wavefront over each lenslet can then be inferred from the measurement of spots' positions on the lenslet focal plane.

The simplest method to measure the spots' position is to use a detector with 2×2 pixel for each subaperture. This configuration is called *Quad Cell* (QC). Referring to Figure 1.10 and defining I_i the intensity on the $i-$th pixel, we compute 2 signals for each QC as:

$$S_x = \frac{I_2 + I_4 - I_1 + I_3}{\sum_i I_i} \tag{1.49}$$

$$S_y = \frac{I_1 + I_2 - I_3 + I_4}{\sum_i I_i} . \tag{1.50}$$

It can be demonstrated that the signals are proportional to the spatial derivative of the wavefront along x and y according to the following relation:

$$S_x = \frac{2}{\theta}\frac{\partial\varphi}{\partial x} \tag{1.51}$$

$$S_y = \frac{2}{\theta}\frac{\partial\varphi}{\partial y} , \tag{1.52}$$

where θ is the spot size on the QC and φ is the aberrated wavefront.

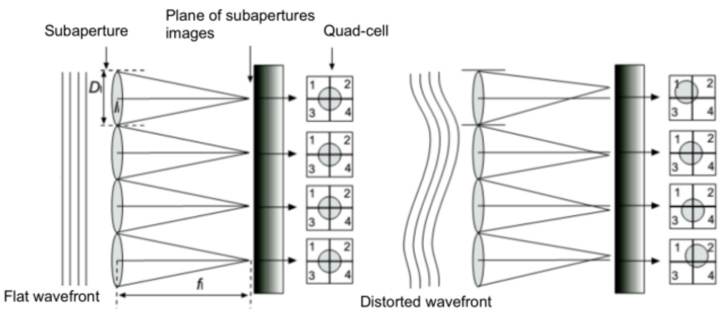

Figure 1.10. Scheme of a SHWFS in Quad-Cell configuration. Courtesy of S. Esposito.

As seen from the latter equations, the SHWFS does not provide a direct measurement of the phase map on the pupil, but rather an estimate of its gradient. The reconstruction of the phase map can be obtained by integration of a 1st order differential equation, obtaining a unique phase map up to an additive constant that is irrelevant for the purpose of the image formation. However, in practice and as we will see in Sec.1.2.4, an integration of the differential equations is rarely performed, as in AO is preferred to link a known, imposed, phase map to the corresponding WFS signals and then invert the algebraic equations to compute a phase reconstructor that links a measured set of signals to the corresponding phase map.

The equations above are not valid anymore when the displacement of the spot is comparable with the spot size, as we incur in large non-linearity between the wavefront gradient and the produced signals. To overcome this problem and increase the linearity range of the WFS, algorithms are typically used that estimate the photocentre of the spots on more than 2×2 pixels. If we sample each subaperture with N pixels, where each pixel is related to a position (x_i, y_i) with respect to the centre of the subaperture and receives an intensity I_i, it can be shown that the average wavefront gradient in the subaperture is given by:

$$S_x = \frac{\sum_{i=1}^{N} I_i x_i}{\sum_{i=1}^{N} I_i} \tag{1.53}$$

$$S_y = \frac{\sum_{i=1}^{N} I_i y_i}{\sum_{i=1}^{N} I_i} \,. \tag{1.54}$$

To conclude, the above equations are often referred as Centre-of-Gravity (CoG) algorithm, that is the most simple routine to infer the spot position in SHWFS. However, in AO practice this method is known to have limitations and more complex algorithms are adopted involving intensity thresholding and/or pixel weighting, to ensure stability, avoid bias and reduce noise in the measured signal [42].

Pyramid WFS

As shown in the left panel of Figure 1.11, the Pyramid WFS (PyWFS) is made of an optical element in the form of a glass square-based pyramid [40] [41], where the pyramid vertex is positioned in the focus of the converging beam. In the absence of any aberration, the beam is split into 4 and is re-imaged on the detector through a camera lens. The distance between the pupil images and their size depends on the input beam aperture, on the pyramid vertex angle and on the camera lens focal length. The spatial sampling of the four pupil images is given by the number of illuminated pixels on the detector. Since any point of the pupil is re-imaged on each of 4 pupil images, on 4 pixels of the detector it can be shown that by combining the intensity of the 4 pixels, in the same way as seen of the quad-cell detector (as in Eqs. (1.49) and (1.50)), we obtain a signal proportional to the wavefront gradient.

With reference to the right panel of the latter figure, the PyWFS is typically equipped with a flat oscillating mirror positioned in a pupil conjugate plane, capable of steering the image in the focal plane. This element is used to introduce the so-called *Tilt modulation*, i.e. to let the image perform a circular trajectory centred around the pyramid vertex, with a period equal to the detector integration time. This device allows us to change and adapt the dynamic range of the WFS as we will see in the following.

Referring to Figure 1.12, a ray coming from a non-aberrated subaperture (left panel) would focus on the pyramid vertex without Tilt modulation. With the modulation, it performs a circular path centred around the pyramid vertex, spending an equal amount of time on the 4 pyramid faces and resulting in a balanced illumination of the 4 pixels corresponding to the considered pupil subaperture. In the case of wavefront aberration (right panel), the circular path will be centred around an off-axis point shifted by $\Delta\eta$, proportional to the wavefront Tilt. The

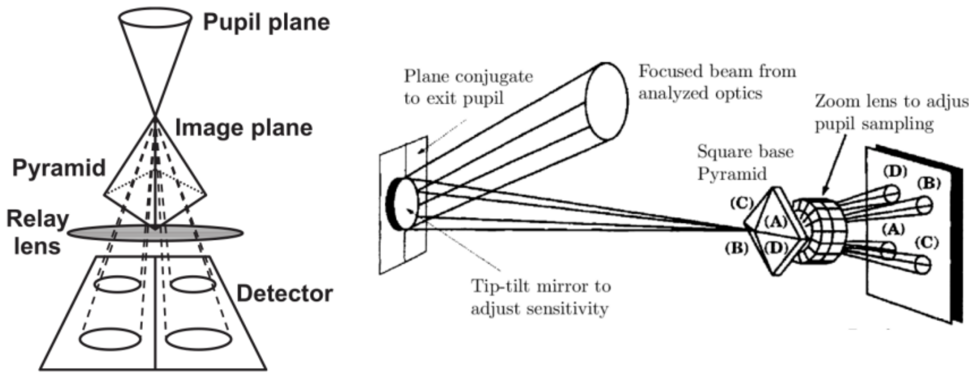

Figure 1.11. Outline of a pyramid WFS. A basic scheme of the Pyramid WFS is shown on the left, and a scheme with the Tilt modulation is shown on the right panel. From Esposito et al. [41].

circular arcs on the 4 faces have now different lengths b_i and the illumination I_i of the 4 corresponding pixels is unbalanced.

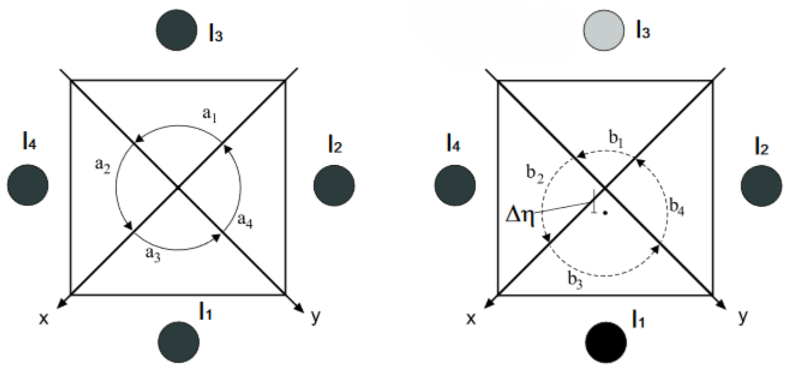

Figure 1.12. Scheme of the path of a beam incident on the pyramid focal plane in the presence of Tilt modulation. Squared-base pyramid view from the top. A ray coming from a non-aberrated subaperture (left) would focus on the pyramid vertex without Tilt modulation. With the modulation, it performs a circular path centred around the pyramid vertex, spending an equal amount of time on the 4 pyramid faces and resulting in a balanced illumination of the 4 pixels corresponding to the considered pupil subaperture. In the case of wavefront aberration (right), the circular path will be centred around an off-axis point shifted by $\Delta\eta$, proportional to the wavefront Tilt. The circular arcs on the 4 faces have now different lengths b_i and the illumination I_i of the 4 corresponding pixels is unbalanced. From [43].

We introduce the signal quantities:

$$S_x(x,y) = \frac{(I_1(x,y) + I_4(x,y)) - (I_2(x,y) + I_3(x,y))}{I_1(x,y) + I_2(x,y) + I_3(x,y) + I_4(x,y)} \tag{1.55}$$

$$S_y(x,y) = \frac{(I_1(x,y) + I_2(x,y)) - (I_4(x,y) + I_3(x,y))}{I_1(x,y) + I_2(x,y) + I_3(x,y) + I_4(x,y)}\,, \tag{1.56}$$

and it can be shown with geometrical arguments that the relation between the signals S_x, S_y and the wavefront gradient is as follows:

$$\frac{\partial \varphi(x,y)}{\partial x} = \frac{R_m}{f} \sin\left(\frac{\pi}{2} S_x\right) \tag{1.57}$$

$$\frac{\partial \varphi(x,y)}{\partial y} = \frac{R_m}{f} \sin\left(\frac{\pi}{2} S_y\right), \tag{1.58}$$

with R_m modulation radius and f distance between the modulation mirror and the pyramid. As shown from the relation above, the dynamic range of the sensor can be tuned during the operations by changing the modulation radius. This is a particularly interesting feature as it allows to adapt the WFS to the operational conditions: in case of very bad seeing (for instance, at system bootstrap or in other cases with large wavefront aberration) the WFS will be set up with a large modulation radius in order to obtain the maximum dynamical range. On the other side, in the cases where we do not require a large dynamical range (like in good seeing conditions or any operational case with small wavefront errors) the modulation radius can be decreased to the advantage of an improved WFS sensitivity and measurement precision.

1.2.2 Deformable mirrors

In AO-assisted astronomical observations, the typical devices used to correct the wavefront aberrations introduced by atmospheric turbulence are DMs, i.e. optical mirrors whose shape can be actively controlled through actuators.

DM must be designed to meet the following general requirements:

- spatial correction: it must have a sufficient number of actuators to reproduce the commanded wavefront with a given accuracy, which is set at first-order by $N_{sub} \approx (D/r_0(\lambda))^2$(as seen in Sec.1.2.1). The difference between the commanded wavefront and the actual shape the mirror is capable of acquiring is called *fitting error*. As we have seen in Sec.1.1.2, a typical number of actuators for an 8-m telescope is about 1000;

- stroke: each actuator must have a sufficient stroke (range of deformation) to reproduce the commanded wavefront with the given fitting error, as above;

- spectral correction: astronomical optical systems are typically broadband, with the scientific instrument typically working in a near-infrared wavelength range and the WFS working in the visible. The wavefront correcting device must be achromatic in such a way that the aberrations sensed by the WFS is properly corrected on the scientific camera. This is the point that drives for reflective devices like mirrors, as they are intrinsically achromatic;

- temporal correction: the DM must be able to modify its figure to the required shape in a short time, comparable or faster than the AO loop frame rate;

- continuous or segmented: the mirror surface can be segmented, made up of several independent segments, or continuous, i.e. made up of a single facesheet;

- actuator density/overall size: any actuator technology has its own range of actuator density that, for a given number of actuators, determines the overall size of the mirror. The size of the DM plays a major role in defining the optical system: if the DM is located in the telescope optical train, as the adaptive secondary mirror at LBT/VLT or ELT's M4, the mirror has to be large (order of 1 m diameter for the 8 m telescopes, 2.5 m for the ELT), imposing quite a large pitch ($\simeq$ 30 mm) between the actuators. If, instead, the DM is located in a post-focal AO module, optical designers tend to limit the size of the pupil to reduce the overall size of the instrument: MEMS technology can produce DMs with a pitch of about 0.5 mm, and a diameter of <20 mm well-suited for an extreme AO system, such as Planet Finders [44]. Unfortunately, because of Lagrange invariant (or conservation of etendue), a too-small pupil magnification is not feasible in wide field AO systems like MORFEO: as shown in Figure 1.13, the ray angles θ in a hugely demagnified pupil plane (a factor D/D' of 1000 for 40 m telescope reimaged on a 40 mm DM) would become so large that the reimaging optical system would be very hard to realise.

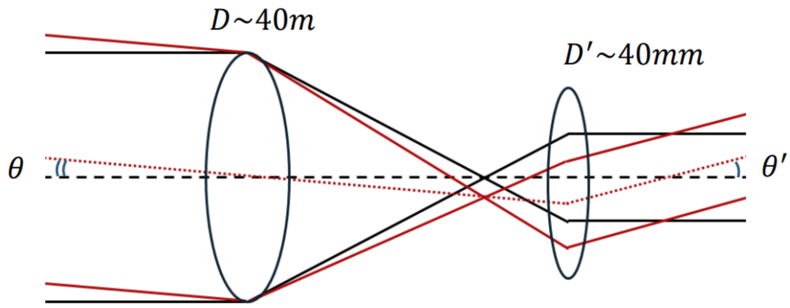

Figure 1.13. Visual representation of the pupil demagnification in the case of MORFEO due of Lagrange invariant of extremely large pupil to DM aperture typically involved in AO laboratory applications. MORFEO has a technical FOV of $2\theta = 150$arcsec, which involves huge angles $\theta' \sim 41$ degrees on a demagnified pupil of 40mm, which is not feasible to realise. The scheme is not in scale for visualisation purposes.

Different technologies for DMs do exist [45] (such as piezo-stack DMs, voice-coil actuator DMs, MEMS) that differs mainly in the actuator's functioning principle.

1.2.3 Feedback control loop

As mentioned in Sec.1.2, AO systems can be considered as servo-loop systems designed for compensating for the incoming aberrated wavefront caused by atmospheric turbulence. As shown in Figure1.8, the basic configuration of an AO system consists of a sensor, the WFS, a control device, the RTC, and a corrector, the DM. Particularly, the input and output of such a control loop are the turbulent wavefront phase and its residual phase after compensation, respectively. The aim of the AO control loop is to minimise the residual phase.

The temporal behaviour of an AO control loop is usually described using a temporal transfer function representation [46]. A schematic block diagram of an AO control loop is shown in Figure 1.14. With reference to the latter figure, $\phi_{\rm turb}$ is the input turbulent phase, $\phi_{\rm a}$ is the compensating phase actuated by the DM, which is based on the correction phase $\phi_{\rm corr}$ that is computed from the residual phase $\phi_{\rm res}$. Here, the phase ϕ refers to the Laplace- or Z-transform of the phase defined in the time domain, depending on whether a continuous or discrete domain is considered. The introduced quantities can be described by the following relations:

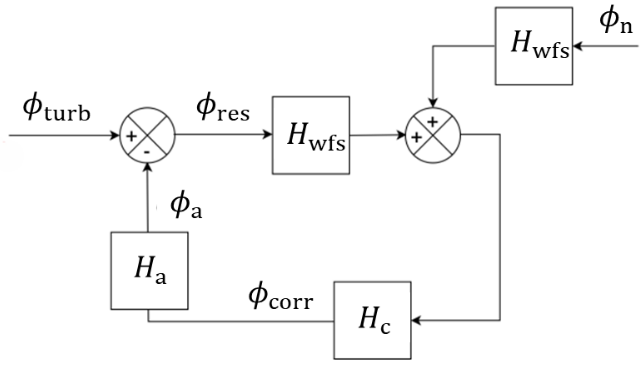

Figure 1.14. Block scheme of an AO control loop.

$$\phi_{\rm res}(\nu) = \phi_{\rm turb}(\nu) - \phi_a(\nu) \tag{1.59}$$

$$\phi_a(\nu) = H_{\rm wfs}(\nu)\,(\phi_{\rm res}(\nu) + \phi_n(\nu))\,H_c(\nu)\,H_a(\nu) \tag{1.60}$$

where $\phi_{\rm n}$ is the noise introduced in the loop due to the WFS integration only (i.e. photo noise), ν is the temporal frequency, and $H_{\rm k}$ is the temporal transfer function of a given block k. Particularly, $H_{\rm wfs}$, $H_{\rm c}$ and $H_{\rm a}$ are the transfer functions of the WFS, the control by means of the RTC and the actuation of the DM, respectively.

Assuming the system is linear, the open-loop transfer function (OLTF) can be computed from the product of all the temporal transfer functions, as follows:

$$H_{\rm ol}(\nu) = H_{\rm wfs}(\nu)\,H_{\rm c}(\nu)\,H_{\rm a}(\nu) \tag{1.61}$$

Following [46], the explicit expression for the OLTF in the case of a simple pure integrator is given by:

$$H_{\rm ol}(s) = \frac{1 - e^{-sT}}{sT}\; e^{-sT_d}\; \frac{g}{sT} \tag{1.62}$$

where s $= 2\pi\, i\, \nu$ is the Laplace variable, g is the integrator gain, T is the WFS integration time that defines the frequency frame rate of the loop ($\nu_{loop} = 1/\mathrm{T}$), T_d is a delay (e.g. readout time) and where the transfer functions have been defined as $H_{\rm wfs}(\nu) = (1 - \exp{(-sT)})/sT$, $H_{\rm c}(\nu) = \exp{(sT_d)} g/sT$ and $H_{\rm a}(\nu) = 1$.

Combining Eqs. (1.59), (1.60) and (1.61), we can define the Rejection Transfer Function (RTF) and Noise Transfer Function (NTF), as follows:

$$\begin{aligned}\phi_{\text{res}}(\nu) = \phi_{\text{turb}}(\nu) - \phi_a(\nu) \; &= \\ = \phi_{\text{turb}}(\nu) - H_{\text{wfs}}(\nu)(\phi_{\text{res}}(\nu) + \phi_n(\nu))\, H_c(\nu)\, H_a(\nu) \; &= \\ = \phi_{\text{turb}}(\nu) - H_{\text{ol}}(\nu)(\phi_{\text{res}}(\nu) + \phi_n(\nu))&\end{aligned} \tag{1.63}$$

and grouping the terms related to ϕ_{res}:

$$(1 + H_{\text{ol}}(\nu))\, \phi_{\text{res}}(\nu) = \phi_{\text{turb}}(\nu) - H_{\text{ol}}(\nu)\, \phi_n(\nu). \tag{1.64}$$

ϕ_{res} can be written as follows:

$$\begin{aligned}\phi_{\text{res}}(\nu) = \frac{1}{1 + H_{\text{ol}}(\nu)}\, \phi_{\text{turb}}(\nu) - \frac{H_{\text{ol}}(\nu)}{1 + H_{\text{ol}}(\nu)}\, \phi_n(\nu) &= \\ = H_r(\nu)\, \phi_{\text{turb}}(\nu) - H_n(\nu)\, \phi_n(\nu)&\end{aligned} \tag{1.65}$$

The latter equation leads to the following expression for the RTF and NTF:

$$H_r(\nu) = \frac{1}{1 + H_{\text{ol}}(\nu)} \tag{1.66}$$

$$H_n(\nu) = \frac{H_{\text{ol}}(\nu)}{1 + H_{\text{ol}}(\nu)}\,. \tag{1.67}$$

The RTF is defined as the transfer function between the residual and turbulent phases, representing the capability of the AO control to compensate for phase disturbance as a function of frequency. The NTF is defined as the ratio of the residual phase due to noise propagation to the measurement noise, and it characterises the effect of noise on the residual phase. From Eq.(1.66) and Eq.(1.67), it can be seen that holds the following relationship:

$$H_r(\nu) + H_n(\nu) = 1 \tag{1.68}$$

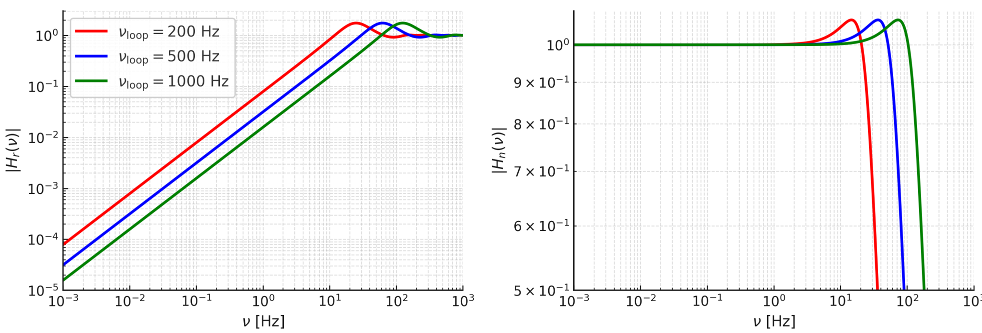

Figure 1.15. 2 Modulus of the RTF (left) and NTF (right) as a function of temporal frequencies. Three values of the loop frequency are shown, corresponding to WFS integration time of 5 ms red), 2 ms (blue) and 1 ms (green). Delay from the WFS integration only is considered. The plots share the same legend.

Figure 1.15 shows the RTF and NTF for different values of the loop frequency. Finally, from Eq.(1.65) we can infer the temporal power spectrum of the residual wavefront S_{res} on the GS:

$$S_{\text{res}}(\nu) = \left|H_r(\nu)\right|^2 S_{\text{turb}}(\nu) + \left|H_n(\nu)\right|^2 S_n(\nu) \tag{1.69}$$

where S_{turb} and S_{n} are temporal spectra of turbulence and noise, respectively, assuming that turbulence and noise are uncorrelated.

To conclude, from the present discussion, we saw that open-loop operations refer to the fact that the WFS measures the absolute/direct atmospheric wavefront, while in a closed-loop, the WFS only detects the residual wavefront after DM correction.

1.2.4 Wavefront reconstruction

The wavefront reconstruction is the process that allows to compute the required commands to be applied to the DM from the measured signals of the WFS.

A generic wavefront $\varphi(\boldsymbol{r})$ can be described as a linear combination of functions F_j as

$$\varphi(\boldsymbol{r}) = \sum_j a_j F_j(\boldsymbol{r})\,. \tag{1.70}$$

One way of visualising the relation above, possibly the most immediately clear, is to consider that the $F_j(\boldsymbol{r})$ are the so-called *influence functions* (IFS), i.e. the wavefront deformation corresponding to the actuation of the j^{th} actuator with unitary amplitude. In this case, the sum extends over the J actuators of the deformable mirror, or better, to the J actuators whose influence function is visible in the pupil, and the vector of the actuator commands $\boldsymbol{a} = [a_1, a_1, ..., a_J]$ is a *zonal* representation of the mirror shape. It is intuitive that a linear combination of J functions does not allow to reproduce any arbitrary wavefront shape: there will be a difference between the actual wavefront and the best approximation that can be realised by the deformable mirror. As mentioned in Sec.1.2.2, this difference is called *fitting error*.

The Zernike polynomials base, as seen in Sec.1.1.2, is a valid set of functions F_j: in this case, the summations extend over infinite functions, as in Eq.(1.25) where any given wavefront can be described as an infinite series of Zernike polynomials. In this so-called *modal* representation, the elements a_j correspond to the amplitude of the jth Zernike mode, and $\boldsymbol{a}$ can extend to an infinite number of elements. As seen in Eq. (1.36), the first J modes are sufficient to give an arbitrarily accurate representation of the Kolmogorov turbulence; therefore, in practice also in the modal approach the summation actually extends only over the first J modes, neglecting the subsequent ones. In both cases, either if one follows a zonal control or a modal control, the vector $\boldsymbol{a}$ is the representation of the wavefront $\varphi(\boldsymbol{r})$.

Moving on to the wavefront sensing, the WFS can be modelled as an operator W that samples the wavefront $\varphi(\boldsymbol{r})$ in a set of discrete points and outputs the vector of measurements $\boldsymbol{s}$.

$$\boldsymbol{s} = W(\varphi(\boldsymbol{r})). \tag{1.71}$$

To give some examples, if a Py-WFS is used, the element s_k corresponds to the wavefront $\varphi(\boldsymbol{r})$ measured in the kth pixel of the illuminated pupil, and the size of

$\boldsymbol{s}$ is M, with M the number of pixels of the illuminated pupils in the frame of the detector. In the case of a gradient WFS, like a SHWFS with K subapertures, the relations between the WFS signals and the wavefront are given by:

$$s_k = \left.\frac{\partial \varphi(\boldsymbol{r})}{\partial x}\right|_k = \sum_j a_j \left.\frac{\partial F_j(\boldsymbol{r})}{\partial x}\right|_k , \tag{1.72}$$

$$s_{k+K} = \left.\frac{\partial \varphi(\boldsymbol{r})}{\partial y}\right|_k = \sum_j a_j \left.\frac{\partial F_j(\boldsymbol{r})}{\partial y}\right|_k \tag{1.73}$$

where the vertical bar stands for the spatial average over the kth subaperture and the signal vector $\boldsymbol{s}$ contains $M = 2K$ gradient values, with K the number of subapertures in the WFS, and k is an index running from 1 to K.

Regardless of the zonal or modal wavefront representation or the type of WFS used, the above arguments can be described generically in the following matrix form:

$$\boldsymbol{s} = \mathbf{H}\boldsymbol{a} , \tag{1.74}$$

where the representation of the wavefront $\boldsymbol{a}$ is related to the measure $\boldsymbol{s}$ through the *interaction matrix* $\mathbf{H}$. The measure $\boldsymbol{s}$ is a vector of M elements, the wavefront $\boldsymbol{a}$ is a vector of J elements and the interaction matrix $\mathbf{H}$ has $M \times J$ elements and is obtained by stacking horizontally the columns s^j, where s^j is the WFS response to the wavefront F_j:

$$\mathbf{H} = \begin{bmatrix} s_1^1 & s_1^2 & \dots & s_1^J \\ s_2^1 & s_2^2 & \dots & s_2^J \\ \vdots & \vdots & \vdots & \vdots \\ s_M^1 & s_M^2 & \dots & s_M^J . \end{bmatrix} \tag{1.75}$$

In order to estimate the actuators' commands to be applied to obtain a given deformation on DM's surface, the control system must reconstruct the wavefront by inverting the relation in Eq.(1.74), leading to the following relation:

$$\tilde{\boldsymbol{a}} = \mathbf{R}\boldsymbol{s} \tag{1.76}$$

where $\tilde{\boldsymbol{a}}$ is the vector representing the wavefront reconstructed from the measured signals $\boldsymbol{s}$. $\mathbf{R}$ is called the *reconstruction matrix* and represents the pseudo-inverse of the interaction matrix $\mathbf{H}$, $\mathbf{H}^\dagger$, which corresponds to the generalization of the inverse matrix applied to non-square matrices. Indeed, Eq.(1.74) corresponds to an overdetermined set of M linear equations in J unknowns because $M > J$ and an exact solution for $\tilde{\boldsymbol{a}}$ doesn't exists. The Moore-Penrose pseudo-inverse [47] of $\mathbf{H}$ is given by:

$$\mathbf{H}^\dagger = (\mathbf{H}^T\mathbf{H})^{-1}\mathbf{H}^T \tag{1.77}$$

and such that $\mathbf{H}^\dagger\mathbf{H} = \mathbf{I}$, where $\mathbf{I}$ is the identity matrix and $\mathbf{H}^T$ is the transpose matrix of $\mathbf{H}$. Furthermore, $\mathbf{H}^\dagger$ is the least square solution (LSE) of the minimization of $\| \boldsymbol{a} - \tilde{\boldsymbol{a}} \|^2$ [47].

Many techniques exist to compute the pseudo-inverse of the interaction matrix. In classical AO control systems, the most commonly used is based on Singular Value Decomposition (SVD) [48]. This technique relies on the following theorem of linear algebra: any $M \times N$ real matrix, whose number of rows M is greater than or equal to its number of columns N, can be written as the product of an $M \times N$ matrix $\mathbf{U}$, an $N \times N$ diagonal matrix $\mathbf{\Lambda}$ and the transpose of an $N \times N$ matrix $\mathbf{V}$. The matrix $\mathbf{U}$ is column-orthogonal, i.e. $\mathbf{U}^T\mathbf{U} = \mathbf{I}$ while $\mathbf{U}\mathbf{U}^T \neq \mathbf{I}$. The matrix $\mathbf{\Lambda}$ is diagonal with positive or null elements λ_i called *singular values*. The matrix $\mathbf{V}$ is orthogonal, i.e. $\mathbf{V}^T\mathbf{V} = \mathbf{V}\mathbf{V}^T = \mathbf{I}$. Specifically, the interaction matrix $\mathbf{H}$ can be factorized as:

$$\mathbf{H} = \mathbf{U}\mathbf{\Lambda}\mathbf{V}^T \tag{1.78}$$

From Eq.(1.78), we can define the matrix:

$$\mathbf{H}^\dagger = \mathbf{V}\mathbf{\Lambda}^{\mathbf{-1}}\mathbf{U}^T \tag{1.79}$$

where $\mathbf{\Lambda}^{\mathbf{-1}}$ is the diagonal matrix with diagonal elements $1/\lambda_i$. It is easy to see that

$$\mathbf{H}^\dagger\mathbf{H} = \mathbf{V}\mathbf{\Lambda}^{\mathbf{-1}}\mathbf{U}^T\mathbf{U}\mathbf{\Lambda}\mathbf{V}^T = \mathbf{V}\mathbf{\Lambda}^{\mathbf{-1}}\mathbf{\Lambda}\mathbf{V}^T = \mathbf{V}\mathbf{V}^T = \mathbf{I} \tag{1.80}$$

and $\mathbf{H}^\dagger$ defined as in Eq.(1.79) is the pseudo-inverse of $\mathbf{H}$ and corresponds to the reconstruction matrix $\mathbf{R}$.

To conclude, in AO practice, the singular values λ_i represent the capability of the WFS to measure the wavefront. An element a_i that is related to a singular value $\lambda_i \to 0$ produces a noisy signal $s_i \to 0$, which is not detected by the WFS. The associated unseen or bad seen (for which $\lambda_i \to 0$) mode (or zonal IFS), is typically discarded during the pseudo-inverse operation, by setting the related value $1/\lambda_i$ equal to zero. Typically, a threshold of $\sim 1/100$ of the maximum singular value λ_{max} is used. This method is commonly known as truncated SVD (T-SVD) [49].

1.2.5 Limitations of classical adaptive optics

The wavefront compensation achieved by AO systems is never perfect. As discussed so far, these systems are clearly subject to limitations arising from the operating conditions of the observations, mainly defined by the nature of the atmospheric turbulence. Furthermore, AO systems are also affected by their own intrinsic limitations. These limitation affect different domains (such as spatial, temporal and angular ones, among others). For the present discussion, we provide a summary of the main sources of error that affect AO systems and their performance. In the following, we refer to Davides's [2] and Rigaut's [3] reviews of the state of the art of AO systems.

Fitting error

As previously discussed in Sec.1.1.1, the characteristic spatial scale of turbulence goes down to the order of centimetres. In addition, as mentioned in Sec.1.1.2, 1.2.4 and 1.2.2, a perfect correction on an aperture of a few meter would require a DM with hundreds of thousands of actuators. Moreover, we saw in Sec1.1.1 that the spatial power spectrum of an input phase fluctuation decreases as a function of the spatial frequency, demonstrating that there is no such advantage in compensating for increasingly higher frequencies. The residual phase due to spatial frequencies that are not compensated leads to the so-called fitting error and is defined as:

$$\sigma^2_{\text{fitting}} = \int_{f_c}^{\infty} \Phi(f)\, df, \tag{1.67}$$

where the DM can be think as a high band pass filter with a cut-off frequency f_c, that is, the maximum frequency that the DM is able to compensate for, and for which $f_c = 1/2d_{\text{DM}}$, where d_{DM} is the inter-actuator pitch projected onto the pupil plane. It can be shown that, assuming the Kolmogorov model of PSD turbulence, Eq. (1.67) becomes:

$$\sigma^2_{\text{fitting}} = a_F \left(\frac{d}{r_0}\right)^{5/3}, \tag{1.68}$$

where d is the subaperture size, r_0 the Fried parameter (Eq.(1.6)) and a_F is a coefficient that depends on the geometry and shape of the DM and its actuators.

Temporal error

As discussed in Sec.1.2.3, an AO control loop is intrinsically affected by a delay between the WFS measurements and the DM application of the correction. This is given at least by the integration time of the WFS. During the period in which the correction is applied, the input perturbation changes, resulting in an imperfect correction. This is called temporal (or servo-lag) error and is defined as follows:

$$\sigma^2_{\text{temporal}} = K \left(\frac{T}{\tau_0}\right)^{5/3}, \tag{1.69}$$

where τ_0 is the coherence time defined in Eq.(1.11), T is the loop sampling time (i.e. WFS integration time) and K depends on the characteristics of the loop and control law.

WFS measurement error

The measurement noise of the WFS introduces an error that is propagated in the wavefront reconstruction (Eq.(1.76)), affecting the accuracy of the retrieved commands $\tilde{\boldsymbol{a}}$. It can be demonstrated that the variance depends on the inverse of signal-to-noise ratio (SNR). In the case of the SHWFS the variance follows the following relation:

$$\sigma^2_{\text{wfs}} \propto \theta^2/\text{SNR}^2 \tag{1.81}$$

where θ is the subaperture's spot size.

Aliasing error

This error arises from the fact that there are spatial frequencies in the wavefront that are greater than the Nyquist frequency f_{Nyq} of the chosen WFS. For instance, in the case of the SHWFS $f_{\text{Nyq}} = \frac{1}{2} f_{\text{samp}}$, where f_{samp} is the sampling frequency defined by the lenslet array subaperture size on the pupil. These frequencies are not seen by the WFS, but can appear in the measured signals as low spatial frequencies, compromising the wavefront reconstruction. The associated variance is given by:

$$\sigma^2_{aliasing} = a_A \, (d/r_0)^{5/3} \,,$$

where d is the subaperture size of the WFS on the pupil and a_A is a coefficient with values typically within 0.035-0.08, depending on the adopted reconstruction algorithms, turbulence model, and modal filtering, among others [50][51].

Focal anisoplanatic error: "cone effect"

As seen in Sec.1.2, the light from an LGS comes from a finite distance compared to astronomical objects. Thus, the wavefront coming from the LGS do not cross the same turbulent volume as in the case of a wavefront received from a NGS. The two wavefronts experience different optical paths. This is called the cone effect or focal anisoplanatism. The residual variance due to the cone effect in a telescope pupil of diameter D is given by:

$$\sigma^2_{\text{cone}} = (D/d_0)^{5/3} \quad \text{with} \quad d_0 \propto H_t \, \theta_0 \tag{1.82}$$

where d_0 is a parameter that depends on the C_n^2 from the anisoplanatic angle θ_0 and the altitude H_t of the LGS. Typical values of d_0 for $\theta_0 = 2.5$arcsec (at $\lambda = 0.5\mu$m), are 3.2m and 0.7m for the Sodium ($H_t = 90$km) and Rayleigh ($H_t = 30$km) LGS, respectively. These values make it easy to see that this effect is highly detrimental for the next generation of 40m-class telescopes like ELT.

Angular anisoplanatic error

In most cases, the science target is not a suitable bright reference source (GS) to fed properly the AO loop and another GS is chosen in the proximity of the scientific object. However, as similarly seen for the cone effect, the wavefront sensed from another GS in the FoV will pass through a different turbulent volume compared to the one propagated along the direction of the science target. The residual due to the uncorrected turbulence is commonly known as angular anisoplanatic error. Considering the scientific object and the AO GS reference source separated by an angular distance θ, the error can be derived from Eq. (1.4) of the structure function:

$$\sigma^2_{\text{aniso}} \approx 2.91 \, k^2 (\cos\gamma)^{-1} \int C_n^2(h) \, dh \, \left[\theta \, h (\cos\gamma)^{-1}\right]^{5/3}, \tag{1.83}$$

where the linear separation ξ in Eq.(1.4): is $\xi = \theta z$, with $z = h(\cos\gamma)^{-1}$. Reminding the definition of θ_0 in Eq.(1.10), Eq. (1.83) can be written as:

$$\sigma^2_{\text{aniso}} = \left(\frac{\theta}{\theta_0}\right)^{5/3} . \tag{1.84}$$

The latter equation shows that the anisoplanatic error increases with the target to reference GS separation θ. For typical values seen of θ_0, the anisoplanatic error strongly limits the AO correction to a small field of view around the reference source of about $\lesssim$ 15arcsec.

1.2.6 Performance of adaptive optics systems

To quantify the image quality, there are several criteria depending on the science cases. However, the most common metric used to quantify the performance of AO-assisted observation is the Strehl Ratio (SR). This merit function is a measure of how close an image is to the theoretical diffraction limit. The SR is defined as the ratio of maximum intensity of a measured (seeing-limited) point-spread-function (PSF), I_{meas}^{peak}, to the maximum of the diffraction-limited PSF , I_{DL}^{peak}, both normalized to the same total flux:

$$\mathrm{SR} = I_{meas}^{peak} / I_{DL}^{peak} . \tag{1.85}$$

An Airy pattern has a SR of 100%, while typical values of SR for seeing-limited images in the NIR spectrum and on an 8-m telescope are shown in Figure 1.16. In practice, the SR strongly depends on the wavelength and on the observation operative condition (i.e. brightness of the GS, among others).

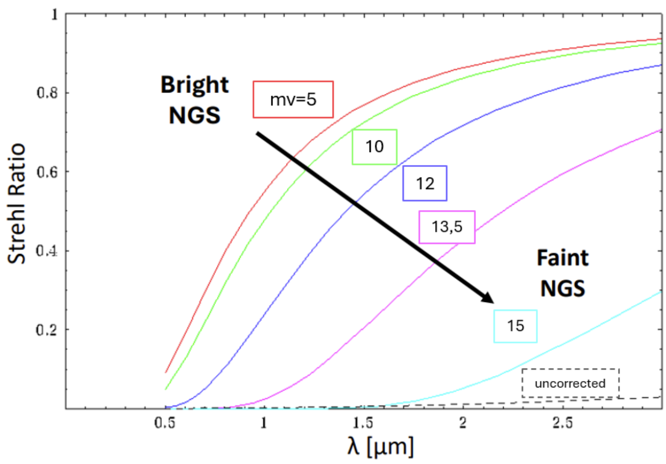

Figure 1.16. Simulations of SR as a function of the observing wavelength for the Keck-Telescope (8m-class). The plot shows how the SR increases as a function of the wavelength and the brightness of the GS. The brightness is quantified with the magnitude of the GS in the visible m_V. Without entering into details, the smaller m_V it is, grater is the brightness of the GS. The dashed line show the expected SR in seeing-limited conditions: it shows how crucial it is to use AO system for large telescopes. The figure is readapted from the Keck AO Blue Book.

Another way to quantify the performance of an AO system, which is used to design such systems with an error budgeting approach, is to quantify the residual wavefront error variance σ^2_{WFE} over the telescope aperture. As seen in Sec.1.2.5, several errors contributes to the residual wavefront error, that in first approximation can be considered uncorrelated:

$$\sigma^2_{\mathrm{WFE}} = \sigma^2_{\mathrm{fitting}} + \sigma^2_{\mathrm{temporal}} + \sigma^2_{\mathrm{wfs}} + \ldots \tag{1.86}$$

The two metrics are linked through the Maréchal approximation expressed as follows:

$$\mathrm{SR} \sim e^{-\sigma^2_{\mathrm{WFE}}} \tag{1.87}$$

It has been shown that this approximation holds exactly in the most common AO case of Gaussian phase residuals and it is a good approximation for many other distribution laws [52]. To conclude, this relation allows to design and quantify the expected performance of an AO-assisted system, linking the phase residual variance σ^2_{WFE} and the SR.

1.3 Multi-conjugate adaptive optics systems

As discussed so far, we describe the basic principle of a classical AO system. These systems, characterised by a single WFS and a single DM are known as Single-Conjugated AO (SCAO) systems. As seen in Sec.1.2.5, SCAO systems are strongly affected by anisoplanatism, which limits the performance of the AO correction to a narrow fields of view. To overcome this problem, the concept of Multi-Conjugate AO (MCAO) has been proposed in 1988 by Beckers[53]. With reference to Figure 1.17, this system foresees the use of multiple GSs to perform a 3D measurement of the turbulent volume and of multiple DMs conjugated to different altitudes to compensate for different layers of the atmosphere. Particularly, it has been proved

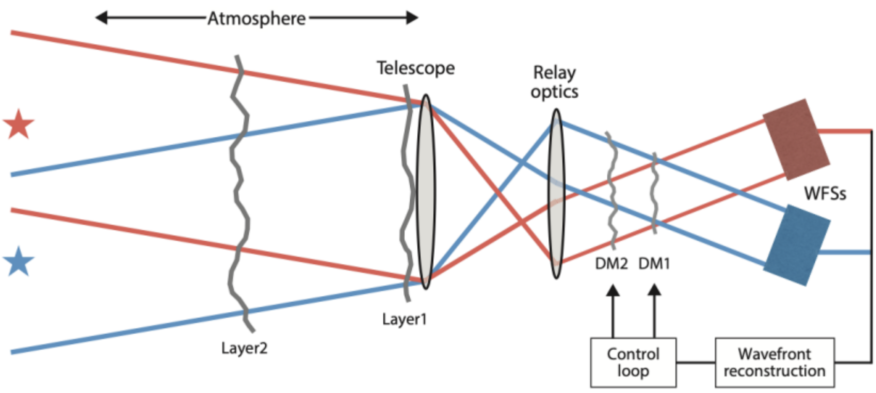

Figure 1.17. Conceptual scheme of a MCAO system (from Rigaut et al. [3]). The atmospheric turbulent volume is probed by multiple WFSs (the two in the figure), each sensing a different GS. The measurements are processed through tomographic techniques and the correction phase is projected onto multiple DMs (the two in the figure), optically conjugated at various atmospheric layers above the telescope.

[54] that the conjugation of N DMs to N layers of atmospheric turbulence can increase the isoplanatic patch identified by θ_0. In this case, the anisoplanatic error can be written as:

$$\sigma^2_{aniso} = (\frac{\theta}{2\theta_0 N})^{5/3} \tag{1.88}$$

The latter equation shows that the isoplanatic angle is reduced by a factor $2N$ with respect to the case of a single DM conjugated to the ground seen in Eq. (1.84). The compensation for various turbulent layers requires the measurement of the atmospheric layers conjugated at each DM, that is obtained through the tomography technique. Different methods have been proposed for the tomographic reconstruction relying on multiple GSs, considering either a zonal approach [55] or a modal approach

[56]. These works involved the use of LGSs only, thus overcoming the AO problem of limited sky coverage. However, the Tip-Tilt indetermination problem associated with LGS-based wavefront sensing has also led to the use of NGSs. Typical configurations use NGSs for Tip-Tilt measurements and LGSs for sensing higher orders of distortion. Such configurations do not reintroduce the sky coverage problem since the small number of modes that have to be measured by the NGS WFSs allows for a fainter NGS limiting magnitude.

To date, the Gemini Multi-conjugate Adaptive Optics System (GeMS) [57] at the Gemini South telescope is the only on-sky operating MCAO system, while new modules are currently being designed and developed. Examples includes MAVIS[58] at VLT, the Narrow-Field InfraRed Adaptive Optics System (NFIRAOS) [59] for the Thirty Meter Telescope (TMT), and MORFEO [4] at ELT.

1.3.1 Tomographic reconstruction

In the present discussion, we review the basic concepts to retrieve the volumetric distribution of atmospheric turbulence from a set of wavefront measurements in different directions. Particularly, we will follow Ragazzoni et a.[56], that provides a modal approach showing that the deformations of several DMs can be controlled by measuring a certain number of Zernike modes on LGSs. The same analysis can be applied to NGSs as well.

We assume that the wavefronts from M GSs are sensed by M different WFSs through the telescope entrance pupil, which has a diameter of D. It is assumed that the incoming wavefront is perturbed by N layers located at different altitudes. The configuration geometry is shown on the left panel of Figure 1.18, while on the right panel of the same figure, the geometry of the footprints projected onto a single layer j is shown, where the meta-pupil is defined as the circular region encompassing all of the GS beams. Assuming that θ is the radius of the technical FoV (i.e. the FoV identified by the GSs asterism), the size of the meta-pupil on a layer j is $D + 2\theta\, H_j$, where H_j is the altitude of the layer. Depending on whether NGSs or LGSs are considered, the beam footprint diameter is equal to D in the case of NGSs, while becomes smaller and it changes depending on the altitude of the layer in the case of LGSs.

The wavefront in the direction of the ith GS can be expanded into a sum of n Zernike polynomials as follows:

$$\varphi_{\mathrm{GS}_i} = \begin{bmatrix} a_2 \\ a_3 \\ \vdots \\ a_n \end{bmatrix} . \tag{1.89}$$

where the piston is neglected since is not accessible and where Tip and Tilt modes have been included in order to extend the analysis to the case of NGSs as well. Particularly, φ_{GS_i} is the modal expansion of the wavefront coming from the ith GS direction, integrated over the layers. thus it can be expressed as:

$$\varphi_{\mathrm{GS}_i} = \sum_{j=1}^{N} \varphi_{\mathrm{GS}_{ij}} , \tag{1.90}$$

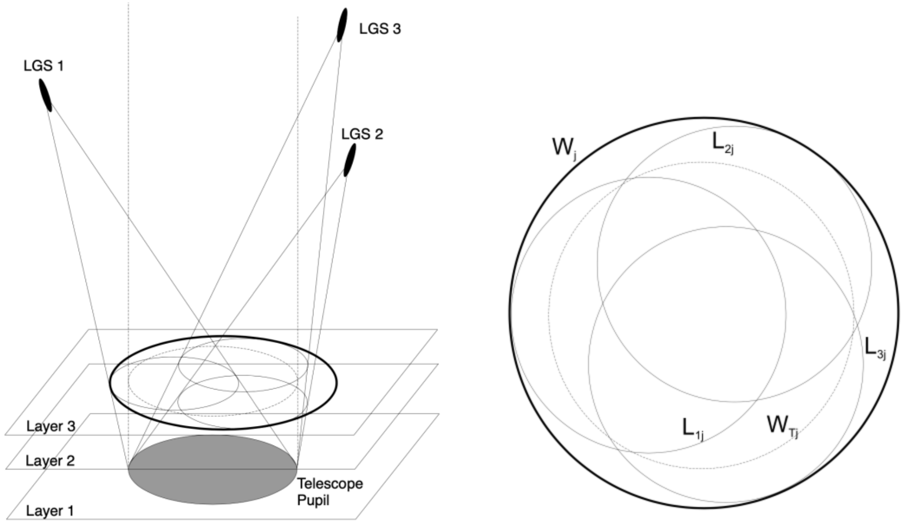

Figure 1.18. Geometrical configuration of modal tomography. On the left, the wavefronts from three LGSs pass the 3 turbulent atmospheric layers before arriving at the entrance pupil. On the right, the geometry of the beams' footprints on a layer j. L_{ij}, with $i = 1, 2, 3$, represents the beam from the ith GS (i.e. φ_{GS_i}). W_j is the meta-pupil (i.e. φ_{DM_j} and W_{T_j} j is the footprint from the scientific object that is assumed on-axis (φ_{O_j}). Both images are from Ragazzoni et al. [56].

where $\varphi_{\mathrm{GS}_{ij}}$ is the expansion of the wavefront from the ith GS on a single layer j and can be related to the wavefront defined on the meta-pupil as follows:

$$\varphi_{\mathrm{GS}_{ij}} = \left(P_{\mathrm{DM}}^{\mathrm{GS}}\right)_{ij} \varphi_{\mathrm{DM}_j} \,, \tag{1.91}$$

where $\left(P_{\mathrm{DM}}^{\mathrm{GS}}\right)_{ij}$ is a matrix of size $n \times n$ that contains information about the geometry between the meta-pupil and the footprint, while φ_{DM_j} is the expansion of the wavefront on the meta-pupil. We considered having a DM conjugated to each layer, with the same number of modes reconstructed on each layer as were measured by each WFS. combining Eq(1.90) and Eq.(1.91), we obtain:

$$\varphi_{\mathrm{GS}_i} = \sum_{j=1}^{N} \left(P_{\mathrm{DM}}^{\mathrm{GS}}\right)_{ij} \varphi_{\mathrm{DM}_j} . \tag{1.92}$$

The latter equation, applied to all the GSs, can be expressed in matrix form including all the N layers and the M GSs in the following relation:

$$\begin{bmatrix} \varphi_{\mathrm{GS}_1} \\ \varphi_{\mathrm{GS}_2} \\ \varphi_{\mathrm{GS}_3} \\ \vdots \\ \varphi_{\mathrm{GS}_M} \end{bmatrix} = \begin{bmatrix} P_{11} & P_{12} & \cdots & P_{1N} \\ P_{21} & P_{22} & \cdots & P_{2N} \\ P_{31} & P_{32} & \cdots & P_{3N} \\ \vdots & \vdots & \ddots & \vdots \\ P_{M1} & P_{M2} & \cdots & P_{MN} \end{bmatrix} \begin{bmatrix} \varphi_{\mathrm{DM}_1} \\ \varphi_{\mathrm{DM}_2} \\ \varphi_{\mathrm{DM}_3} \\ \vdots \\ \varphi_{\mathrm{DM}_N} \end{bmatrix} . \tag{1.93}$$

That in a compact form becomes:

$$\boldsymbol{\varphi}_{\mathrm{GS}} = P_{\mathrm{DM}}^{\mathrm{GS}} \boldsymbol{\varphi}_{\mathrm{DM}} . \tag{1.94}$$

This final relation has the same form as seen in Eq(1.74): it represents the relationship between the wavefronts propagated to the WFSs and those to be applied on the DMs via the interaction matrix $P_{\mathrm{DM}}^{\mathrm{GS}}$. However, in contrast to classical AO reconstruction, the interaction matrix contains, for each layer, information on how all WFSs react to a given Zernike mode on a meta-pupil in altitude.

Similarly, the wavefront expansion φ_{DM_j} from the meta-pupil can be projected onto the smaller on-axis footprint of the scientific target on the jth layer as follows:

$$\varphi_{O_j} = \left(P_{\mathrm{DM}}^{O}\right)_j \varphi_{\mathrm{DM}_j} \, , \tag{1.95}$$

leading to the compact form:

$$\boldsymbol{\varphi}_O = P_{\mathrm{DM}}^{O} \, \boldsymbol{\varphi}_{\mathrm{DM}} \, . \tag{1.96}$$

The dimensions for P_{DM}^{GS} are $(M\,n) \times (N\,n)$, while for P_{DM}^{O} are $n \times (N\,n)$. These matrices contain coefficients that depends on the geometry of the problem.

To conclude, as seen in Sec1.2.4, as long as $M \geq N$, the interaction matrix P_{DM}^{GS} can be inverted to infer the tomographic reconstructor:

$$W_{\mathrm{tomo}} = \left((P_{\mathrm{DM}}^{\mathrm{GS}})^T P_{\mathrm{DM}}^{\mathrm{GS}} \right)^{-1} (P_{\mathrm{DM}}^{\mathrm{GS}})^T . \tag{1.97}$$

Unseen modes and minimum mean square estimator

The geometrical configuration of the GSs asterism can introduce a crucial limitation of the tomographic reconstruction process of the turbulent volume, which is described by the problem of the *unseen modes*. These occurs when wavefronts from different atmospheric layers cancel each other out in the direction of the WFSs, but not in the direction of the science camera, leading to a degradation of the image quality. Figure 1.19 describes the nature of these modes. Particularly: the wavefront aberrations are measured by two WFSs sensing at two different directions, while the science camera operates on the on-axis direction. In the configuration shown in the latter figure, the sum of the phase perturbations induced by the turbulent layers is zero in the GSs directions. Therefore, the WFSs only provide piston measurements, and no information on phase deformation is available. Thus, these aberrations are not estimated in the tomographic reconstruction process. Clearly, these modes do not play any role in the GS directions, but they lead to wavefront distortions in other directions (i.e. the one related to the science target). This limits the capability of MCAO to provide a uniform correction all over the FoV. In addition, unseen frequencies represent a strong limitation for the pure LSE reconstructor typically used in SCAO systems. Indeed, the interaction matrix coefficients approach zero for such frequencies, resulting in overamplification of the noise within the inversion operation. Furthermore, the *badly seen* frequencies sets constraints on the LSE reconstructor. For these frequencies, the measurement is close to zero and falls within the noise of the WFSs. Therefore, the same problem applies as for the unseen frequencies. A possible solution to overcome the noise amplification is to rely on a truncated LSE (T-LSE) reconstructor (namely the T-SVD seen in Sec1.2.4). However, this results in uncorrected frequencies. Moreover, the truncation is selected using a trial-and-error approach, which may not be straightforward for real systems.

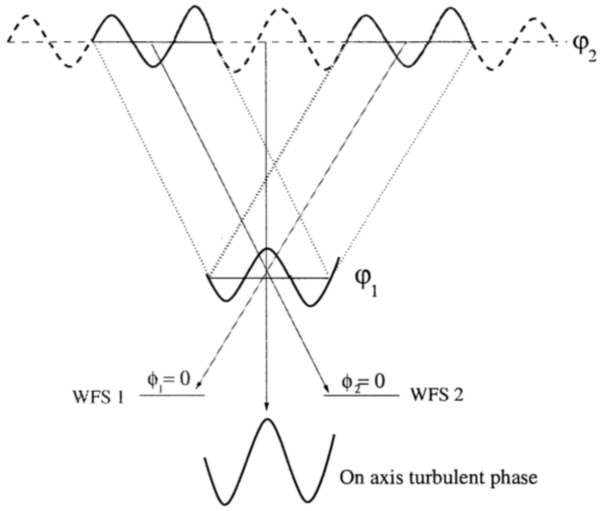

Figure 1.19. Geometrical schematic representation of the problem of the *unseen modes.* Two WFSs measure turbulent distortions from two different GSs. The sum of the phase perturbations on the two layers is zero in each GS directions and therefore provides zero signal on each WFS. However, the wavefront deformations do not cancel out in the on-axis direction. Consequently, the modes unseen by the WFSs may still degrade the correction in other directions. From Fusco et al.[8].

In this context, another solution was proposed, performing the reconstruction through the Minimum Mean Square Estimator (MMSE)[12]. This estimator minimises the residual phase variance in each reconstructed layer by comparing the actual and estimated phases:

$$\sigma^2_{\mathrm{res}} = \langle|\varphi_{\mathrm{turb}} - W_{\mathrm{tomo}}(P_L^{\mathrm{GS}}\,\varphi_{\mathrm{turb}} + \varphi_{\mathrm{n}})|^2\rangle\,, \tag{1.98}$$

where φ_{turb} is the turbulent phase and P_L^{GS} is the interaction matrix that projects the turbulent layers seen in the GSs directions in the pupil plane ($P_L^{GS} = P_{DM}^{GS}$ if we consider a DM conjugated at each layer). Differently from Eq.(15) in Neichel et al. [12], we assumed a direct measurement of the phase by setting M = 1, with M the matrix that models the wavefront sensing operation. The minimization process leads to the following expression for the MMSE reconstructor:

$$W_{\mathrm{MMSE}} = \left[(P_L^{\mathrm{GS}})^T (C_{\varphi_n})^{-1} P_L^{\mathrm{GS}} + (C_{\varphi_t})^{-1}\right]^{-1} (P_L^{\mathrm{GS}})^T (C_{\varphi_n})^{-1}\,, \tag{1.99}$$

where C_{φ_t} is the covariance of the turbulent phase and C_{φ_n} is the covariance of the noise. This reconstructor includes prior knowledge of the phase statistics and noise power spectrum by means of C_{φ_t} and C_{φ_n}. The noise term can be factorized under the assumption of same noise σ_n^2 for all GSs and x and y directions and Eq. (1.99) can be rewritten as:

$$W_{\mathrm{MMSE}} = \left[(P_L^{\mathrm{GS}})^T P_L^{\mathrm{GS}} + \sigma_n^2\,(C_{\varphi_t})^{-1}\right]^{-1} (P_L^{\mathrm{GS}})^T. \tag{1.100}$$

where the inverse of the SNR appears, namely $\sigma_n^2\,(C_{\varphi_t})^{-1}$.

Compared to the TLSE, the MMSE reconstructor does not require any truncation. Indeed, through the regularization term $\sigma_n^2\,(C_{\varphi_t})^{-1}$, the MMSE reconstructor weights the noise propagation and is capable of optimising the reconstruction in function of the SNR. Particularly: in the case of frequencies with a good SNR, the MMSE and TLSE are equivalent, while in the case of low SNR the inverse of the interaction matrix is weighted by the regularization term, avoiding noise amplification.

However, an issue comes with the MMSE tomographic reconstruction approach: although it uses a priori information on turbulent phase statistics, it has to deal with closed-loop configurations where the WFSs are after the DMs, so they only see residual turbulence that does not obey the same statistics. To overcome this problem, the concept of pseudo open-loop control (POLC) has been introduced [10]: the idea is to reconstruct virtual open-loop measurements using a combination of closed-loop measurements and DMs' shape.

1.3.2 Limitations of multi-conjugate adaptive optics

MCAO systems also have their intrinsic sources of error and limitations, in addition to those inherited from SCAO systems (as seen in Sec.1.2.5, except for angular anisoplanatism). In the following, we briefly describe the main error contributions, without entering into detail on the limitations due to the use of LGSs (that is beyond the interest of the present work). In this context, a general review is provided by Rigault et al. [3].

Generalized fitting error

As seen in Sec.1.3.1, we ideally assumed to have a DM conjugated at each turbulent layer. However, this is not the case for real systems that rely only on a limited number of DM to compensate for the atmospheric turbulent volume. The residual wavefront due to the uncorrected layers leads to the generalized fitting error.

Tomographic error

Using multiple GSs does not ensure complete coverage and measure of the turbulent volume. Some of the turbulence above the telescope pupil will always be probed by only one GS: this limits the tomography as it cannot infer the altitude at which the perturbation is located in this part of the beam. Another limitation of tomography arises from unseen modes, as already discussed in Sec.1.3.1.

Generalized aliasing error

Turbulent layers above and below the altitude control domain of the MCAO system can be seen and misinterpreted as layers within the control domain, causing an error commonly known as generalised aliasing error. Unlike classical spatial aliasing (seen in Sec.1.2.5), which is caused by the WFS, generalised aliasing is caused by the tomographic process.

1.3.3 MORFEO: the MCAO module for ELT

MORFEO [4][7] is the MCAO system of the 39-m ELT [5] that will provide large diffraction-limited correction to the near-infrared Multi-AO Imaging Camera for Deep

Observations (MICADO) [6] and, as lately confirmed, to High Angular Resolution Monolithic Optical and Near-infrared Integral field spectrograph (HARMONI) [21]. The primary observing mode of MICADO is astrometric imaging with either a large FoV of 50×50 arcsec, or a small FoV of 18×18 arcsec, with wavelength coverage from 0.8 to 2.4 μm [6]. Jointly with the MICADO consortium, MORFEO will provide a SCAO system as well.

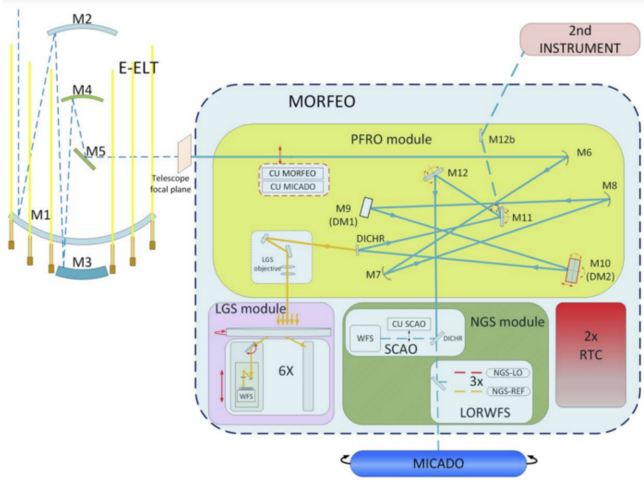

Figure 1.20. Overview of MORFEO related to ELT and the science instruments, MICADO and HARMONI (2nd instrument diagram). In the figure, MORFEO is divided into the post-focal relay optics (PFRO), the LGS and the NGS modules. The PFRO contains two post-focal DMs (PFDMs) and a dichroic that feeds the six LGS WFSs in the LGS module. Light emerging from the PFRO module is directed to the NGS module, where it is split between the NGS WFSs (LORWFS in the diagram) and the MICADO instrument. Measurements from the LGS and NGS WFSs are collected by MORFEO RTC, which drives the DMs (M4/M5 and the two PFDMs). From Ciliegi et al.[60].

Figure 1.20 provides an opto-mechanical overview of MCAO module. Particularly, MORFEO consists of an optical relay that re-images the telescope's focal plane for the scientific instruments. Supported by an optical bench mounted on the telescope's Nasmyth platform in a gravity-invariant configuration, shown in Figure 1.21, the relay consists of six mirrors and a dichroic beam splitter that separates the light for the science path from the light for the LGS WFSs. MORFEO will provide two DMs (DM1 = M9 conjugated at 6–12 km and DM2 = M10 conjugated at 17–20 km) for the optical relay that will work alongside the adaptive (M4)[61] and Tip-Tilt (M5) mirrors of the ELT.

The tomographic reconstruction relies on measurements from three NGS WFSs and six LGS WFSs. The former are 2×2 SHWFSs working in the H band, measuring five modes (Tip, Tilt, focus, and the two astigmatisms) at a frame rate of 100–1000 Hz on stars with a H-band magnitude of up to 21. The latter are 68×68 SHWFSs sensing the higher orders of distortion at a frame rate of 500 Hz. Up to three NGSs can be selected within a technical FoV with a diameter of 160 arcsec, while the LGS asterism radius is fixed at 45 arcsec for any telescope elevation. The adaptive correction is provided by the ELT's M4 and the two MORFEO DMs, which control more than 5000 modes.

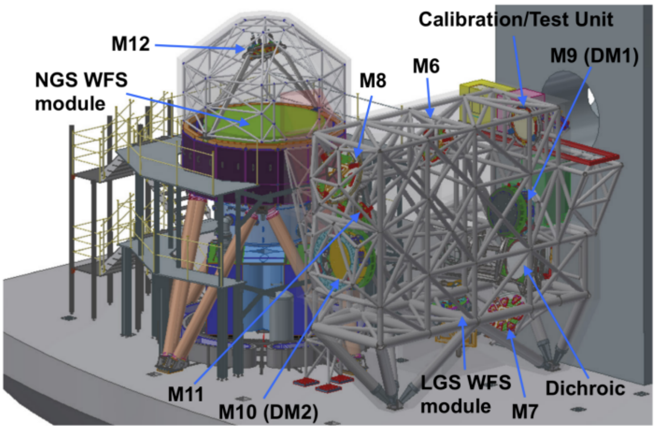

Figure 1.21. General overview of MORFEO as installed on the ELT's Nasmyth platform. From [7].

Challenges and critical aspects of reconstruction and control

The complexity of MORFEO system introduces new significant challenges compared to the operational AO system, that needs to be tested and prototyped before its integration and troubleshooting on sky. Particularly, it concerns the design and validation of the reconstruction and control algorithms.

As discussed in Sec.1.3.1, one of the major limitations to MCAO systems is represented by *unseen modes*. To overcome this problem, MORFEO will implement a MMSE tomographic reconstructor that will be included in a Pseudo-Open Loop Control (POLC) [10]. To date, only few MCAO systems, like GEMS [11], implement such a tomographic reconstruction algorithm.

Furthermore, a peculiar aspect of MORFEO is characterised by the high geometrical variability of GS footprints, DMs and WFSs projection on the reconstructed layers. With reference to Figure 1.22, the footprints change continually with telescope azimuth and elevation of the telescope, the instantaneous NGS asterism, sodium-layer distance, and any small telescope–Nasmyth platform misalignment. As a result, while the telescope tracks a target, NGS footprints rotate relative to LGS ones, the post-focal DM (pfDM) actuator grid rotates with elevation, and the LGS meta-pupil size varies with zenith angle. Basically, the only static geometry is the LGS footprint over M4.

This effect introduces complexity in the definition of wavefront reconstruction and DMs actuation. Indeed, the actuator-subaperture matching is not constant. Accurate actuator matching is critical for the AO performance: a mismatch of 1/10 DM pitch adds several tens of nm WFE, and in the case of MORFEO 30 nm RMS WF is allocated to this source of error [62]. As a consequence, a single fixed interaction matrix becomes useless, requiring continuous recomputation/inversion at the expense of a heavy and prohibitive computational load for the RTC. To overcome this problem, MORFEO decouples reconstruction from DM actuation by using two projections per DM [62]. First, it projects the reconstructed layers onto an ideal DM-altitude surface (where temporal filtering is applied), and then it maps that surface onto the actual DM actuators/modal basis, accounting for the current

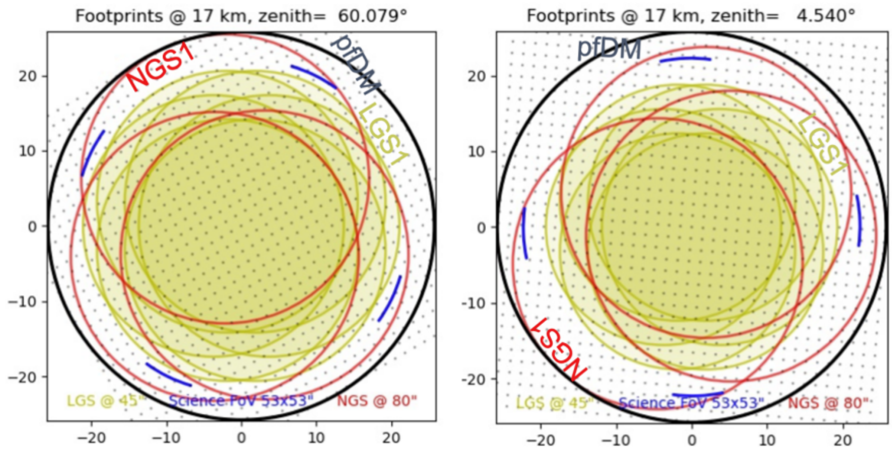

Figure 1.22. Evolution of the footprint and post-focal DM (pfDM) actuators projection on the meta-pupil at 17km, while the telescope is tracking a target. The six yellow circles show the footprint of the LGS, whose centres are fixed because the LGS module is derotated to track the telescope pupil. However, the radius depends on the distance to the sodium layer. The three red circles show the footprint of a generic, roughly equilateral NGS asterism that follows the sky rotation and flips when the telescope crosses the meridian. The grid of grey dots represents the projection of the pfDM actuators onto the layer, which rotates with the telescope elevation, as there is no pupil derotation before the MORFEO PFRO. From Busoni et al. [62].

alignment and magnification.

These are only a few of the main factors that make MORFEO's reconstruction and control algorithms particularly challenging (for further details, see Busoni et al.[62]). To address them, it requires dedicated test facilities to test and validate MORFEO's reconstruction and control algorithm before its system integration and to minimise troubleshooting on-sky.

However, as mentioned in Sec.1.2.2, developing realistic telescope simulators for MORFEO and any other next-generation AO supported instrument for extremely large telescopes (ELTs) is complex due to the optical constraints imposed by the Lagrange invariant. This principle sets a fundamental limitation on how telescope optics can be re-scaled in a laboratory test-bench. For instance, MORFEO's technical field of view is ∼150 arcseconds over a 40m pupil: if this system were scaled down to a 40mm pupil, the equivalent field of view would be about 42 degrees, which is impractical to reproduce on an optical bench. As a result, it is challenging to create a fully accurate re-scaled simulator for ELT AO systems.

For all these aspects, it is crucial to develop simplified test facilities that reduce complexity and still allow for assessing the performance and critical aspects of next AO facilities on ELTs, before their integration and troubleshooting on sky. To conclude, MORFEO is being developed by an European consortium led by INAF (the Italian National Institute for Astrophysics), with the Arcetri Astrophysical Observatory in Florence playing a major role in its design and implementation [7]. The present work, in collaboration with the AO group of the Arcetri Astrophysical Observatory, is part of the MORFEO work package to test its reconstruction and control algorithms.

Chapter 2

SLM-based test-bed setup for wide field AO simulations

As discussed at the end of the previous chapter, the next generation of AO facilities on extremely large telescopes shows new and critical aspects compared to classical SCAO systems, that need to be tested and prototyped before their integration and on-sky troubleshooting. Among these facilities, the upcoming MCAO module of ELT, MORFEO, is not excluded. Despite the limitations imposed by the development of a 40 m telescope simulator in laboratory, is crucial to develop simplified test facilities that reduce complexity and still allow for assessing the performance and critical aspects of upcoming AO modules on ELTs.

In this context, the present chapter describes the SLM-based test-bed setup, aimed to test MORFEO's reconstruction and control algorithms. Particularly, in Sec.2.1 we describe the working principle of the test-bed, aimed to simulate MCAO loop through a SLM-based SCAO setup, showing how the numerically simulated residual phase operates alongside the hardware. In Sec.2.2, we provide a summary of the software supporting tools used for AO simulations and control the devices on the test-bench, to reproduce hardware in the loop simulations. Finally, in Sec.2.3 and Sec.2.4, we show the optical layout of the test-bench, providing a description of the SLM and sensors present on the bench.

2.1 MCAO decomposition into a SCAO loop

As seen in Sec.1.3.3, MORFEO, due to its intrinsic nature and reconstruction and control aspects, is a complex system made of multiple WFS and DMs that operates simultaneously, and that are not feasible to reproduce in an AO test facility. However, several laboratory facilities have been developed [63] to simulate the simultaneous sensing of the residual phase on a wide field observations: by means of multiple phase correctors and WFSs on the optical bench, the test-bed simulates an actual MCAO system, at the expense of introducing complexity in the testing setup.

In this context, the present work was aimed at developing a test facility to test and validate the reconstruction and control algorithms foreseen for MORFEO, by breaking down the complex MCAO process into a simpler and sequentially executed SCAO test-bed and a numerical simulator. The goal was to design and test the needed software and hardware equipment to simulate the atmospheric turbulence sensed by each of MORFEO's 12 WFSs and the corresponding correction provided by the 3 DMs. This is performed by means of a single phase corrector, a single WFS, and a MMSE+POLC reconstructor, to reduce the complexity of the testing setup.

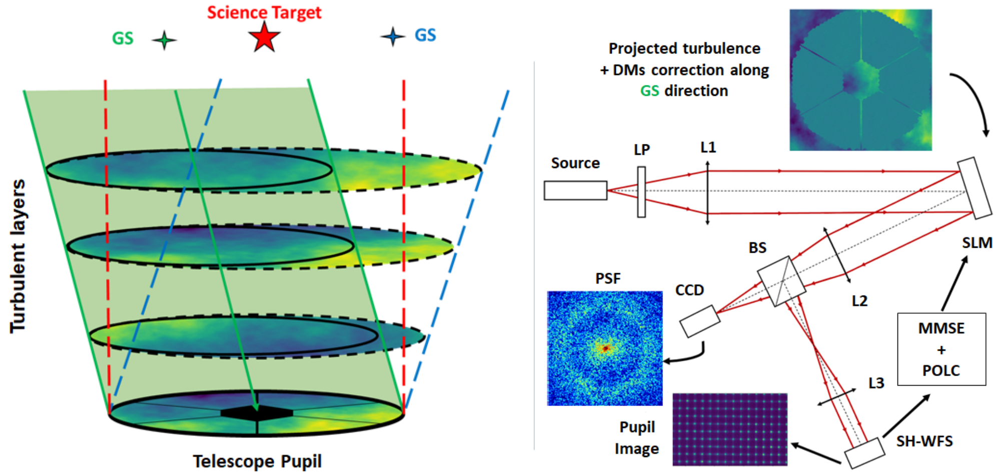

Figure 2.1. Scheme of the working principle of MCAO simulation sequentially decomposed in the SLM-based SCAO testbed. On the left, a visual representation of the numerical computation of the residual phase that is sequentially propagated on the telescope pupil for the GS and science target directions. It is essentially a sequential coring of the turbulent volume along the directions of all the GS and target in the FoV. For the sake of clarity, the DMs conjugated layers are not shown. On the right, a schematic optical layout of the SCAO test-bench in which the residual phase in a given GS or science direction is applied on the SLM and sensed by the WFS. Once the slopes in all the GS direction are measured, the MMSE+POLC reconstructor is used to infer the DMs compensation across the wide field. Finally, the CCD checks the PSF quality of the correction, once the residual phase along a direction of the science field is applied on the SLM.

Figure 2.1 shows the working principle of the SCAO hardware-in-the-loop for MCAO simulation. The test-bench includes a SHWFS to sense the wavefront aberrations, a phase modulator (SLM in the figure) to inject and compensate for the disturbances, and a scientific camera to analyse the correction performance in the science field of the simulated wide FOV, through the resulting PSF. In this setup, MORFEO's wide field is simulated through a sequential decomposition approach: the projection of the atmospheric turbulent volume and the related residual phase along the line of sight of each MORFEO WFS is computed and applied to the phase modulator, one direction at time, and the corresponding residual wavefront is measured by the SHWFS. These measurements are then used to compute the tomographic reconstruction, which defines the commands for ELT's M4 and MORFEO's DMs. To simulate the correction for a given direction in the science field, the integrated aberrations from the turbulent layers and the corresponding DMs corrections along that line of sight are applied to the phase modulator (i.e. the residual phase in the science direction), and the resulting PSF is acquired on the scientific camera. The whole process is repeated iteratively by shifting the turbulent layers previously simulated, in order to take into account the temporal evolution effects between successive iterations of the control loop.

By discretising the MCAO system in such a way, the test facility essentially reconstructs the wide field MCAO correction loop within a simplified and sequentially executed SCAO test-bed, allowing a practical, step-by-step evaluation of MORFEO's correction capabilities. This approach allows us to focus on critical aspects of the reconstruction and control algorithms in a controlled environment, without the need to fully replicate the real system (with multiple WFSs and DMs) capable of sensing the entire wide field all at once. Furthermore, this hybrid approach of using hardware alongside simulation enables more reliable system validation by addressing problems close to those in the real system like WFS noise, alignment, and sensor imperfections, providing more reliable performance validation compared to pure end-to-end simulations. As will be discussed in the following section, we used a Spatial Light Modulator (SLM) to inject in the SCAO test-bed the expected residual phase in the decomposed MCAO simulation.

To conclude, the present SLM-based testbed is a promising and useful test facility to inspect all the critical aspects of MORFEO's reconstruction and control system, discussed in Sec.1.3.3. Furthermore, it can be used to prototype and characterise the WFSs planned for MORFEO, before going on sky and to test novel techniques foreseen for the next generation of AO modules, such as the so-called *super-resolution* [64]. This technique combines slightly shifted WFS measurements (e.g. through micro-dithering of the WFS) to reconstruct spatial components beyond the former sampling of the single fixed subaperture, decoupling its size from the effective resolution and mitigating losses due to edge vignetting. In other words, super-resolution reduces the aliasing error seen in Sec.1.2.5 and Sec.1.3.2, improving the reconstruction at higher frequencies due to the finer sampling of the wavefront.

2.2 Support software for hardware-in-the-loop simulations

In this section, we briefly describe the main software and IT tools used to integrate the SCAO test-bench hardware into MCAO decomposed simulations. In particular, for the hardware control and interface, we rely on PLICO [65], while for the numerical simulations of AO loops we use SPECULA [66]. Both are Python packages developed by the AO INAF Arcetri group, to which I have contributed to the development and testing of the hardware integration on the end-to-end AO simulations and the SLM control. These packages are available on GitHub [67][68].

2.2.1 AO numerical simulator: SPECULA

SPECULA is a Python package for AO end-to-end simulator, based on its IDL precursor PASSATA [69]. It adopts a modular, object-oriented design in which "processing objects" exchange typed "data objects", enabling closed-loop pipelines to be easily configured. The former represents the main active components of the AO loop, such as turbulence (with its evolution and propagation to the telescope pupil), the slope computer (with centroid algorithms to estimate slopes from the WFS frame), the reconstruction (with modal or zonal wavefront reconstruction) and the DM (with correction application and its effects on the conjugated layers), among others. The latter represents the input and output of each processing object triggered on the simulated loop (e.g. phase of the propagated electric field, slopes, interaction and reconstruction matrices). SPECULA provides an explicit time handling of the simulated AO loops. Based on a fixed time step, it allows for modelling processing objects characterised by fixed delays, so that different blocks may run at different rates in the simulated loop. This is exactly what happens in a real AO system and specifically, as seen in Sec.1.3.3, how MORFEO will operate relying on a complex control system with the multiple WFS and compensation components that work at different frame rates and characterised by specific delays. As mentioned, SPECULA inherits the philosophy of PASSATA. Its precursor is a Monte-Carlo AO simulator originally developed in an IDL environment. Compared with PASSATA, SPECULA keeps the same object-oriented approach but implements it in Python with optional GPU acceleration, enabling faster simulations. For these reasons, it represents a suitable package for simulating AO loops in complex systems such as the one of MORFEO.

In the present work, we developed an ad hoc processing object for SPECULA in order to couple end-to-end loop simulations with the real hardware on the SCAO test-bench.

2.2.2 Hardware interface & control: PLICO

Python Laboratory Instrumentation COntrol (PLICO) is a framework designed to assist developers in instrument control applications, with a focus on interfacing with the most frequently utilized devices in adaptive optics laboratories [65]. It is written in Python and follows a distributed client-server model: each device (e.g., deformable mirrors, cameras, motors, interferometers) is wrapped by a small server process that talks and interfaces to the vendor's device driver locally, while remote Python clients connect over ZeroMQ using a simple and standardized API. This architecture hides the devices' specific interfaces, allowing multiple devices to be synchronized and making adding new hardware on a given testing setup straightforward. In practice, the PLICO provides specific device packages, such as *plico_dm* and *pysilico*, allowing the client to control the phase modulator and cameras with primitives and straightforward commands (like `get_shape()/set_shape()` for DM and `getFutureFrames()` for the detectors). Similar modules are available to control for motors and WFS, such as interferometers and SHWFSs, and perform DM calibrations. Finally, PLICO provides a detailed log history that tracks all the process between the client request and the device response. These allow to verify the client-server communications to the hardware and debug any related errors.

In the present work, the SCAO test bench hardware is controlled through PLICO. Particularly, my contribution concerns the development of the software package to interface and control the SLM, based on the Software Developer Kit (SDK) provided by the manufacturer. It allows to apply phase patterns on the SLM's display from a user-defined image wavefront map. This package is available on GitHub and has been integrated into PLICO.

To conclude, it is worth stating that PLICO is not designed to control an AO systems at frame-rates of $\sim$ 1kHz. However, for the present work, we are not interested in reproducing real-time compensation of the turbulence. As previously seen in Sec.2.1, the real system, in which a measure of the 3D turbulent volume is performed "simultaneously" (net to the different frame rates and delays) by the foreseen MORFEO's WFSs at a given time is sequentially decomposed by coring the atmospheric turbulence in each direction of the GSs in the entire FoV.

2.3 Test-bench optical layout

The test-bench is designed to reproduce AO-assisted telescope observations in a controlled laboratory environment. The design emphasizes simplicity of the testing setup, aiming to reduce the complexity of a real MCAO system and focusing on aberrations injection and compensation, as previously discussed. Figure 2.2 shows the optical layout of the SLM-based SCAO testbed.

A collimated beam is directed onto a Spatial Light Modulator (SLM), which acts as a phase modulator. In this configuration, the SLM plays the role of the telescope pupil: it can introduce aberrations, emulating atmospheric turbulence, and simultaneously provides for their compensation, reproducing the correction of a simulated deformable mirror. On the SLM is mounted a circular aperture stop of ~ 10.5 mm of diameter. The SLM reflected beam is then split into two paths by a 50:50 Beam Splitter (BS): one dedicated to the wavefront sensing and the other to the science camera, for focal plane analysis.

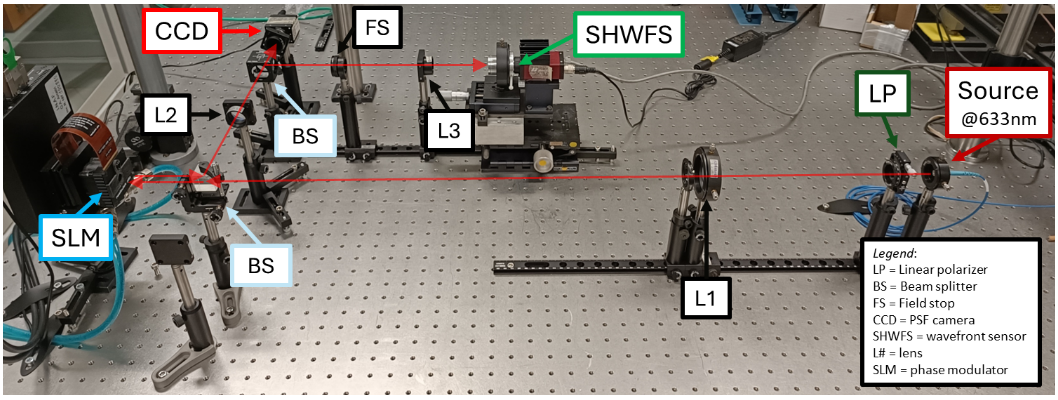

Figure 2.2. A picture of the SLM-based SCAO test-bench, in the INAF Arcetri AO laboratory. The red arrows represent the optical path. It is worth noting that the beam component of the first beam splitter that is once reflected (when the collimated beam comes from the source) and then transmitted (when the beam comes from the SLM) are not shown in the figure, since they do not actively contribute to the loop.

The collimated beam is generated by means of a lens (L1), with the laser source positioned at its focal plane. Since the SLM works with polarised light (as will be discussed in Sec.2.4.3), the source is a linearly polarised laser at 632.8 ± 0.2 nm coupled with a polarisation-maintaining single-mode fibre. A linear polariser (LP) is placed between the fibre output and lens L1, to align the polarisation state of the collimated beam with the modulation axis of the liquid crystal cells of the SLM. As we will see in the following sections, the orientation of the polarisation optics is crucial to ensure efficient phase modulation.

The wavefront sensing path includes a relay of two lenses, L2 and L3, placed in confocal configuration. A field stop is located at the intermediate focal plane between these lenses to spatially filter unwanted light that could lead to non-linear response of the WFS. The lens pair L2–L3 reimages the SLM pupil onto the lenslet array of the Shack–Hartmann wavefront sensor (SHWFS). The lenslet array is positioned at the focal plane of L3, while the SHWFS detector is located at the focal plane of the microlenses, where the subaperture spots are formed. This configuration ensures that the wavefront aberrations introduced at the SLM pupil are accurately sampled by the SHWFS.

Finally, in the science path the lens L2 acts as the objective lens, focusing the SLM reflected beam onto the science camera, which is positioned at its focal plane. This allows direct inspection of the PSF, enabling the evaluation of image quality parameters such as full width at half maximum (FWHM) and Strehl Ratio (SR) and infer the correction performance of the simulated AO loop.

Table 2.1. Thorlabs achromatic doublets used in the test-bench. Each ID encodes the series and clear diameter (e.g., AC254 = 25.4 mm), and the nominal focal length (e.g. 250 = 250 mm), while the suffix denotes the AR coating. All three lenses use the A broadband AR coating (400–700 nm), with a manufacturer-specified an average reflectance $< 0.5\%$ per surface (i.e. total reflection losses $< 1\%$ per lens within the band).

Label	ID	Diameter [mm]	Focal Length [mm]
L1	AC508-300-A	50.8	300 ± 3
L2	AC254-250-A	25.4	250 ± 2.5
L3	AC254-150-A	25.4	150 ± 1.5

To conclude, all the lenses and BSs are provided by Thorlabs. Particularly, the lenses are achromatic doublets with an anti-reflecting coating from 400-700nm, with losses due to reflection of $\lesssim 0.5\%$ for each surface. In Table 2.1, we report the main characteristics of employed lenses. Further details on the SHWFS and science camera will be provided in the following sections.

2.4 Hardware equipment description

In this section, we provide a description of the key elements of the SCAO testbed, showing their nominal parameters according to the manufacturers' specifications. Particularly, we discuss the features of the Spatial Light Modulator, describing its working principle and the main differences compared to ordinary DMs used in AO testbed applications, highlighting both advantages and disadvantages.

2.4.1 Shack-Hartmann WFS

The WFS used in the SCAO test-bench is a custom assembled SHWFS: the sensor consists of a lenslet array mounted on a commercial detector.

Lenslet array

The lenslet array is the APO-Q-P144-R3.8 manufactured by Advanced Microoptics System Gmbh [70], whose layout is shown in Figure 2.3. It consists on an array of 46×46 lenslets with an aperture (i.e. the subaperture) size of $d_{la} = 144 \pm 1\,\mu$m. The array of lenses is made of fused silica (fused quartz). Each lens has a plano-convex profile with a curvature radius of $R = 3.80 \pm 0.11$ mm and lies on a square orthogonal configuration: thus each barycentre of the lens lies on a Cartesian grid at fixed pitch in both X- and Y- direction. As a first approximation, relying on geometrical optics, the focal length of a plano-convex lens in the air is given by:

$$f = \frac{R}{n-1} \tag{2.1}$$

where R is the curvature radius of the lens and n is its refractive index, that is a function of λ. According to Malitson et al. [71], the expected value for the refractive index at ambient temperature of the fused quartz at $\lambda = 633$ nm is $n = 1.475$. Thus, we expect that the lenslet array focal length f_{la} is of the order of ~ 8.3 mm. An optical ray-tracing of the lenslet array on Ansys Zemax OpticStudio confirmed that the lenslet array has a focal length of $f_{la} = 8.3 \pm 0.2$ mm at the bench working wavelength. The error is computed through the error propagation of Eq.(2.1), assuming n constant.

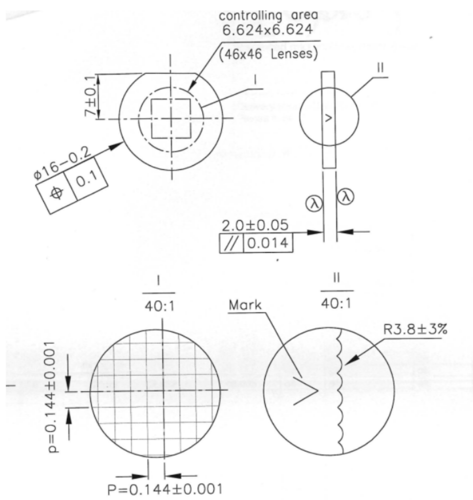

Figure 2.3. Lenslet array layout from the manufacturer's factsheet. The lenslet array is in an orthogonal configuration, with a square aperture and a convex profile. Credits to Advanced Microoptics System Gmbh [70].

Detector

The detector is the AVT/Manta G419 camera manufactured by Allied Vision. It is a CMOS with a global shutter of 2048×2048 pixel, with a pixel pitch of 5.5μm. The camera has a 12-bit ADC and a maximum frame-rate at full resolution of 28Hz. According to the manufacturer specifications, the camera gain is $g = 2.34e^-/\mathrm{ADU}$, while the read-out-noise (RON) is $\sigma_{RON} = 13.7e^- \equiv 5.85$ ADU rms.

Table 2.2. Geometrical parameters of the SHWFS.

Parameter	Symbol	Value	**Units**
Array size	–	6.624×6.624	mm
Number of subapertures	N_{sub}	46×46	–
Lenslet focal length	f_{la}	8.3 ± 0.2	mm
Lenslet pitch	d_{la}	144 ± 1	μm
Camera pixel pitch	p_{shwfs}	5.5	μm

Subaperture features

Table 2.2 summarises the geometrical features of the SHWFS. As will be discussed in Sec2.4.3, the actual pupil size is not defined by the mechanical aperture stop mounted on the SLM: it can be realised by the SLM itself, loading a proper pattern on its display to mimic the pupil effective aperture and obstruction. Thus, if we consider a circular pupil of 10 mm diameter (that is the actual pupil size reproduced by means of the SLM, as we will see in Sec.2.4.3), the relay L2 and L3 will compress the beam footprint of a factor 0.6. Thus, the actual illuminated subapertures are $\approx 42 \times 42$.

With reference to the latter table, it is worth noting that there is a mismatch between the subaperture size and the camera pixel pitch. As we will see, it will contribute to a bias signal on the measured slopes, which reconstructs an apparent Defocus (or Focus) Zernike mode, $Z_4 = \sqrt{3}(2\rho^2-1)$. Indeed, the mismatch introduces an isotropic scaling error in the slopes, which the reconstructor measures as radial dilation or contraction of the wavefront gradient, which can be mainly projected on radially symmetric modes, particularly on Z_4 (since $\partial Z_4/\partial\rho \propto \rho$). In Appendix A, we show how this mismatch is related to the apparent Defocus mode: this effect, if we consider a demagnified pupil due to the relay L2 and L3 with a radius of ~ 3 mm, results in a reconstructed coefficient $c_4 \sim 1.1\mu$m rms wf.

The subaperture pixel sampling is defined by the size of the field stop (FS) placed in the intermediate focal plane between the two lenses L2 and L3, as seen in Figure 2.2. Particularly, the FS diameter allows for avoiding nonlinearities on the SHWFS signals. These ones arise when a steep Tilt is sampled by a lenslet: in this case, the spot is not focused on-axis but on a pixel region below the next subaperture. To overcome this problem, the FS size has to be chosen such that its image realised by the L3 lens and the lenslet is less than the subaperture pitch d_{la}. Relying on the equation of thin lens and considering the relay made of L3 and the lenslet, the upper bound for the FS radius R_{FS} is given by:

$$R_{FS}^{max} = \frac{f_3}{f_{la}}\frac{d_{la}}{2} \approx 1.56\,\mathrm{mm} \tag{2.2}$$

In order to have a sampling of 25 pixels along the lenslet diameter, we set the iris of the FS to a diameter of $2R_{FS} \sim 2.485$ mm by means of a micrometer. To conclude, in the absence of any aberration, we expect that the generated spots on the WFS detector by the lenslet array are characterised by diffraction-limited FWHM of:

$$\text{FMHM} = 1.028 \frac{\lambda}{d_{la}} f_{la} = (37.5 \pm 0.9)\mu\text{m} \equiv (6.8 \pm 0.2)\,\text{px} \tag{2.3}$$

where the associated error is computed from the propagation error of the equation, assuming the pixel pitch is known.

To conclude, it is worth noting that the spatial sampling provided by the employed SHWFS becomes a limiting factor when probing turbulent wavefront over VLT- and (even more) ELT-like pupils in the visible. In particular, with 46 subapertures across the diameter, the corresponding subaperture pitch is $d = 8.2m/46 \approx 18$ cm on a VLT-pupil and $d = 40m/46 \approx 90$ cm on a ELT-pupil. These values are too large to properly sample a turbulent wavefront under typical visible-band conditions (e.g. $r_0 \sim 10$ cm, as seen in Sec.1.1), leading to spatial undersampling and, consequently, WFS aliasing (as discussed in Sec.1.2.5). However, as we will see in Sec.4.3, to mitigated this effect in the SCAO closed-loop simulations we restricted the turbulence strength to good-seeing conditions at the test bench wavelength, i.e. $r0 \gtrsim 20$ cm at 633 nm), for which $d \lesssim r_0$ on a VLT-like pupil. Furthermore, it is worth noting that the present work was aimed at the development and characterisation of the hardware and software support for the SLM-based testbech, which will be used to validate MORFEO's reconstruction and control algorithms. For this reason, we were not interested at this phase of the project to reproduce the same ELT's turbulence and sampling conditions, which would require the 68×68 SHWFS, like the LGS WFS foreseen for MORFEO (as seen in Sec.1.3.3).

2.4.2 PSF Camera

The science camera is the Prosilica GC 1350 manufactured by Allied Vision. It is a Sony ICX205 CCD with a global shutter of 1024×1360 pixel, with a pixel pitch of 4.65μm. The camera has a 12-bit ADC and a maximum frame-rate at full resolution of 20Hz. According to the manufacturer specifications, the camera gain is $g = 3.54e^-/\text{ADU}$, while the read-out-noise (RON) is $\sigma_{RON} = 8.5e^- \equiv 2.4$ ADU rms. If we consider a circular pupil of size $D = 10.028 \pm 0.003$mm, the expected diffraction-limited resolution is given by:

$$\text{FMHM} = 1.028 \frac{\lambda}{D} f_2 = (16.2 \pm 0.1)\mu\text{m} \equiv (3.49 \pm 0.03)\,\text{px} \tag{2.4}$$

To note, the uncertainty on D corresponds to SLM sampling quantisation, as will be discussed in Sec.2.4.3. Thus, the error on the FWHM is mainly due to the tolerance error of the objective lens L2.

2.4.3 Spatial Light Modulator

To reproduce the atmospheric disturbance and compensation on our test-bench, we are using a 1920x1152 XY Phase Series Spatial Light Modulator (SLM) manufactured by Meadowlark Optics. The device is a reflective Liquid-Crystal-on-Silicon (LCoS) modulator [13][72], typically used to modulate the phase of an incident beam.

Reflective SLMs of this type exploit the birefringent properties of nematic liquid crystal layers deposited on a silicon backplane, whose molecules are characterised

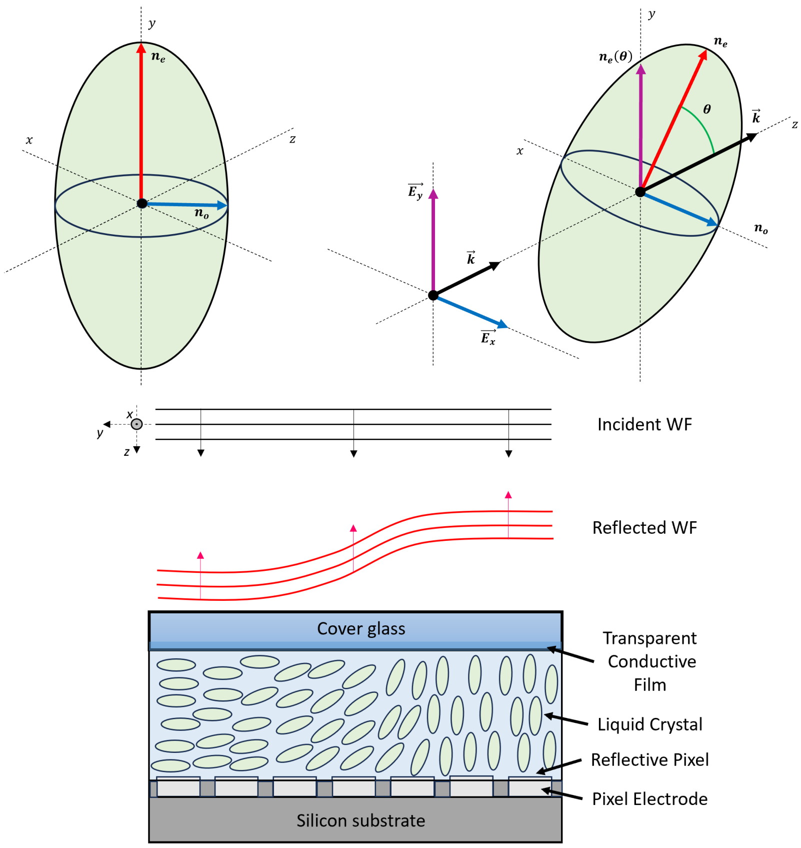

Figure 2.4. On the top panel, the incidence of the unpolarised beam on the LC molecule propagating in the z-direction. The optical axis of the LC device lies on the y-axis. Due to the voltage control, the extraordinary axis, n_e, of the LC molecule forms an angle θ with the incident wave vector $\boldsymbol{k} = \vec{k}$. Thus, the electric field component along the y-axis experiences an index of refraction $n_o < n_e(\theta) < n_e$. On the bottom panel, is shown the cross-section of a reflective SLM. As the applied voltage is zero, the LC molecules are aligned to the cover glass along the y-axis, the optical axis of the LC device. This results in the maximum phase retardation of the reflected wavefront, defined by n_e. As the applied voltage increases, the molecules are oriented perpendicular to the cover glass, so that the reflected wavefront has the minimum phase delay, defined by n_o.

by two refractive indices: the ordinary (n_o) and the extraordinary (n_e) [73]. The phase modulation of reflective SLMs relies on the controlled orientation of liquid crystal molecules, described by a non-linear electro-optical response to voltage. As shown in Figure 2.4, in their unperturbed state, when no voltage is applied, the molecules are aligned parallel to the cover glass (y-axis), such that an incident linearly polarised beam aligned with the extraordinary axis of the liquid crystal experiences the maximum birefringence and, consequently, the maximum phase delay. As voltage is applied to the pixel electrodes, the molecules gradually tilt towards the perpendicular direction (z-axis), reducing the effective refractive index difference between the extraordinary and ordinary axes. This variation in birefringence produces a controllable phase shift on the reflected beam, which depends on the applied voltage, the thickness of the liquid crystal layer, and the wavelength of the incident beam. Thus, if the incident beam is linearly polarised and parallel to the extraordinary axis of the LC molecules (y-axis), the outcome wavefront experiences a phase delay $\Delta\phi$ due to the liquid crystal molecules' orientation with respect to the wave vector $\boldsymbol{k}$ given by:

$$\Delta\phi \ = \frac{2\pi}{\lambda} \ \ OPD = \ \frac{2\pi}{\lambda}\left(n_e(\theta) - n_o\right)2d \tag{2.5}$$

where $n_e(\theta) - n_o$ is the birefringence of the LC material, $\theta = \theta(V)$ is the angle between $\boldsymbol{k}$ and the extraordinary axis identified by the index of refraction n_e, the d is the thickness of the LC layer and λ is the wavelength.

Thus, when illuminated with linearly polarised beam parallel to the extraordinary axes of the LC molecules, the SLM acts as a programmable phase-only modulator based on a fixed spatial pattern, where each pixel is independently addressable to discrete voltage values.

To ensure a predictable and linear response, the manufacturer provides a look-up table (LUT) calibrated at $\lambda = 633$ nm. The LUT defines the mapping between the digital grey level command (0–255, corresponding to 256 8-bit addressing values) and the induced phase delay (0–2π). Thus, each SLM pixel can be addressed with 8-bit digital commands, corresponding to 256 discrete voltage values. As shown in

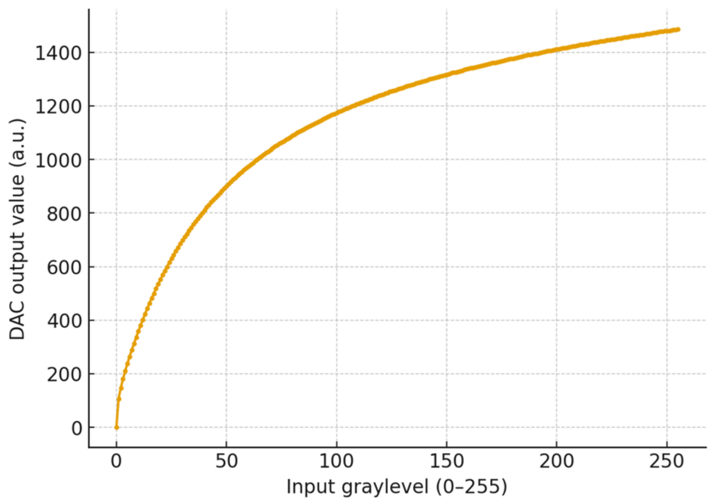

Figure 2.5. SLM's Look-Up-Table calibrated at 633 nm: the mapping defines each 8-bit command, represented as an input grey level (0-255), to a calibrated DAC output value. The latter commands correspond to an induced phase delay (0–2π).

Figure 2.5, the LUT is an operator that maps each digital grey level to a calibrated DAC output value, which in turn sets the voltage applied to the LC layer upon the pixel pad. This voltage controls the birefringence upon the pixel and therefore the induced phase delay, as seen in Eq.(2.5). Through this calibration, the non-linear voltage–phase response is mapped in such a way that input values from 0 to 255 correspond to a linear progression of phase shifts covering the full range 0-2π of the reflected wavefront.

In addition, the manufacturer supplies a Wavefront Correction (WFC) file, which compensates for aberrations introduced by the non-flatness of the silicon backplane. As shown in Figure 2.6, manufacturing tolerances can lead to a slight curvature of the substrate, causing non-uniform thickness of the liquid crystal layer and, consequently,

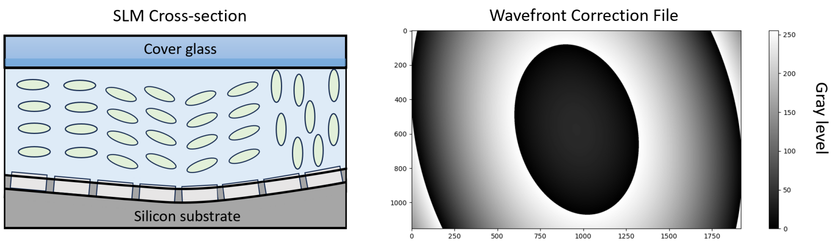

Figure 2.6. Wavefront correction file (WFC) used to compensate for the SLM's intrinsic aberrations due to the manufacturing process, such as the curved silicon back panel. On the left, a schematic representation of the SLM's silicon backplane curvature. On the right, the 8-bit map of the WFC file.

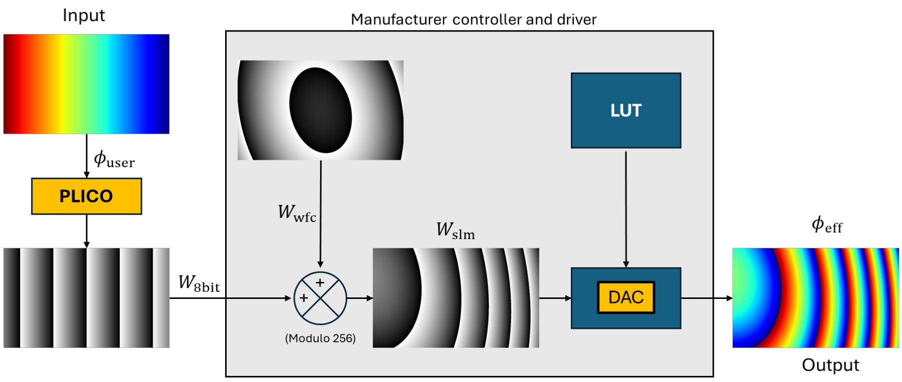

Figure 2.7. SLM control scheme: the user-defined wavefront map is processed by PLICO to compute equivalent 8-bit maps. The latter is processed by the manufacturer control by adding the WFC and using the LUT to produce the output wavefront map. In this example, the case of a Tilt wavefront of a PtV$\sim 3\mu$m defined over the full frame of the SLM is shown, with the calibration wavelength at 633 nm.

spurious phase delay on the SLM reflected beam [74].

From the SDK provided by the manufacturer, we developed a Python package to control the SLM, which has been integrated in PLICO. This control allows to apply commands on the SLM from a user-defined wavefront map in units of meters. Figure 2.7 shows a visual representation of how PLICO interfaces with the manufacturer controller. Particularly, if ϕ_{user} is a given 2D wavefront map, PLICO computes the equivalent 8-bit map $W_{8\mathrm{bit}}$ as follows:

$$W_{8\mathrm{bit}} = \mathrm{round}(\frac{\phi_{\mathrm{user}}}{\lambda_c} L) \mod L\,, \tag{2.6}$$

where $L = 256$ are the SLM phase levels and λ_c is the calibration wavelength and the $W_{8\mathrm{bit}}$ values are in $[0, 1, ..., L-1]$ range. Then, the WFC, W_{wfc}, is superimposed to the user-defined converted wavefront pattern $W_{8\mathrm{bit}}$ by adding the two images with a modulo 256 operation [75]:

$$W_{\mathrm{slm}} = (W_{8\mathrm{bit}} + W_{\mathrm{wfc}}) \mod L\,. \tag{2.7}$$

Finally, the 8-bit image W_{slm} applied on the SLM display is then processed by the wavelength-specific LUT calibration, that corresponds to an effective OPD given by:

$$\phi_{\text{eff}} = \frac{\lambda_c}{L} W_{\text{slm}} \tag{2.8}$$

Recent advancements in Liquid Crystal on Silicon (LCoS) [13] devices have led to the widespread use of reflective phase-only nematic Spatial Light Modulators (SLMs) in AO laboratory applications. The high spatial resolution, with thousands-to-millions of pixels, makes the SLM a promising phase modulator for reproducing atmospheric turbulence on complex pupil geometries, such as those of the E-ELT. Figure 2.8 shows how, by programming the phase pattern at the pixel level, the device is capable of generating atmospheric phase screens across apertures with central obstructions, spiders, and segmented geometries, making them valuable tools for testing and characterisation of upcoming AO facilities for ELTs in laboratory test-beds. To do so, in the pixels region outside the pupil active area (in yellow, on the left panel of the latter figure) is applied a steep Tilt pattern: the result is that, for a huge Tilt, the pixel outside the pupil active area steers the SLM reflected beam outside the FoV of the science camera, basically simulating the effects of the obstructions and spiders in ELTs complex like pupils. On the right panel of the latter figure is shown the generated 8-bit map that simulates the ELT pupil.

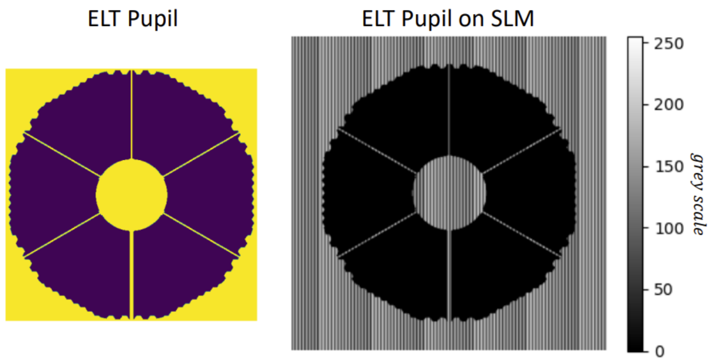

Figure 2.8. ELT pupil reproduced with the SLM. On the left panel, the simulated pupil mask where in yellow and purple are shown the obstruction and active area of the pupil, respectively. On the right panel, an example of 8-bit map command used to reproduce the pupil is shown. The black central area corresponds to the active pupil area, while in the outer region (the yellow one of the left panel) a huge Tilt is loaded. The high resolution of the SLM allows to reproduce any complex pupil shape.

Table 2.3 shows the specification provided by the manufacturer of the present SLM. The SLM offers several advantages compared to conventional deformable mirrors:

- the high spatial resolution of thousands of pixels, allows us to finely reproduce on the SLM turbulent wavefront structures over 8-40 m pupil diameters: for instance, assuming $r_0(500\,nm) = 10$ cm and a circular pupil with a diameter of 1000 pixels, the SLM is capable to reproduce a wavefront with a resolution of 0.8 and 4 cm/pixel for 8- and 40-m pupil diameters, respectively;

- the absence of electro-mechanical actuators and a mechanical surface to reproduce phase distortions eliminates hysteresis, as, in LCoS SLMs, the phase

Table 2.3. 1920×1152 XY Phase Series SLM manufacturer's specifications.

1920×1152 XY Phase Series SLM manufacturer specifications	
Resolution	1920 × 1152
Array size	17.6 × 10.7 mm^2
Fill factor	95.7%
Pixel pitch	9.2 μm
Phase stroke	2π
LC response time	1.8 ms
System frame rate	422.4 Hz
AR coating ($R_{\mathrm{avg}} < 1\%$)	488–800 nm

modulation is driven by the local orientation of liquid crystal molecules under the applied electric field, such that the same voltage always corresponds to the same molecular configuration and phase shift [73];

- the ease of programming allows to reproduce arbitrary pupil obstructions that can be loaded on the SLM directly as digital images, without using complex aperture stop on the testing setup.

However, it also presents inherent limitations:

- the phase modulation works only with monochromatic, polarised light aligned with the liquid crystal extraordinary axis;
- it has a discretised structure, due pixelation (fill factor) and finite quantum phase levels;
- the refresh rate and the optical response (typically ∼500 Hz) is limited and much slower than state-of-the-art deformable mirrors, making the SLM not suitable for real time compensation;
- the complex phase modulation is extremely sensitive to calibration and any deviation from a precise 2π phase wrapping value leads to unwanted spots in the science camera FoV;
- each SLM's pixel can apply a limited phase delay up to 2π (i.e. equivalent to an actuator wavefront stroke of λ) compared to ordinary DMs actuators that typically shows strokes of $\sim 5\mu$m wf: higher delays are reproducible due to the wrapping provided that the phase jump between adjacent pixels is less than 2π:
$$|\Delta\phi| \;=\; |\phi(x+dx, y+dy) - \phi(x,y)| \;\;<\;\; 2\pi\,, \tag{2.9}$$
where dx and dy are the pixel dimensions. If this condition is not met, wrapping artefacts appear in the form of unwanted diffracted spots;
- besides the absence of actuator hysteresis, inter-actuator/pixel coupling may occur when between pixels a huge tension gradient is applied on the scales comparable to the pixel pitch, this is the so-called fringing field effect [73][74].

From the present discussion, it is straightforward to understand that the 1920×1152 Meadowlark XY Phase Series SLM represents a promising phase modulator for laboratory AO experiments relying on its high-resolution wavefront control over complex pupils. However, as will be discussed in the next chapter, the intrinsic nature of SLMs and their complex phase modulation are known to have spurious effects which prevent from a full phase modulation.

Hereafter, to control the SLM we use the calibration provided by the manufacturers and, by means of PLICO, apply any aberration through the corresponding user-defined wavefront maps. Furthermore, we use the SLM itself to reproduce a circular pupil with a radius of $R = 545$px, corresponding to a pupil diameter of $D = 10.028 \pm 0.003$mm. To do so, we applied in the outside region of the active pupil area a Tilt coefficient of $\sim 100\mu$m rms wf over a diameter of 1920 pixels. To note, the uncertainty on D corresponds to SLM sampling quantisation, with a pixel pitch $\Delta = 9.2\mu$m: an uniform half-width $\Delta/2 = 4.6\mu$m implies $\sigma_D = \Delta/\sqrt{12} \approx 3\mu$m.

Chapter 3

SLM-based test-bed characterisation

The experimental validation of wide-field AO reconstruction and control algorithms requires a flexible and controllable test environment, where wavefront aberrations, sensing and compensation must be reproducible under laboratory conditions. As seen in the previous chapter, the SLM results a promising phase modulator for testing MORFEO's control and reconstruction. However, such device, are known to have limitations.

In this chapter, we describe the characterisation performed on the test facility. Particularly, in Sec.3.1 we provide an in depth analysis of the SLM aimed to characterise and detect its limitations, and maximise its phase modulation response. In Sec.3.1, we quantify the response of the SHWFS and its noise propagation on the reconstructed modes. Finally, Sec.3.3 provides a description of the system's aberration and stability.

The present analysis establishes a solid experimental reference, needed for the testing control strategies and closed-loop simulations, and the hardware-in-the-loop control optimisation.

3.1 SLM characterisation

As seen in the previous chapter, the SLM results in a promising phase modulator for testing MOREFO's control and reconstruction. However, despite their high spatial resolution, the intrinsic pixelated structure and complex phase modulation of SLMs present limitations compared to conventional DMs. Such devices are known to have a limited phase depth up to 2π and to produce spurious effects which prevent from a full phase modulation. In the present discussion, we describe the analysis performed to quantify the effects of the SLM intrinsic pixelated structure and its phase quantisation. In addition, we quantified the spurious effects of such a device and the consequence of any deviation from a precise phase wrapping, in the AO simulations. Finally, we show the analysis performed aimed to characterise the SLM time response.

3.1.1 Quantisation effects on phase modulation

The manufacturer provides the SLM with a phase dynamic range of ϕ_{stroke} over L discrete levels, which corresponds to an OPD defined by the specific calibration wavelength λ_{cal} (in our case: $L = 256$, $\phi_{stroke} = 2\pi$, $\lambda_{cal} = 633\ nm$). For a phase modulator with phase stroke ϕ_{stroke} on L discrete levels, the quantisation phase step Δ_q is

$$\Delta_q = \frac{\phi_{stroke}}{L} \tag{3.1}$$

where L are the discrete phase levels. If the per-pixel phase error (namely, if the phase rounding error is uniform over the pixel) due to quantisation is uniform in $[-\Delta_q/2, \Delta_q/2]$ and statistically independent of the pixel, the variance is:

$$\sigma_q^2 = \frac{\Delta_q^2}{12} = \frac{\phi_{stroke}^2}{12\ L^2} \tag{3.2}$$

(is the variance of an uniform distribution of amplitude Δ_q).

To note: if the commanded phase is a complex phase map like a turbulent phase, then all the phase values will fall in a different phase level/state and, with respect to the ideal continuous phase values, they will experience a small random rounding. In this case, the error per-pixel can be modelled as uniformly distributed in the range $[-\Delta_q/2, \Delta_q/2]$. Otherwise, if the commanded phase has values equal to the quantum phase state, quantisation does not introduce any error.

For $L = 256$ and a phase stroke $\phi_{stroke} = 2\pi$ the variance is $\sigma_q^2 \sim 5\ 10^{-5}\ rad^2$. the associated wavefront error at 633 nm is $< 1\ nm\ rms\ wf$. The effects of the phase quantisation can be quantified on the SR (using Marechal)

$$SR_q \approx e^{-\sigma_q^2} \tag{3.3}$$

for $L = 256$ and $\phi_{stroke} = 2\pi$, $SR_{8bit} \approx 0.99995$. Thus, the effect of 8-bit phase quantisation ($L = 256$ and $\phi_{stroke} = 2\pi$) on the Strehl is negligible ($\lesssim 0.005\%$) and it is the same for all the calibration wavelengths.

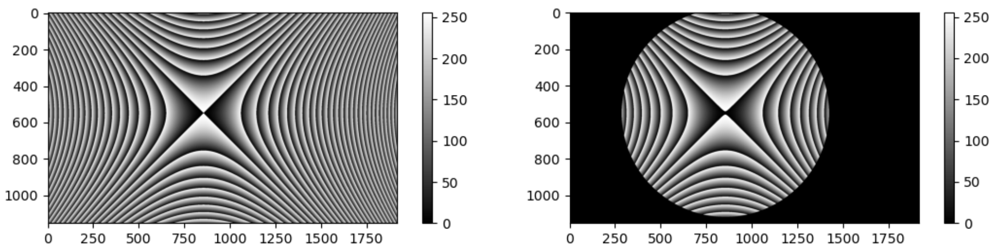

Figure 3.1. Phase pattern of the astigmatism $Z_6 = \sqrt{6}\rho^2 cos(2\theta)$ with amplitude $c_6 = 2\mu m$ rms reproduced with Blink (on left) and PLICO (on the right), without the superposition of the WFC. The Astigmatism is defined in a circular pupil with a radius R of 596 pixels and centred in (853, 550) pixel in a frame that represents the SLM display.

While developing the Python package to control and interface with the SLM, we find out some differences between manufacturer's provided BlinkOverDrivePlus software [75] (hereafter referred as Blink), and the PLICO integrated one, in applying

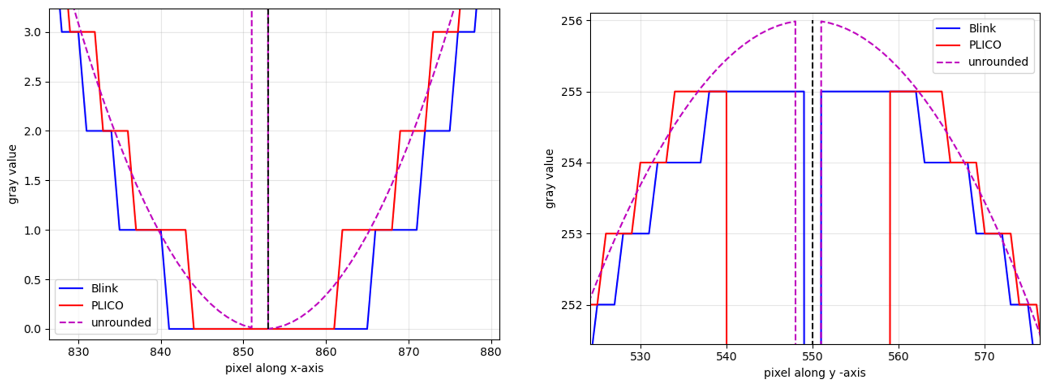

Figure 3.2. Phase pattern profile of the astigmatism $Z_6 = \sqrt{6}\rho^2 cos(2\theta)$ with amplitude $c_6 = 2\mu m$ rms, around the centre of the circular pupil of (853, 550) pixel coordinates. The lines represent the phase pattern value assumed in each pixel. In magenta is shown the value of the phase pattern before the conversion into 8-bit integer value, while in blue and red are shown respectively the 8-bit integer phase pattern obtained with Blink and PLICO. Finally, the black dashed line represents the centre coordinates of the circular pupil. We get a better approximation of the expected phase pattern through our software.

phase patterns on the SLM. We find that Blink and PLICO do not give the same result for equivalent modes. We study the example of Zernike polynomials. For instance, in Figure 3.1 and Figure 3.2, we show the comparison of the phase patterns for the same astigmatism Z_6, with an amplitude $c_6 = 2\mu m$ rms. In both cases, there is no superposition of the WFC. Figure 3.2 shows that these phase patterns are slightly different inside the pupil. The phase pattern applied on the SLM is a result of a modulo 256 operation, whose profile is represented in magenta, which is then converted into 8-bit integers. The difference arises in the conversion to the 8-bit integer. While Blink (in blue) uses a floor division operation, PLICO (in red) uses a true rounding operation. As a result, our software gives us a better approximation of the expected phase pattern.

To conclude, the manufacturer implements a quantisation by truncation (floor division), whereas in our software a rounding-to-nearest convention has been adopted. In the first case, the mean error per pixel is $\Delta_q/2$, which corresponds to a global piston (a constant phase shift across the entire pupil and therefore does not reduce the Strehl Ratio). In the second case, the mean error is zero. However, in both cases the variance of the quantisation error is identical, equal to σ_q^2 and it is negligible in terms of SR loss as previously seen.

3.1.2 Pixelation effects compared to ordinary deformable mirrors

In this section, we describe the effects of the pixelated structure of the SLM compared to ordinary DMs. The pixelated structure and the reflective pixel pads of the SLM behaves as a classical diffraction grating with $N \times N$ grooves. The diffraction grating equation (is the same for reflective and transmissive grating, just sign of the order changes) [76] is given by:

$$m\ \lambda = d\ \sin\theta_m \qquad m \in \mathbb{Z} \tag{3.4}$$

where d is the pitch, θ_m is the reflected angle of the diffractive order m, and λ is the wavelength. Thus, if the reflected collimated beam is focused by an objective lens with focal length f, the position of the diffraction order x_m is given by:

$$x_m \approx f \ \sin\theta_m \ = m \ \frac{\lambda \ f}{d} \tag{3.5}$$

This relation tells where the main diffractive order occurs in the focal plane (for the classical grating is where constructive interference occurs). In our case, for $\lambda = 633$nm, $f = 250$mm, and $d = 9.2\mu$m, these spots doesn't affect our available field of view and the diffraction spots will occur at multiples of ~ 1.7 cm, while our science camera is 4.76×6.23 mm. We want to compute the effects of the fill factor on the PSF. Following [76], we compute the scalar electric field on the focal plane in far field approximation:

$$U(x,y) \ = \ \frac{e^{jkf}}{jkz} \ e^{j\frac{k}{2f}(x^2+y^2)} \iint_{-\infty}^{\infty} U_r(\xi,\eta) \ e^{-j\frac{k}{f}(x\xi+y\eta)} d\xi d\eta \tag{3.6}$$

where f is the focal length of the objective lens, k is the wave number $k = 2\pi/\lambda$, and $U_r(\xi,\eta)$ is the reflected field on the pupil plane. The PSF is the modulus squared of the Fourier transform of U

$$I(x,y) \ = \ |U|^2 \ \simeq \ |\mathcal{F}\{U_r\}|^2 \tag{3.7}$$

where x and y position coordinates in the focal plane are related to spatial frequencies in the Fourier domain $\nu_x = \frac{x}{\lambda f}$ and $\nu_y = \frac{y}{\lambda f}$

If we consider a 1D model, electric field on the pupil plane that is reflected from the SLM pixelated structure with N pixel, size a and pitch d is given by:

$$U_r(\xi) = \sum_{n=0}^{N-1} rect(\frac{\xi \ - \ (n+1/2) \ d}{a}) \tag{3.8}$$

Thus, the intensity is given by:

$$I_{1D}(x) = (\frac{aN}{\lambda f})^2 \ \frac{sinc^2(N \ \frac{xd}{\lambda f})}{sinc^2(\frac{xd}{\lambda f})} \ sinc^2(\frac{xa}{\lambda f}) \tag{3.9}$$

extending to a 2D dimension:

$$I_{2D}(x,y) = I_{1D}(x) \ I_{1D}(y) \tag{3.10}$$

The intensity peak ratio between the one given by the pixelated structure of the SLM with respect to continuous mirror of same aperture size is:

$$\frac{I_{2D}(0,0)}{I_c(0,0)} = (\frac{aN}{\lambda f})^4/(\frac{D}{\lambda f})^4 = (\frac{a^2}{d^2})^2 \tag{3.11}$$

thus the ratio increases quadratically with the active area of the pixelated structure. is proportional to the square of the fill factor, for the present SLM (see Table2.3) the loss is $\simeq 8.4\%$.

These energetic considerations are still valid if we assume a bidimensional grating with a circular aperture of radius R. Thus, the pixels at the edge of the pupil are cut: the fraction of pixels at the edge is the ratio between the perimeter and the area $2\pi R/(\pi R^2)$. For $R = 545$ pixels, $2/R = 0.37\%$. Thus, the committed error on the effective active area (considering a circular pupil instead of a square one) is negligible on the intensity peak loss. So, the on-axis intensity loss does not depend on the pupil shape but only on the fraction of active area. Therefore, the on-axis intensity peak loss does not depend on the shape of the aperture/pupil, but only on the fraction of active area, provided that the illumination is uniform and the phase is flat.

3.1.3 Unmodulable zero-order spot

Phase only SLMs reflected beams are usually polluted by a non-negligible fraction of light which prevents a full phase modulation. The result is an un-modulated spot in the specular reflection of the SLM, often referred to as a zero-order spot. As shown in Figure 3.3, this affects the available field of view on the science camera, setting constraints in reproducing short exposure seeing-limited PSFs in AO simulations.

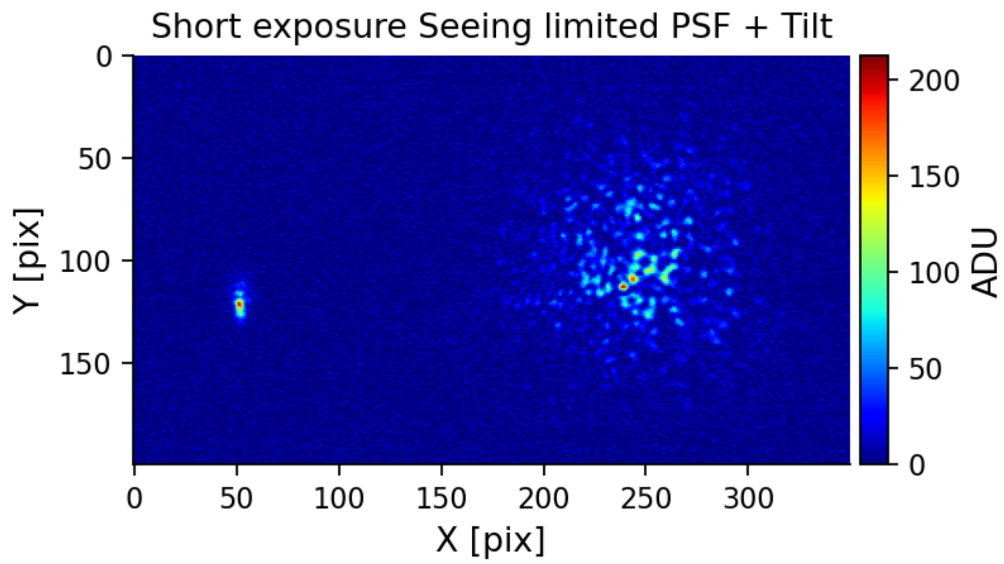

Figure 3.3. Unmodulated zero-order spot polluting the available FoV. The magnitude of the zero-order spot (on the left) is comparable to the seeing-limited speckles of the short exposure PSF (on the right).

Several factors can contribute to the magnitude of this spot, as reported and documented in many studies [77, 78, 79, 80, 81, 82]. Among these, cross-polarised leakage due polarisation misalignment produces a coherent and unmodulated zero-order spot. As seen in Sec.2.4.3, the LCs modulate only one linear component of the incoming electric field, the one aligned to the LC's director axis, defined by the extraordinary refractive index n_e. Thus, any angular deviation between incident polarisation and the SLM modulation axis, generates on the reflected beam a cross-polarised component on the orthogonal direction of the LC director, leading a fraction of power in the specular reflection. Furthermore, the intrinsic nature of SLM is responsible for residual power on the specular reflection. Its complex modulation is the cause of a partial depolarisation on the reflected beam. It consists of a reduction of the output degree of polarisation caused by spatial and temporal inhomogeneities, whose physical origins are well understood [78, 79, 81]. As a result, the SLM maps the input field into a randomly distributed polarisation state so that the camera exposure integrates these states, lowering the degree of polarisation of the reflected beam. Thus, the depolarised component adds incoherently to the phase-modulated field, leading to a residual zero-order spot that does not vanish with the polariser rotation and can be just partially suppressed by an analyser (i.e. an additional linear polariser located to analyse the polarisation state of the SLM reflected beam).

On the other side, the reflective pixel pad has a finite fill factor that acts like an amplitude grating, given by the gap between pixels that reflects the beam without applying any phase modulations. Only the recent SLM series have a dielectric mirror placed over the pixel reflective pad allowing a full phase modulation and avoiding this effect. To quantify the effect of the amplitude grating effect caused by the inter-pixel gap, we assume a Fraunhofer regime and a scalar model for the electric field (following [76]), to compute the expected magnitude of the spot in the specular reflection and analyse its behaviour as a function of the commanded phase. We consider a pupil plane P of area A_{tot} and define the active area function $M(\xi, \eta) \in \{0, 1\}$ where $M = 1$ on the active pixels and $M = 0$ on the gaps between pixels. Thus, for the considered geometry, the active area A_{act} is given by the integral of the pixel function over the pupil domain $A_{act} = \iint_P M \; d\xi d\eta$, while the one relative to the gap is $A_{gap} = A_{tot} - A_{act}$, and the fill factor is $\mathrm{ff} = A_{act}/A_{tot}$. So the reflected complex field on the SLM (the pupil plane P) can be written as:

$$U_r(\xi, \eta) = R_{act}\; M(\xi, \eta)\; e^{j\phi(\xi,\eta)} \;+\; R_{gap}\; (1 - M(\xi, \eta)) \tag{3.12}$$

where R_{act} and R_{gap} are the mean complex amplitudes of the reflected field by the active and inter-pixel areas respectively, and $\phi(\xi, \eta)$ is the commanded phase over the active pixel area (which determinates a phase-only modulation on the active area, so that $|e^{j\phi(\xi,\eta)}| = 1$).

The on-axis field, namely $(x, y) = (0, 0)$ for which the kernel is equal 1, Eq.(3.6) using Eq.(3.12) becomes (for simplicity, we neglect propagation constants in Eq.(3.6)):

$$\begin{aligned} U(0,0) &= R_{gap}\, A_{gap} + R_{act} \iint_{A_{act}} e^{j\phi(\xi,\eta)}\, d\xi\, d\eta = \\ &= A_{tot} \left[R_{gap}\, (1 - \mathrm{ff}) + R_{act}\, \mathrm{ff}\; \langle e^{j\phi} \rangle \right] \end{aligned} \tag{3.13}$$

where we define the mean complex field (mean of the phasor $e^{j\phi(\xi,\eta)}$) over the active area as follows:

$$< e^{j\phi} > = \frac{1}{A_{act}} \iint_{A_{act}} e^{j\phi(\xi,\eta)}\; d\xi d\eta \;=\; \frac{1}{A_{act}} \iint_{\mathbb{R}^2} M(\xi, \eta)\; e^{j\phi(\xi,\eta)}\; d\xi d\eta \tag{3.14}$$

Using Eq.(3.7), the on-axis intensity becomes:

$$I(0,0) \ = \ A_{tot}\,|R_{gap}\,(1-\text{ff}) \ + \ R_{act}\ \text{ff} \ \ < e^{j\phi} > |^2 \tag{3.15}$$

The total intensity on the focal plane can be computed relying on Parseval/Plancherel conservation law. So the integral of the intensity on the focal plane can be computed from the one computed on the pupil plane:

$$I_{tot} \ = \ \iint_P \ |U_r(\xi,\eta)|^2 \ d\xi d\eta \tag{3.16}$$

where $|U_r(\xi,\eta)|^2$ can be written as follows:

$$\begin{aligned}
|U_r|^2 &= |\,R_{\text{act}}\,M\,e^{j\phi} \ + \ R_{\text{gap}}\,(1-M)\,\big|^2 = \\
&= \big(R_{\text{act}}\,M\,e^{j\phi} \ + \ R_{\text{gap}}\,(1-M)\big)\big(R^*_{\text{act}}\,M\,e^{-j\phi} \ + \ R^*_{\text{gap}}\,(1-M)\big) = \\
&= |R_{\text{act}}|^2\,M\,|e^{j\phi}|^2 \ + \ |R_{\text{gap}}|^2\,(1-M) \ + \ 2\,\Re\Big\{\,R_{\text{act}}\,R^*_{\text{gap}}\,M(1-M)\,e^{j\phi}\Big\}\,.
\end{aligned} \tag{3.17}$$

To note that the SLM acts as a phase only modulator (so $|e^{j\phi}|^2 = 1$) and the active and the inter-pixel regions do not overlap (thus, the cross term $M(1-M)$ is 0 for each point in the pupil plane). Thus Eq.(3.16) becomes:

$$I_{tot} = |R_{\text{gap}}|^2\,A_{\text{gap}} + |R_{\text{act}}|^2\,A_{\text{act}} = A_{tot}\Big[(1-\text{ff})\,|R_{\text{gap}}|^2 + \text{ff}\,|R_{\text{act}}|^2\Big] \tag{3.18}$$

Finally, using Eq.(3.15) and Eq.(3.18), the fraction of intensity in the specular reflection is defined as:

$$\eta_{00} = \frac{I(0,0)}{I_{tot}} = \frac{\Big|\,R_{\text{gap}}(1-\text{ff}) + R_{\text{act}}\,\text{ff} \ < e^{j\phi} > \,\Big|^2}{(1-\text{ff})\,|R_{\text{gap}}|^2 + \text{ff}\,|R_{\text{act}}|^2} \tag{3.19}$$

The inferred expression for η_{00} shows explicitly the dependence of the zero-order spot magnitude from the reflectance of the active and inter-pixels areas, the pixel fill factor and the commanded phase on the SLM.

If the inter-pixel gap is filled with an absorptive mask (i.e., $|R_{gap}| = 0$ and $|R_{act}| = 1$), only the active area concur to the phase modulation, so $\eta_{00} = \text{ff}\ |< e^{j\phi} > |^2$. If between the reflective pixel pad and the LCs is placed a dielectric mirror (i.e., $|R_{gap}| = |R_{act}| = 1$ and $\text{ff} \to 1$), the phase is applied over the full pupil P and even the inter-pixel gap is phase modulated, so $\eta_{00} \ \approx \ |< e^{j\phi} > |^2$. However, if there is no dielectric mirror and the gap is reflective, the inter-pixel area doesn't contribute to the phase modulation and the phase is applied only in the active area. If we assume that the active and inter-pixel area have the same reflectance (we expect typically $|R_{gap}| \lesssim |R_{act}|$) the efficiency in the specular reflection is given by:

$$\eta_{00} \ = \ |(1-\text{ff}) + \text{ff} < e^{j\phi} > |^2 \tag{3.20}$$

If the SLM command is a constant phase $\phi = \phi_0$, $< e^{j\phi} >= e^{j\phi_0}$, thus $\eta_{00} = 1$ as expected (we have the maximum efficiency on the zero-order). If the commanded phase is almost constant across the active area, the complex mean of the phasor has a modulus close to unity; otherwise, for high or uncorrelated phase variation across the pupil, $|\langle e^{j\phi}\rangle| << 1$ (for further details see Appendix B).

This analysis allowed us to define an upper bound to the residual power on the zero-order caused by the SLM pixelated structure. For the present SLM with a ff $= 95.7\%$ (see Table 2.3) if we consider a reflecting and non-modulated gap, the pixelated structure contribution to the zero-order is $< 0.2\%$. Thus, in the following analysis this effect is neglected.

To quantify the fraction of the phase that is effectively modulated by the SLM compared to the residual un-modulated one, we measure how the power is distributed between two spatially separated spots in the focal plane while rotating a linear polariser (LP) with respect to the SLM's LC director axis (i.e. the extraordinary axis). To do so, a Tilt command is applied on the SLM, causing a PSF shift in the focal plane. As shown in Figure 3.4, it spatially separates the phase modulated component of the reflected beam into a first diffraction order (the "Tilt-order"), from the modulation-free component that lies in the specular reflection and is responsible for residual power on the zero-order.

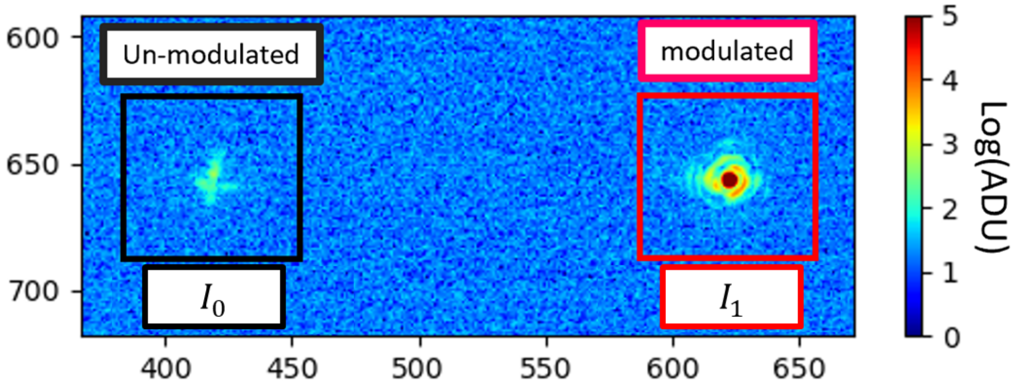

Figure 3.4. Regions of interest after the application of a Tilt on the SLM. The residual fraction of the reflected beam that lies in the zero-order corresponds to the non-modulated spot (I_0), while most of the light is tilted (I_1).

To compute the associated power, we defined two square regions of interest (ROIs) of 50×50 pixels, one centred on the zero-order and one on the Tilt-order. For each rotation of the LP angle θ, we acquire a frame, subtract a background image and the camera bias, and compute the integrated intensities $I_0(\theta)$ and $I_1(\theta)$ as the sum of the pixel values inside the corresponding ROIs.

To suppress any drifts and jitter effects due to the laser source and any normalization bias introduced by using a separate reference frame acquired at a different time, we normalize the integrated intensities by the total intensity in the two ROIs, $I_{tot}(\theta) = I_0(\theta) + I_1(\theta)$, and compute the corresponding efficiencies $\eta_0(\theta)$ and $\eta_1(\theta)$ of the zero- and Tilt-order, respectively:

$$\eta_0(\theta) = \frac{I_0(\theta)}{I_{tot}}, \qquad \eta_1(\theta) = \frac{I_1(\theta)}{I_{tot}}.$$

Physically, the rotation of the LP relative to the LC extraordinary axis results in a Malus-like response. Particularly, the modulable order follows $\sim cos^2(\theta)$ while the zero-order follows $\sim sin^2(\theta)$, up to offsets that capture depolarisation, coherent cross-polarised leakage and any other non-idealities.

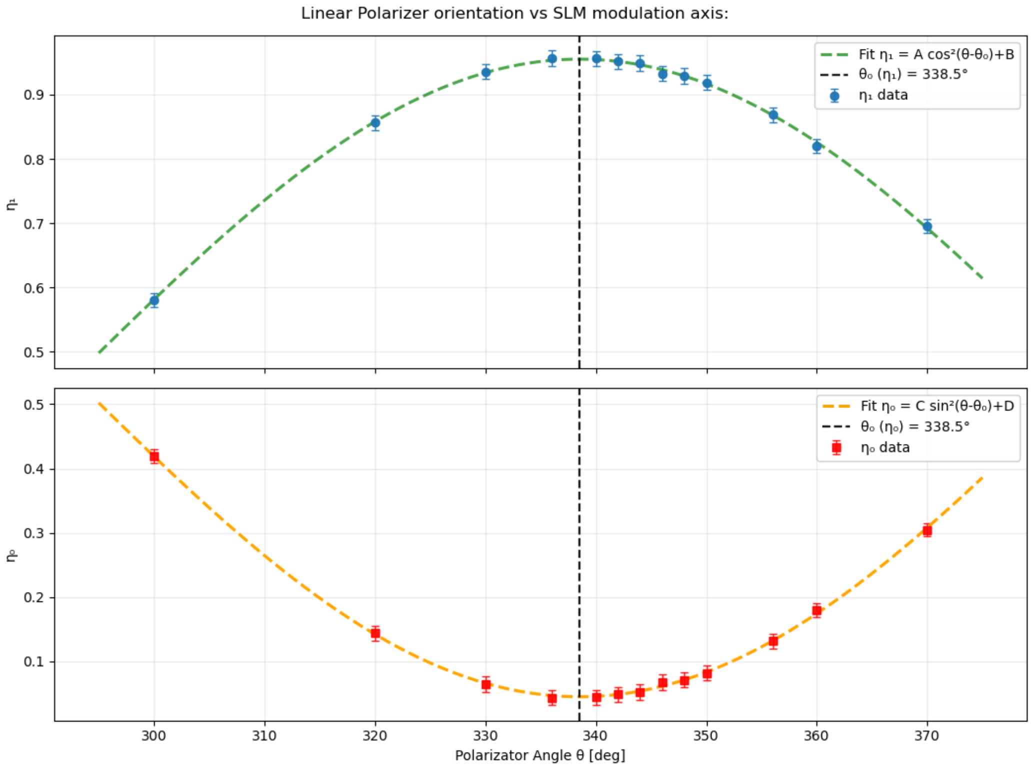

Figure 3.5. Intensity ratios as a function of the rotation angle of the linear polariser support. The intensity ratios measured in the zero-order, η_0 , and tilted region, η_1, are shown in blue and red dots, respectively. The dashed lines represent the fitted curve of the Malus-like modes for η_0 and η_1 in orange and green, respectively. Finally, the black dashed lines correspond to the estimated optimal angle θ_0.

Figure 3.5 shows the measured efficiencies in the zero and Tilt orders for the LP rotation angles and the corresponding fits, computed with the Malus-like model as follows:

$$\begin{aligned} \eta_1(\theta) &= A\cos(\theta-\theta_0)^2 + B, \\ \eta_0(\theta) &= C\sin(\theta-\theta_0)^2 + D \end{aligned} \tag{3.21}$$

where θ_0 is the LP angle aligned with the SLM modulation axis (defined modulo 180°); A and C represent the modulable components in the Tilt and zero-order, respectively, D is the un-modulable residual in the zero-order that cannot be erased by the LP alignment, and B is an offset around zero (due to the background subtraction and the absence of unmodulable component in this ROI). Since θ_0 has a periodicity of 180°, after fitting, we project θ_0 mod 180 ° into the actual LP rotation angle range (300°-370°) to report a physically meaningful orientation within the interval used for data acquisition. Thus, the outcome analysis reported in Table 3.1 shows that

Parameter	η_1	η_0
A, C	0.96 ± 0.03	0.96 ± 0.03
B, D	-0.01 ± 0.03	0.045 ± 0.004
θ_0	$(338.5 \pm 0.4)^\circ$	$(338.5 \pm 0.4)^\circ$

Table 3.1. Estimated fit parameters for η_1 and η_0.

the $\sim 95 - 96\%$ of the optical power reflected by the SLM can be actively (phase) modulated at the optimal LP rotation angle $\theta_0 = (338.5 \pm 0.4)^\circ$, while we measure a non-negligible incoherent residual power in the zero-order $(4.5 \pm 0.4)\%$ that remains un-modulated, which prevents a full phase modulation. For the following analysis, we set the LP angle at $\theta_0 = 338.5^\circ$ to maximise the SLM phase modulation response.

To complement the polarisation-angle dataset study, we analyse how the residual power in the zero-order evolves as a function of the applied command. The aim is to verify that the residual incoherent component on the zero-order does not depend on the commanded phase. To do so, using a similar procedure as previously described, we measured the efficiencies, η_0 and η_1, in the zero- and Tilt-order as a function of the RMS amplitude (c_2) of the commanded Tilt. However, we want to stress that this is just a qualitative cross-check of the measured efficiencies under Tilt modulation.

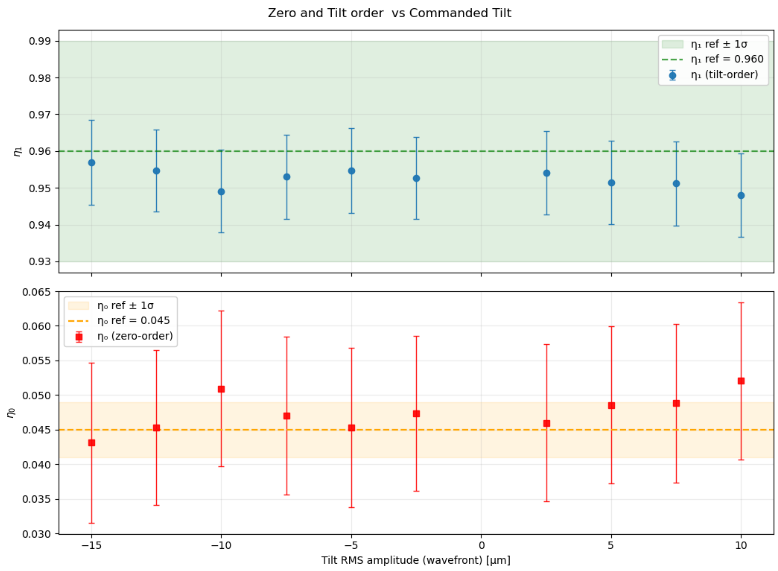

Figure 3.6. Intensity ratios η_0 (red dots) and η_1 (blue dots) for the zero and Tilt order, respectively, as a function of RMS the amplitude of the applied Tilt. The dashed green and red lines are the estimated parameters A and D, respectively, in Table3.1, while the bands are the associated $\pm 1\sigma$ interval. The intensity ratios are constant in the explored range of applied Tilt.

Indeed, unlike the polarisation-angle measurement procedure (where each integrated intensity was normalized by its own per-frame total intensity), the measured efficiencies in the zero and Tilt order, shown in Figure 3.6, are computed from frame-averaged ratios normalized to an independently measured reference frame (acquired in a different time t_0 and when the SLM is set to a flat command, $\eta_k = \langle I_k(c_2, t)/I_{flat}(t_0)\rangle_t$). As a result, the dataset does not benefit from the frame-wise suppression of frame-to-frame source fluctuation, which was enforced in the polarisation-angle analysis. For this reason, the analysis is strictly a qualitative cross-check. In the latter figure, we over-plot the horizontal references corresponding to the best-fit parameters from Table 3.1. The measured efficiencies are compatible with the estimated fit parameters within 1σ, but the apparent reduction of the error bars on η_1 and the simultaneous inflation on η_0 relative to the fitted parameters are expected consequence of the different normalization (to a separate reference frame), responsible of an implicit reweighting of $1/I_{flat}$ before averaging, and the absence of frame-wise source systematics cancellation.

3.1.4 Linearity of the PSF displacement to the commanded Tip-Tilt

To quantify the linear response of the SLM to commanded Tip and Tilt wavefronts, we measure the displacement of the PSF centroid on the science camera placed at the focal plane of the lens L_2.

In the paraxial approximation, the PSF shift is a linear function of the wavefront slope commanded by the SLM. Using the Noll notation for Zernike polynomials, Tip Tilt modes , Z_2 and Z_3 respectively are described as:

$$Z_2(\rho, \theta) \ = 2\rho \ cos\theta, \qquad Z_3(\rho, \theta) \ = 2\rho \ sin\theta \tag{3.22}$$

where ρ and θ are the polar coordinates in an orthonormal unitary circular pupil. The corresponding wavefront (OPD) is given by:

$$W(\rho, \theta) \ = \ c_2 \ Z_2(\rho, \theta) \ + \ c_3 \ Z_3(\rho, \theta) \tag{3.23}$$

where c_2, c_3 are the RMS amplitude in meters of the Tip-Tilt OPD. Considering a pure Tip-Tilt along x (namely $c_3 = 0$), and writing $x \ = \ R \ \rho \cos\theta$, with R the pupil radius, the wavefront is given by:

$$W(x) \ = \ c_2 \ \frac{2x}{R} \quad \Rightarrow \quad \frac{\partial W}{\partial x} \ = \frac{2c_2}{R} \ = \frac{4c_2}{D} \tag{3.24}$$

where $D = 2R$ is the pupil diameter. In the paraxial approximation, namely small angles for which the reflected ray angle equals the OPD slope α, the PSF shift at the focal plane is given by:

$$\Delta x \ = \ \tan(\alpha) \ f \ \approx \ \frac{4 \ c_2}{D} \ f \ = \ \frac{PtV(W(x))}{D} \ f \tag{3.25}$$

where $PtV(W)$ is the Peak-to-Valley of the wavefront. Similarly, a pure Tip-Tilt along y axis (namely $c_2 = 0$ in Eq.(3.23)), will cause a PSF displacement $\Delta y \ = \ (4c_3/D) \ f$. Eq.(3.25) shows that the PSF shift is a linear function of the commanded Tip (or Tilt) RMS amplitude. However, if there is any small rotation ψ between the SLM and scientific camera axes caused by alignment errors, the expected displacement is mapped by:

$$\begin{bmatrix} \Delta x \\ \Delta y \end{bmatrix} = \frac{4 f_2}{D} \, R(\psi) \begin{bmatrix} c_2 \\ c_3 \end{bmatrix} = \frac{4 f_2}{D} \begin{bmatrix} \cos\psi & -\sin\psi \\ \sin\psi & \cos\psi \end{bmatrix} \begin{bmatrix} c_2 \\ c_3 \end{bmatrix} \tag{3.26}$$

namely,

$$\begin{aligned}\Delta x &= \frac{4f_2}{D}\left(\cos\psi\, c_2 - \sin\psi\, c_3\right),\\ \Delta y &= \frac{4f_2}{D}\left(\sin\psi\, c_2 + \cos\psi\, c_3\right)\end{aligned} \tag{3.27}$$

where $R(\psi)$ is the rotation matrix.

Thus, we use Eq.(3.26) to quantify the SLM response to the commanded Tip-Tilt on the SLM. To do so, we measured the centroid displacement for different commanded pure Tip and Tilt on the SLM, spanning the available field of view in the scientific camera. The commanded wavefront is generated on a circular pupil of 5.25 *mm* of radius. For each RMS amplitude command, a short exposure of the PSF is acquired and then subtracted from the background. The background frame is computed as the temporal median of N frames with the source turned off and setting the same exposure time as the PSF displacement measurement procedure. The centroid of each acquired PSF is computed on a square ROI (Region-of-Interest) of size $\sim\ 3\ FWHM_{dl}$ centred in the measured PSF peak. Since we are not interested in photometric analysis, the PSF centroid coordinates (x_c, y_c) are computed by a 2D Gaussian fit. Besides an Airy fitting would be the ideal appropriate model, Gaussian is a good approximation in a small ROI centred on the core of the PSF and in the presence of static aberrations, providing unbiased centroids estimation. The effective PSF displacement is then computed as the distance of the measured centroids coordinate (x_c, y_c) for a given command with respect to one estimated when a null command is applied on the SLM (x_0, y_0).

Figure 3.7 shows the measured PSF displacements due to a pure Tilt and Tip wavefronts commanded on the SLM, and the results form the linear fitting analysis. From Eq.(3.27), the adopted linear model is described by the following equations:

$$(Tip\ only) \quad \Rightarrow \quad \begin{aligned}\Delta x &= s_{x,2}\, c_2 + b_{x,2},\\ \Delta y &= s_{y,2}\, c_2 + b_{y,2}\end{aligned} \tag{3.28}$$

$$(Tilt\ only) \quad \Rightarrow \quad \begin{aligned}\Delta x &= s_{x,3}\, c_3 + b_{x,3},\\ \Delta y &= s_{y,3}\, c_3 + b_{y,3}\end{aligned} \tag{3.29}$$

where the slopes coefficients are:

$$\begin{aligned} s_{x,2} &= K\cos\psi, \quad s_{x,3} = -K\sin\psi,\\ s_{y,2} &= K\sin\psi, \quad s_{y,3} = K\cos\psi.\end{aligned} \qquad with \quad K = 4f/D \tag{3.30}$$

The outcome analysis shows that the SLM has a linear response with a $R^2 = 99.87\%$ and a relative error less than 2%. In addition, the estimates of ψ from the Tip and Tilt scan, show that the SLM and science camera plane are rotated by 0.97 ± 0.01deg.

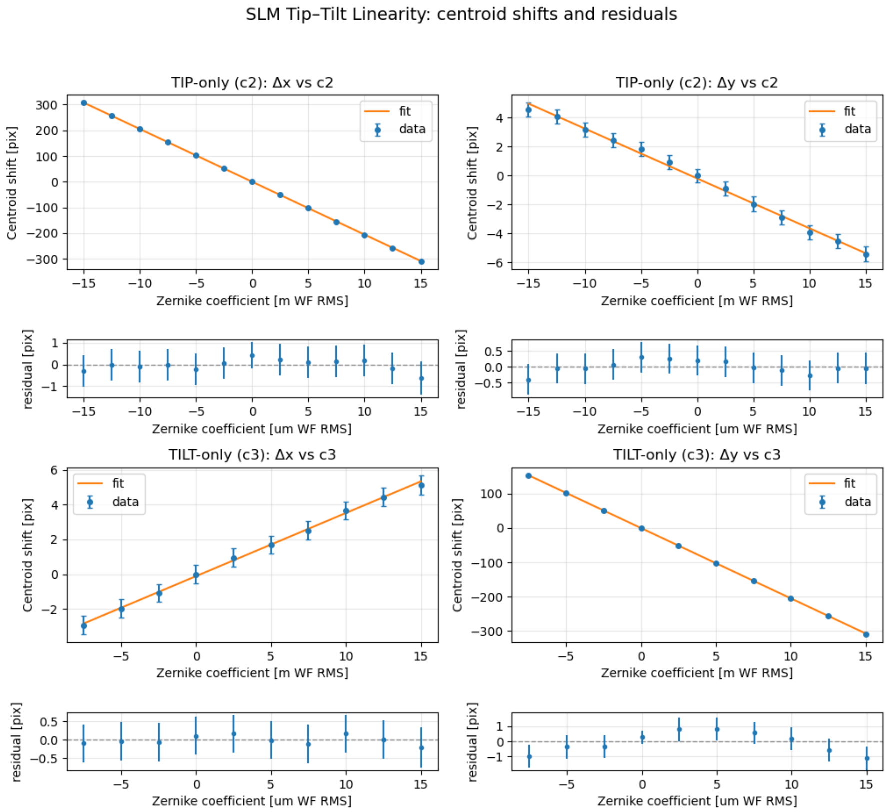

Figure 3.7. PSF centroid shift Δx and Δy along x and y axis, respectively, as a function of the applied Tip (on the top panels) and Tilt (on the bottom panels). The blue dots are the measured centroid shifts, while the orange lines represent the linear fits. For each plot, the residual is shown. The centroid shifts show a linear response, with residual around zero.

3.1.5 Effects of deviation from 2π phase wrapping

The SLM's complex phase modulation creates a wrapped 2π phase pattern from the user-defined wavefront. Any deviation from a linear phase modulation with 2π phase depth coupled with the pixelated structure and the 256 phase quantisation levels of the SLM, results in a degradation of SLM response and loss of diffraction efficiency [80]. These effects lead to diffracted spots on the focal plane, which limit the available field of view and could trick wavefront reconstruction. As discussed in Sec.2.4.3, a user-defined wavefront (or phase) is a result of a λ_{cal} (or 2π) modulo operation. Thus, any commanded wavefront to the SLM results in a wrapped pattern with discontinuity jumps defined by the stroke. Figure 3.8 (left panel) shows

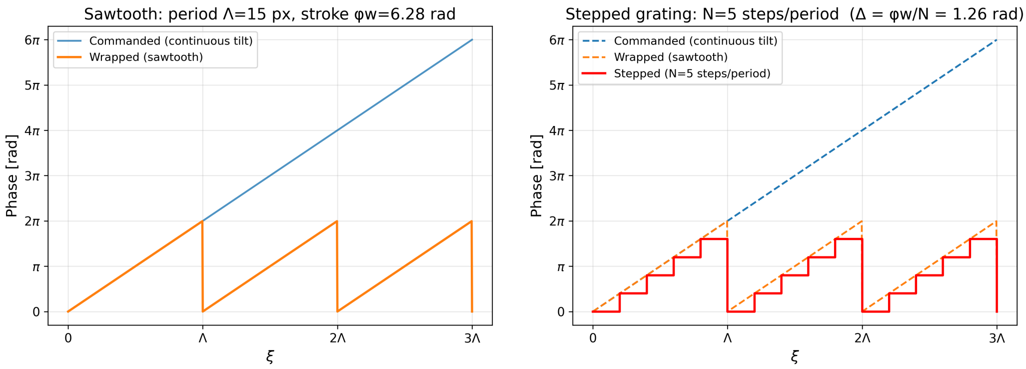

Figure 3.8. A user-defined commanded Tilt (in blue) as sawtooth (in orange, on the left panel) or stepped grating (in red, on the right panel) due the phase wrapping and phase quantisation. The one dimensional phase is shown as a function of the pupil plane coordinate ξ, where Λ is the spatial period of wrapped Tilt. On the right panel, the commanded continuous Tilt and its equivalent sawtooth pattern are shown in blue and orange dashed-lines, respectively.

how a commanded Tilt $\phi(x) = \alpha x$, a continuous linear phase, is applied on the SLM. When $\phi(x) > 2\pi$, the SLM wraps the commanded Tilt on the range $[0,\ 2\pi]$ generating a sawtooth pattern of the same slope, with a spatial period Λ and phase depth 2π. However, if the actual phase depth/stroke ϕ_w is different from 2π, the commanded Tilt will result in a phase grating leading to diffractive spots on the focal plane.

Similarly, Eq.(3.4) can be applied to any kind of grating, so the diffraction grating equation of the sawtooth is described by:

$$m\ \lambda\ =\ \Lambda\ \sin\theta_m \qquad m \in \mathbb{Z} \tag{3.31}$$

where Λ is the spatial period of the sawtooth and m is the diffractive order ($m \in \mathbb{Z}$). Thus, in the paraxial approximation, if the reflected collimated beam is focused by an objective lens with focal length f, the position of the diffraction order x_m is given by:

$$x_m \approx f\ \sin\theta_m\ = m\ \frac{\lambda\ f}{\Lambda}\,. \tag{3.32}$$

However, this relation tells nothing about the intensity distribution across the diffractive orders, only where (destructive or constructive) interference occurs. For the classical grating all the m orders are an exact replica of the on-axis PSF, this is not true when considering sawtooth or stepped gratings, which are designed to favour a specific diffractive order m. To study the effects on the PSF caused by a deviation from a 2π phase stroke, consider a 1D model to describe how a commanded Tilt is applied on the SLM when the actual phase wrapping occurs at ϕ_w:

$$U_r(\xi) \;=\; rect(\frac{\xi - \Lambda/2}{\Lambda})\; e^{j\frac{\phi_w}{\Lambda}\xi} \;*\; comb(\frac{\xi - \Lambda/2}{\Lambda}) \tag{3.33}$$

From Eq.(3.7):

$$I(x) \;=\; (\frac{\Lambda^2}{\lambda f})^2\; sinc^2(\frac{\Lambda x}{\lambda f} \;-\; \frac{\phi_w}{2\pi}) \sum_{q=-\infty}^{+\infty} \delta(\frac{\Lambda x}{\lambda f} - q) \tag{3.34}$$

So in the Fourier domain, the envelope will be sampled at the spatial frequencies defined by the spatial period of the sawtooth $\nu_q = q/\Lambda$. This corresponds to the focal plane positions $x_q = q\,\frac{\lambda}{\Lambda} f$, as expected from Eq.(3.32). Thus, a commanded Tilt on the SLM may lead to equidistant PSF replicas at the positions x_q, that are a multiple of the expected shift on the PSF caused by a Tilt wavefront of slope λ/Λ (even if ϕ_w is not 2π, the slope is the same). These replicas correspond to the main diffraction orders of the equivalent sawtooth diffraction phase pattern, whose intensity is defined by the actual phase stroke ϕ_w. Indeed, the diffraction efficiency η_q of the diffraction order q is given by (I_{tot} is computed relying on the property $\sum_{q=-\infty}^{\infty} sinc^2(q) = 1$):

$$\eta_q \;=\; \frac{I(x_q)}{I_{tot}} \;=\; sinc^2(q - \frac{\phi_w}{2\pi}) \tag{3.35}$$

Figure 3.9 shows how the diffraction efficiency changes as a function of the effective phase wrapping value: if $\phi_w = 2\pi$, the wrapped phase is equivalent to the commanded continuous Tilt, and the overall intensity is efficiently diffracted to the order $q = 1$, reproducing the effects of a pure/continuous Tilt as expected.

If $\phi_w < 2\pi$: the commanded Tilt behaves like a diffraction grating splitting the energy among the 0 and first-order. In general, if ϕ_w is a multiple k of 2π the reflected beam will be diffracted at the order $q = k$. On the other side, if the phase wrap is $2\pi(k-1) < \phi_w < 2\pi k$, the intensity distribution will mainly split between the order $k-1$ and k. However, this gives rise to other diffraction orders with non-negligible intensities (as shown in Figure 3.9 (top), for $\phi_w = \pi$ $\eta_{-1}, \eta_2 \lesssim 5\%$, for $\phi_w = 1.5\pi$, $\eta_0 \lesssim 10\%$, also visible in the bottom panel of the latter figure).

However, due to the finite resolution both in phase and pupil sampling of the SLM, a commanded continuous Tilt will result in a stepped phase grating of N steps over the spatial period Λ. As shown in Figure 3.8 (right), the SLM implements a sample-and-hold pattern made of N constant phase jumps of width Λ/N and phase level $n\,\phi_w/N$, where $n \in [0,\ N-1]$. In this case, assuming an infinite one-dimensional pupil domain, the complex transmitted electric field can be expressed as the transmittance $t(\xi)$ of the single phase-ladder convolved by the Dirac-comb, as follows:

$$U_t(\xi) = \sum_{n=0}^{N-1}\; rect(\frac{\xi \;-\; (n+1/2)\frac{\Lambda}{N}}{\Lambda/N})\; \exp(j\frac{\phi_w}{N}n) \;*\; comb(\frac{\xi - \Lambda/2}{\Lambda}) \tag{3.36}$$

Following Eq.(3.7), the resulting intensity pattern is given by:

$$I(x) = (\frac{\Lambda^2}{\lambda f})^2 \; \frac{sinc^2(\frac{\phi_w}{2\pi} - \frac{\Lambda x}{\lambda f}))}{sinc^2(\frac{1}{N}(\frac{\phi_w}{2\pi} - \frac{\Lambda x}{\lambda f}))} \; sinc^2(\frac{\Lambda x}{N\lambda f}) \sum_{q=-\infty}^{+\infty} \delta(\frac{\Lambda x}{\lambda f} - q) \tag{3.37}$$

As in Eq.(3.35), the diffraction efficiency of a given order q can be retrieved as:

$$\eta_q(N, \phi_w) \; = \; \frac{I(x_q)}{I_{tot}} \; = \; \frac{sinc^2(\frac{\phi_w}{2\pi} - q)}{sinc^2(\frac{1}{N}(\frac{\phi_w}{2\pi} - q))} \; sinc^2(\frac{q}{N}) \tag{3.38}$$

To note, as $N \rightarrow \infty$: Eq.(3.37) and Eq.(3.38) are equivalent to Eq.(3.34) and Eq.(3.35) respectively, thus the infinite (phase) resolution stepped phase grating collapse to a sawtooth phase pattern. Furthermore, when the phase wrapping is a multiple of 2π, $\phi_w = 2\pi k$, $\eta_k = 1$, thus the 100% of the efficiency lies on the $q = k$ order, as seen in Eq.(3.35), reproducing a pure Tilt. However, Eq.(3.38) shows that, differently from that sawtooth case, the diffraction efficiency of a given order is only a function of the phase wrapping/stroke ϕ_w, but also of the number of steps N per period Λ. Particularly, the envelop term due to the step-and-hold aperture ($sinc^2(q/N)$), tells us that the higher orders are suppressed but most importantly that the main order (the one defined by ϕ_w, where the maximum efficiency is expected) will never reach an efficiency of 100%, unless $N \rightarrow \infty$. Thus, the effective number of steps N per period Λ, is crucial to study the diffraction efficiency behaviour. In literature, N is generally assumed as an independent/free parameter defined by the user. For instance, [80] investigated the diffraction efficiency of stepped gratings on high–phase modulation SLMs by systematically varying N (e.g. 2, 4, 8, 16 levels per period) and comparing theoretical predictions with experimental data. In their formulation, N is not explicitly linked to the commanded phase pattern or to the internal LUT resolution of the device. Similarly, [76] provides the theoretical framework to evaluate diffraction from quantized gratings, again assuming N as a given parameter.

In the present work, we extend these models by deriving an explicit relation between N, the commanded Tilt ϕ_{tilt}, the available stroke ϕ_w and the phase resolution L provided by the LUT calibration. The number of effective steps N changes if wrapping occurs on the commanded Tilt. With reference to Figure 3.10, we distinguish two case scenario:

- $\phi_{tilt}^{PtV} < \phi_w$: if the PtV of the commanded phase Tilt ϕ_{tilt}^{PtV} is less than the phase stroke ϕ_w, the Tilt linearly increases along the pupil in the range of $[0,\ \phi_w)$ and is not wrapped by the SLM. Only a fraction of available phase levels are used. Thus the maximum number of steps is constrained by the Tilt and the phase quantisation levels L. Thus, the effective number of steps is then given by the number of quantisation levels actually spanned:

$$\phi_{tilt}^{PtV} < \phi_w \;\Rightarrow\; N = \min\Bigg(L,\; \left[\frac{\phi_{tilt}^{PtV}}{\Delta\phi_{\text{step}}}\right] + 1\Bigg) \tag{3.39}$$

where the $\Delta\phi_{step} = \phi_w / L$ is the phase quantisation step and $[\ \cdot\ ]$ is the floor operator. So if the commanded Tilt is small ($\phi_{tilt}^{PtV} << \phi_w$), only few steps are used for the sampling and hold; then $\phi_{tilt}^{PtV} \simeq \phi_w$ all the phase levels are used to reproduce the commanded Tilt ($N = L$). This expression is exact in an ideal model but it represents an approximation, since calibration errors, pixel cross-talk and device nonlinearities can reduce the number of effectively distinct phase values.

- $\phi_{tilt}^{PtV} \geq \phi_w$: if the PtV of the commanded Tilt exceeds the phase stroke, the commanded Tilt is wrapped in a train of stepped gratings with a spatial period Λ, with a number of pixel per period N_Λ equal to:

$$N_\Lambda = \frac{\phi_w}{\alpha}, \qquad \alpha = \frac{\phi_{tilt}^{PtV}}{D_{px}} \tag{3.40}$$

where α is the phase distortion per pixel and D_{px} is the number of pixels across the pupil. In each period, the SLM can realise at most L discrete phase levels, but the number of pixels per period N_Λ may impose a tighter limitation. The effective number of phase steps per period is then given by:

$$\phi_{tilt}^{PtV} \geq \phi_w \;\Rightarrow\; N = \min(L, N_\Lambda) \tag{3.41}$$

In other words if N_Λ is huge enough (moderate Tilt), all the L phase level can be used ($N = L$); otherwise for short spatial period (steep Tilts), the sampling and hold is performed only in few pixels ($N = N_\Lambda$). This expression is exact in the stepped-grating model, widely used to describe quantized gratings in Fourier optics [76], and directly connects the commanded Tilt to the number of effective steps available.

So, $N = N(\phi_{tilt},\ L,\ \phi_w)$. This formulation allows us to predict how many effective phase steps per period are actually generated on the SLM for a given Tilt command. Figure 3.12 shows that, when $\phi_w = 2\pi$, the loss of efficiency on the order $q = 1$ for increasing Tilt as shown in Figure 3.11, is not scattered on the zero-order, causing residual energy and polluting the available field of view. Only if $\phi_w < 2\pi$, we observe residual power on the zero-order, however if the deviation from 2π is in the order of 10%, the values of η_0 remain less than 3% in all the explored range of applied Tilt (Figure 3.11). Thus, we do not expect side effects in reproducing ELT complex pupil with huge Tilt. Furthermore, considering the presence of the physical aperture stop upon the SLM, the area of the simulated complex pupil is negligible compared to the active pupil area where phase aberrations are displayed. No power will be distributed on the zero-order.

To conclude, similar approaches have been adopted in literature to model the diffraction efficiency of quantized gratings on SLMs. In particular: [80] derived analytical expressions of diffraction efficiency as a function of the number of phase steps N, while [13] provide a general discussion of the electro-optical response of LCoS modulators and their phase wrapping properties; in [83], we described the SLM diffractive model, relaxing the assumptions on the finite resolution, both in the spatial and phase domain. Here we try to extend these models by linking N explicitly to the commanded Tilt amplitude, the SLM LUT resolution and the effective phase stroke. If $\phi_w = 2\pi$, the loss in efficiency on the order $q = 1$ is due to the stepping and not on the SLM pixelation.

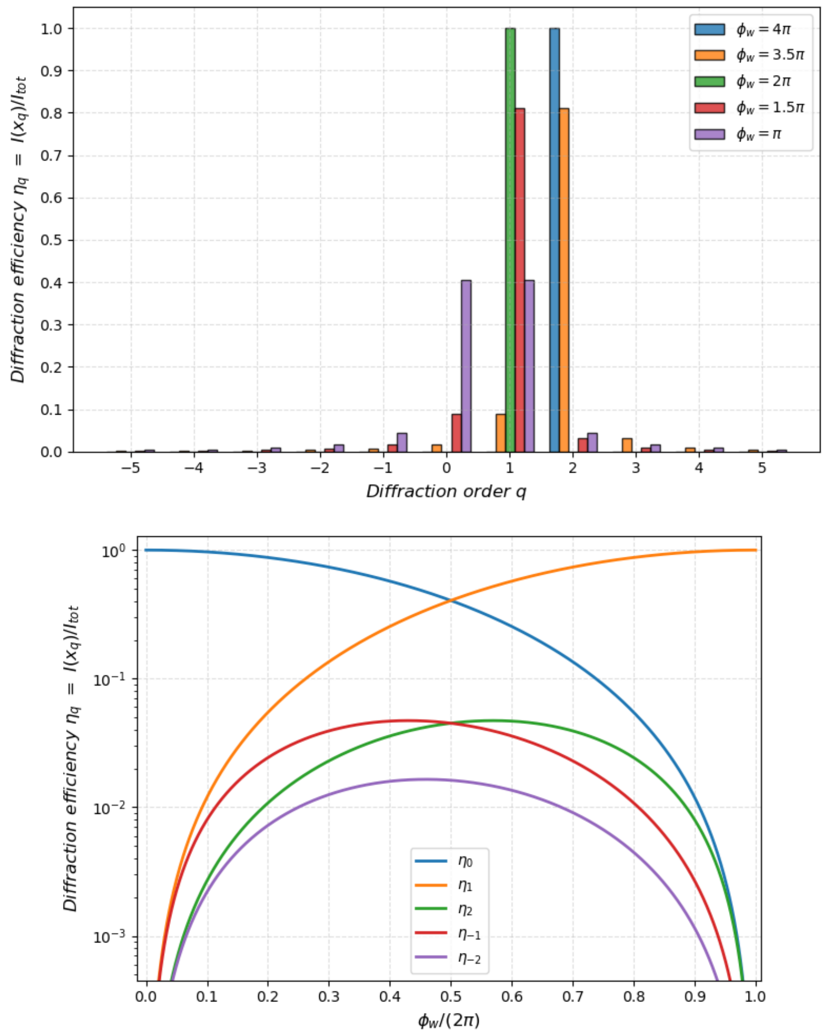

Figure 3.9. Diffraction efficiency as a function of the phase wrapping value ϕ_w. On the top panel, an histogram showing the diffraction efficiencies for diffraction order q for different phase wrapping values. On the bottom panel, are shown the diffraction efficiencies for different orders q as a function of the normalized phase wrapping values. As $\phi_w \neq 2\pi$ the intensity is spread among the diffractive order.

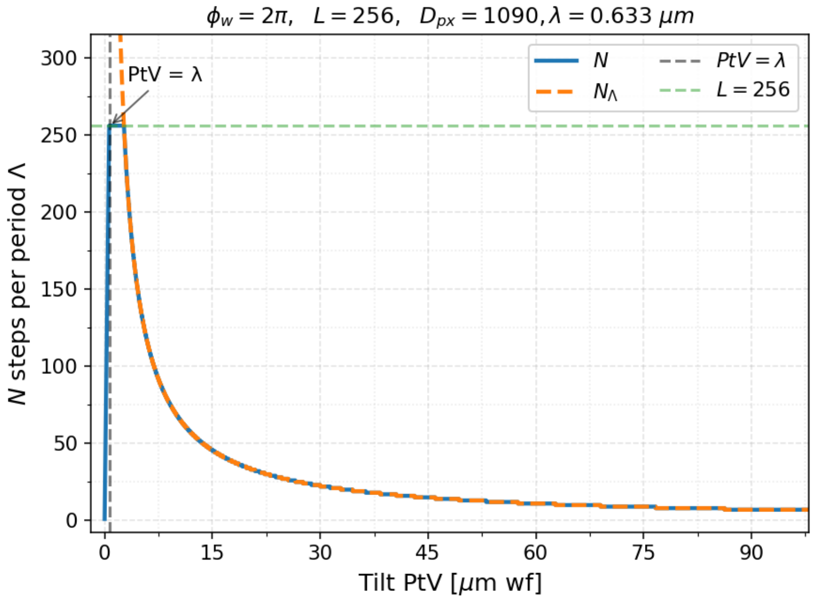

Figure 3.10. N steps per period Λ as a function of the applied Tilt. The blue line is the number of steps N, the orange dashed line is the number of spatial period Λ in the pupil of diameter D_{px}, the grey dashed line corresponds to a PtV equal to λ, and the green dashed line shows when N equals the number of discrete phase levels L. To Note that for PtV$< \lambda$,$N_\Lambda \rightarrow D_{px}$.

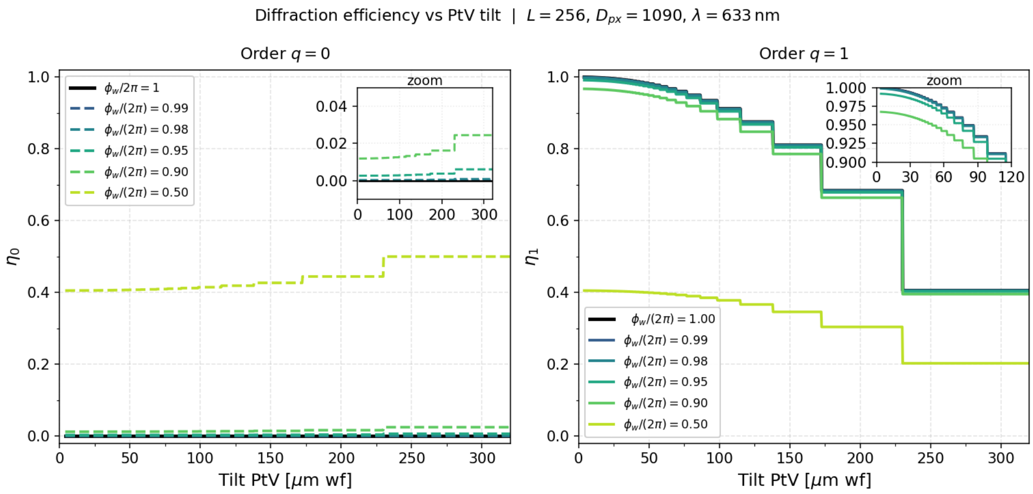

Figure 3.11. Diffraction efficiencies of the zero ($q = 0$, on the left panel), and Tilt order ($q = 1$, on the right panel) as a function of the applied Tilt PtV and normalized phase wrapping values ($\phi_w/2\pi$). To note that for $\phi_w = 2\pi$ there is no residual energy in the zero-order, while residuals only occur for wrapping variations that differ from 2π. We remind that, in the ideal case, η_1 decreases as the number of steps is less, namely as the Tilt PtV is higher.

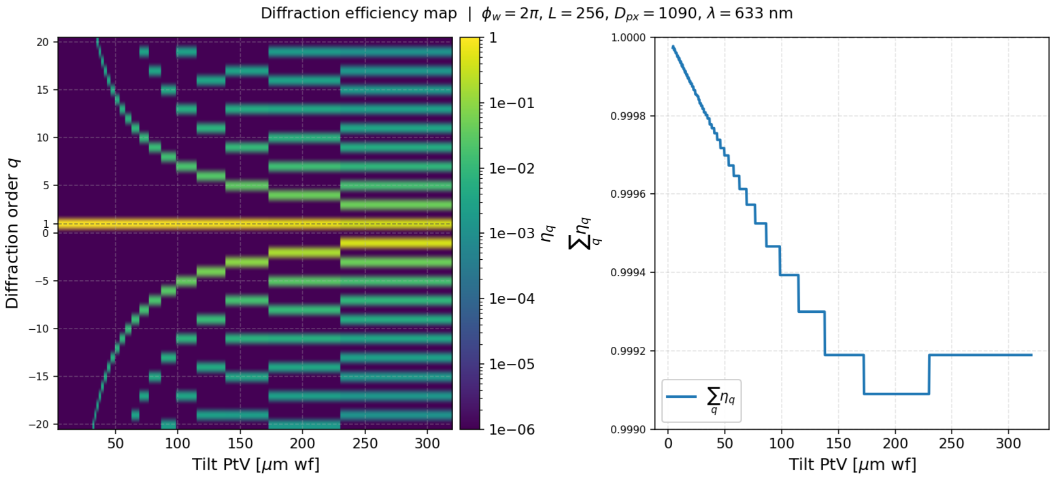

Figure 3.12. Energy distribution on the q diffraction orders. On the left panel, the diffraction efficiencies for the different orders q are shown as a function of the Tilt PtV. On the right panel, the sum of the diffraction efficiencies for a given Tilt is shown as a function of the Tilt PtV. For each Tilt the total normalized energy is close to 1, except for numerical approximations and the selected q orders.

3.1.6 Phase modulation time response

As mentioned in Sec.2.4.3, SLMs are known to have a slower time response and frame rate system compared to the most commonly used DMs in AO applications. Current DMs, such as ALPAO's voice coils [84] and Boston Micro Machines' MEMS [85], demonstrate sub-millisecond mechanical response and kHz frame rates with appropriate drive electronics. In contrast, in LC based phase modulation the dynamics is dominated by the molecular alignment [73]: LC based SLMs typically operate in the millisecond range with rates of a few hundreds Hz [86]. Only the most recent Meadowlark's 1024x1024 SLMs and in-house models [87] show higher frame rates of the order of 1kHz and sub-millisecond time response. According to the manufacturer specifications (in Table 2.3), our SLM is characterised by a LC response time of 1.8 ms, with a system frame rate of 433 Hz.

In this context, we describe the methods and analysis used to quantify the SLM's LC dynamics under applied commands, with emphasis on the step-response (rise, fall and settling time) The derived quantities are then used to optimise the AO loops and synchronize the SHWFS and science camera acquisitions. These time scales sets a lower bound to the needed time between the commanded phase and camera exposure to prevent frame acquisition during the SLM transients (i.e. command settling) in successive loop iterations, reducing outlier frames and optimising the loop timing.

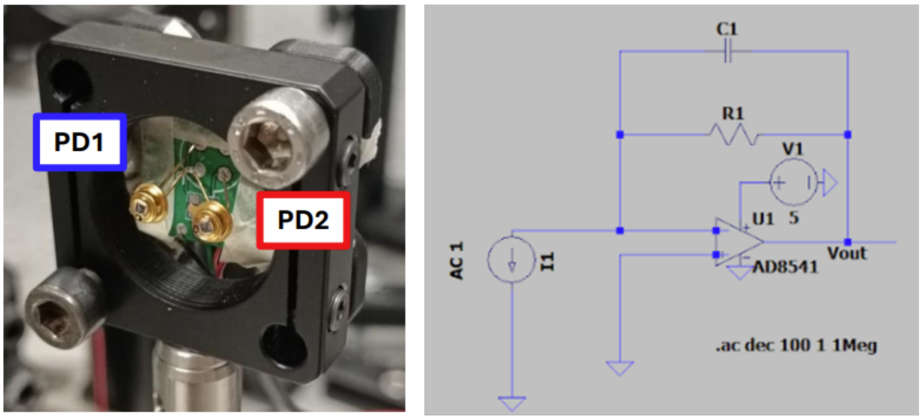

Figure 3.13. Electronic setup used for the SLM time response study. On the left panel, a picture of the 2 photodiodes, PD1 and PD2, placed in the intermediate focal plane, with PD1 on-axis. On the right panel, the electronic scheme of the in-house circuit to sense the SLM reflected beam.

Figure 3.13 shows the setup used for the following analysis. To estimate the LC time response, we built an in-house electronic circuit to sense the SLM reflected beam by means of two photodiodes, hereafter PD1 and PD2. We used the MTD3910PM units manufactured by Marktech Optoelectronics, which were placed in the intermediate focal plane (in place of the Field Stop in Figure 2.2) in order to steer and focus the beam into them. Particularly, PD1 lies on the on-axis optical path, while PD2 is off-axis by ~ 8 mm. Looking at the right panel of the latter figure, each photodiode is read by a trans-impedance amplifier (TIA) operated in photovoltaic mode (i.e. with the photodiode that is zero-biased), so that the photogenerated current (I_1)

is converted into a voltage (V_{out}) read by an ADC. The photodiode is connected to the inverting input of the operational amplifier, while the non-inverting input is grounded. The output is fed with a feedback RC parallel circuit with a resistor of $R_1 = 4M\Omega$ in parallel to a capacitor of $C_1 = 1\,pF$. The cut-off frequency of the RC filter is $f_c = 1/(2\pi\, R_1\, C_1) \approx 39.8\,\text{kHz}$ with a characteristic time scale $\tau = R_1\, C_1$ of $4\,\mu s$. Thus, the in-house circuit has an electronic response time that is comfortably faster than the millisecond dynamics of the SLM. Finally, the operational amplifier for this circuit is the AD8541 manufactured by Analog Devices Inc., which has low input bias currents [88] and therefore can be used together with a high source impedance sensor like the photodiode.

To estimate the time response to the applied commands, we sequentially apply the flat and Tip-Tilt commands to steer and focus the beam into the photodiodes, setting a dwell time between the commanded sequence. We measure the photodiodes voltage signals over time, with a sampling frequency of $f_s = 40\,\text{kHz}$. To reduce noise on the recorded signals, we re-sample the data with a Simple Moving Average (SMA). We select a window of 8 samples, which provides re-sampled signals at 5kHz, corresponding to a temporal resolution $\Delta t = 0.2$ms. This choice allows us to resolve LC transients of $\sim 2\,\text{ms}$ and to be sampled in about 10 sampling points. Figure 3.14 shows the SMA voltage signals over time of the two photodiodes, due to the sequence of flat and Tip-Tilt commands and a dwell time between the SLM commands of 100 ms.

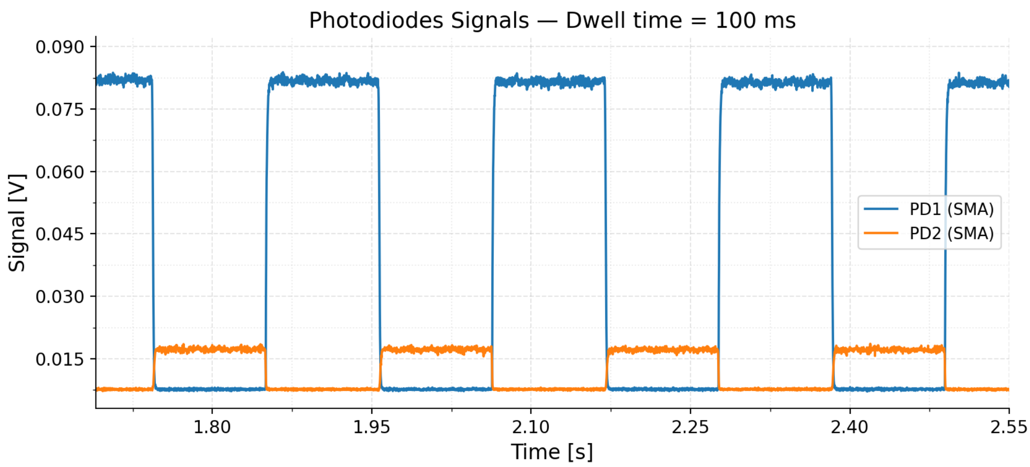

Figure 3.14. Measured photodiodes' voltage signals over time. In blue and orange are shown the SMA signal of the on-axis (PD1) and off-axis (PD2) photodiode, respectively. The lower signal on photodiode PD2 is attributed to the limitations of our in house setup, in which the beam is not properly focused onto the photodiode active area.

For each photodiode, we compute the rise time t_{rise} (and similarly for the fall time t_{fall}) as the period required for the signal to increase from 10% to 90% of its amplitude difference $\Delta V = |V_{max} - V_{min}|$ between the maximum, V_{max}, and minimum, V_{min}, voltage state. The minimum voltage state V_{min} in computed as the median of the signals on a window of 5 ms before the transient, since the signal is already at the minimum regime. While for the maximum voltage state V_{max}, the median is computed on a wider window of 20 ms after the transient, allowing the signal to reach the asymptotic value (reducing any bias due to the exponential-like behaviours) and avoiding the following transient.

To infer the rise and fall time, we compute a linear interpolation between the couple of points at $[k,\, k+1]$ and $[n,\, n+1]$ that bounds respectively the signal corresponding to 10% (V_{10}) and 90% (V_{90}) of the amplitude difference ΔV:

$$\begin{aligned} t_{10} = &\ t_k\ + \frac{V_{10} - V_k}{V_{k+1} + V_k}\,(t_{k+1} - t_k)\,, \\ t_{90} = &\ t_n\ + \frac{V_{90} - V_n}{V_{n+1} + V_n}\,(t_{n+1} - t_n)\,, \end{aligned} \tag{3.42}$$

where

$$\begin{aligned} V_{10} = &\ V_{min}\ + 0.1\,\Delta V\,, \\ V_{90} = &\ V_{min}\ + 0.9\,\Delta V\,. \end{aligned} \tag{3.43}$$

Finally, for each observed transient on the measured signals, we compute the rise and fall time as follows:

$$\begin{aligned} t_{rise} &= t_{90}\ - t_{10} \\ t_{fall} &= t_{10}\ - t_{90} \end{aligned} \tag{3.44}$$

Figure 3.15 shows the observed rising and falling transients on the measured signals on the two photodiodes. However, our measurements (blink control) show $t_{rise} = 1.80 \pm 0.07$ ms and $t_{fall} = 1.54 \pm 0.02$ ms, revealing an asymmetry (probably due geometry, spot not properly centred and focus on the 2 photodiodes) in the rise and fall time and consistency with the manufacturer specifications. Further studies are required to determine whether this asymmetry is related to the SLM or the photodiodes' response or setup geometry.

Finally, we compute the SLM settling time of the SLM command. This is computed as the time difference in an applied command from the t_{90} of the signal fall on one photodiode and the t_{90} of the signal rise in the other one. The outcome analysis shown that the SLM settling time for the commanded Tip/Tilt is 2.74 ± 0.09ms.

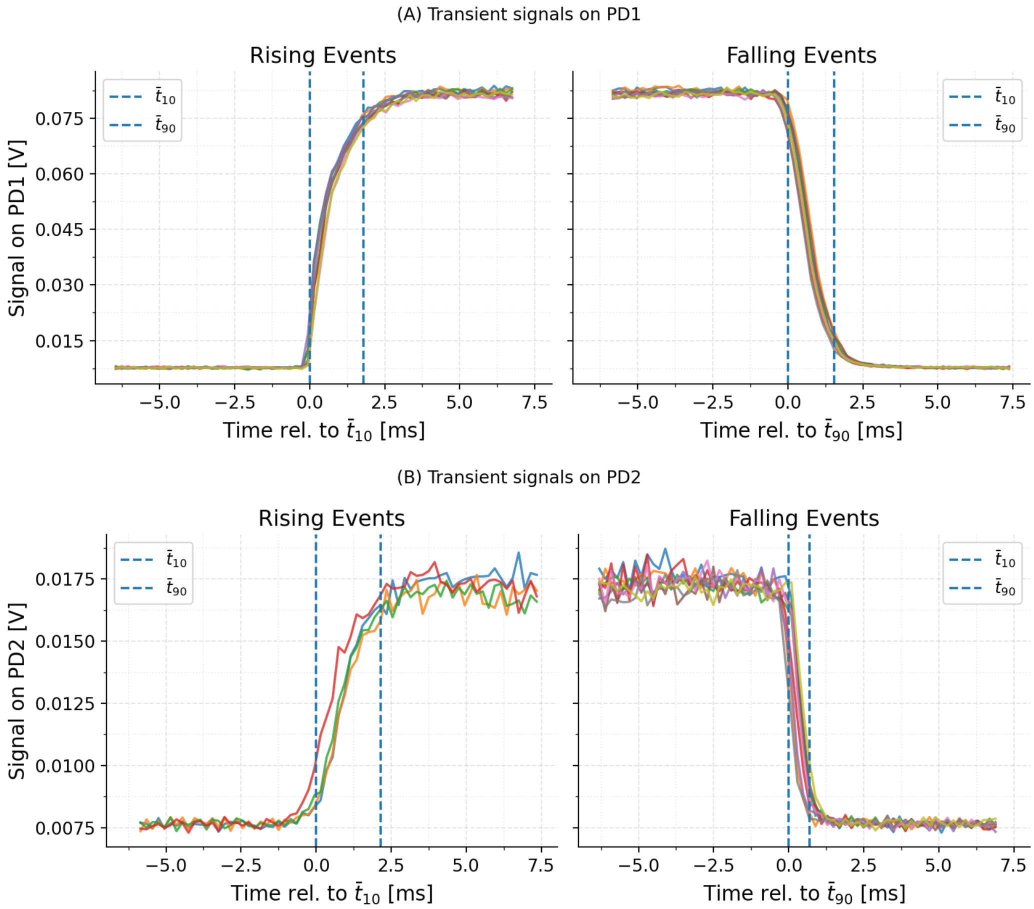

Figure 3.15. Transient events measured on the 2 photodiodes, due to the applied commands. On the top (A) and bottom panels (B), are shown the transients of the rise and fall of the signals measured on the on-axis (PD1) and off-axis (PD2) photodiodes, respectively. The vertical dashed lines are the average values $\bar{t}_{10}$ and $\bar{t}_{90}$, of t_{10} and t_{90}, respectively.

3.2 SHWFS characterisation

In this section, we describe the analysis performed to characterise the performance of the custom SHWFS, by quantifying its dynamic range and noise. Furthermore, we show the methods used to define the actual subaperture set for AO loops simulations and its features.

3.2.1 Subaperture set definition

In present discussion, we described how the SHWFS's subaperture set is defined. To do so, we numerically computed a Cartesian grid centred of 46×46 square ROIs, each of 26 pixel size. Each ROI corresponds to a subaperture that ideally lies on the lenslet barycentres. However, as seen in Sec.2.4.1, the SHWFS pixel pitch and lenslet aperture are responsible of an isotropic radial shift of the spots centroids, rising an apparent Defocus signal (as quantified in Appendix A). In addition, depending on the positioning of the numerical computed square grid with respect to the lenslet centroid, it may rise an apparent Tip-Tilt signal. In order to define a proper numerically computed subaperture set, we use an extended source placed on the intermediate focal plane between L2 and L3 lens, in front of the Field stop FS. The extended source is realised by means of a LED source and a diffuser. This allows to reproduce on the detector, a series of images of the FS aperture, whose barycentres overlap with those of the lenslet array. With reference to Figure 3.16-a, by means of the extended source we define the subaperture grid selecting a central set of subapertures with respect to the footprint, and centring the Cartesian grid with respect to the central image of the FS, in order to minimise the Tip-Tilt error. Once the grid is defined, the extended source is removed, and the subaperture set is applied on the SHWFS image when the SLM is set to the flat command. As visibly shown in the right panel of the latter figure, the generated spots do not overlap on the barycentre of the defined grid, due to the static aberration on the optical system.

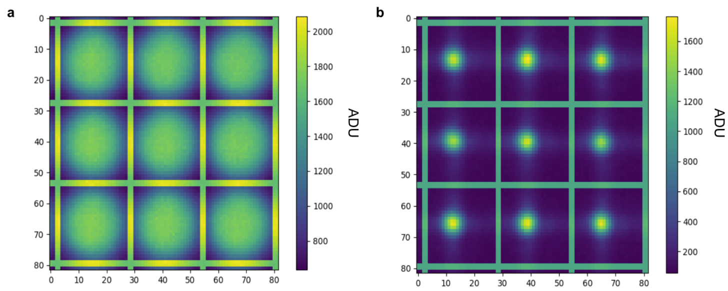

Figure 3.16. Example of frames used to define the subaperture set. On the left panel (a), image of a central (with respect to the beam footprint) ROI of 3×3 subapertures when an extended source is placed on the field stop. The images of the field stop identify the actual barycentre of SHWFS subapertures. On the right panel (b), the same image taken when the extended source is removed. When the SLM is set to the flat command, the generated spot on the subaperture does not lie on the lenslet barycentre. The grid represents the numerically computed subaperture set that is centred on the central subaperture to minimise the Tip-Tilt.

Once the subaperture grid is numerically defined, we select the useful subapertures by looking at the measured flux in each subaperture, in order to detect and remove noisy subapertures from the actual set. To do so, we compute the measured flux in each defined subaperture grid and set a threshold of 1.1 10^4 ADU at an exposure time of 8 ms, to remove badly illuminated lenslet. Figure 3.17, shows the final subaperture set. The final set is made of 1289 subapertures, with 41-42 subapertures along the pupil diameter.

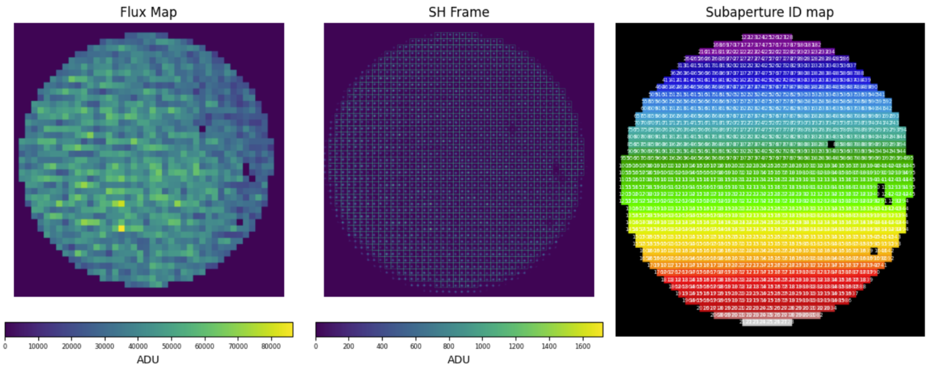

Figure 3.17. Subaperture set maps after flux thresholding. From the left to the right panel, the subapertures' flux map, the corresponding acquired frame and finally a map showing the final adopted subaperture set are shown. The flux seems not uniformly distributed across the subaperture due to the alignment errors. The defined set is made of 1289 subapertures. The exposure time of the SHWFS detector is set to 8 ms.

As seen on the right panel of Figure 3.16, each subaperture, after background subtraction, is characterised by the diffraction pattern of the lenslet array. Due their square aperture, the diffraction pattern of the microlenses follows a bidimentional $sinc^2$ pattern with sidelobes that slowly decay and pollute the adjacent subaperture. The result introduces a systematic bias on the estimated barycentre, shifting the estimated centroid close to the brightest subaperture and inducing noise correlation between subapertures, due to the subaperture cross-talk. To mitigate this effect, we defined a per-aperture background threshold that is defined has the 18% of the maximum intensity measured in the corresponding subaperture. We preferred a relative threshold compared to an absolute one, due to the non-uniform distribution of the flux across the subaperture set (caused by error alignments). This procedure, as we will see in Sec. 3.2.2, improves the estimation of the spot centroid at the price fo introducing truncation errors and non-linearities [42] in the response of the SHWSF. Figure 3.18, shows the benefits of the relative thresholding compared to a standard background subtraction on the acquired frame. To conclude, we compute the spots' average FWHM. On a selected fraction of subapertures, we computed the FWHM through a 2D Gaussian fit on a ROI of 8x8 pixel centred on the maximum intensity of each spot. Thus, the measured mean spots' FWHM is:

$$\mathrm{FWHM} = (7.1 \pm 0.3)\,\mathrm{pixel} \equiv (39 \pm 2)\mu\mathrm{m} \tag{3.45}$$

3.2.2 Linearity response

To quantify the SHWFS's dynamic range and the linearity response, we analysed the measured slope signals as a function of the commanded Zernike Tip-Tilt modes.

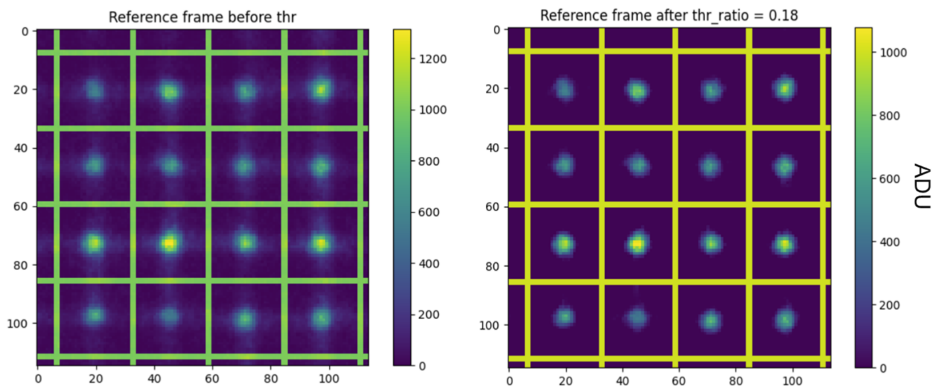

Figure 3.18. Mitigation of the subaperture diffraction sidelobes. On the left panel, a ROI of the acquired frame of the SHWFS that is simply background reduced. On the right panel, the corresponding frame after setting a per subaperture intensity threshold of the 18% of the maximum intensity measured for the related subaperture. The thresholding removes the diffraction side lobes, preserving the spots' core.

As mentioned, we expect that the adopted centroid intensity thresholded algorithm to estimate the spot position, induces non-linear effects on the SHWFS [42].

In the ideal case, without any aberration, we expect that a Tip or Tilt wavefront defined on the SLM circular pupil of diameter D induces an uniform spot shift Δ described as follows:

$$\Delta = \frac{f_2}{f_3}\frac{4c}{D} f_{la} \,, \tag{3.46}$$

where c is the Zernike Tip or Tilt coefficient, and where the term $4c/D$ is the slope of the commanded mode. The latter equation is computed relying on geometrical optics and the angular magnification of the commanded Tip/Tilt slope $4c/D$ due to the relay lens of L2 and L3. Thus, to check and verify the latter equation, we applied Tip and Tilt modes with different rms coefficients c, and measured the slope signals as a function of the commanded rms amplitude. From the acquired dataset, we estimated the average spot shift as the mean of the measured slope for each applied command. Figure 3.19 shows the measured slopes signals for the applied Tip and Tilt commands. For the applied commands in which the reflected SLM beam is not cropped by the FS, the SHWFS shows a linear response with a gain factor with respect to the expected ideal centroid shift (shown in red).

To estimate the gain, we execute a linear fit relying on the measured centroid shift assuming a linear model $\Delta^{fit} \propto m\, c$ where from the angular coefficient m we estimate the SHWFS gain as follows:

$$g = m \frac{f_3}{f_2}\frac{D}{4} \,. \tag{3.47}$$

The outcome analysis shows that the SHWFS is characterised by the following gains for the Tip (g_2) an Tilt (g_3):

$$g_2 = 0.80 \pm 0.03 \qquad \text{and} \qquad g_3 = 0.81 \pm 0.04 \,. \tag{3.48}$$

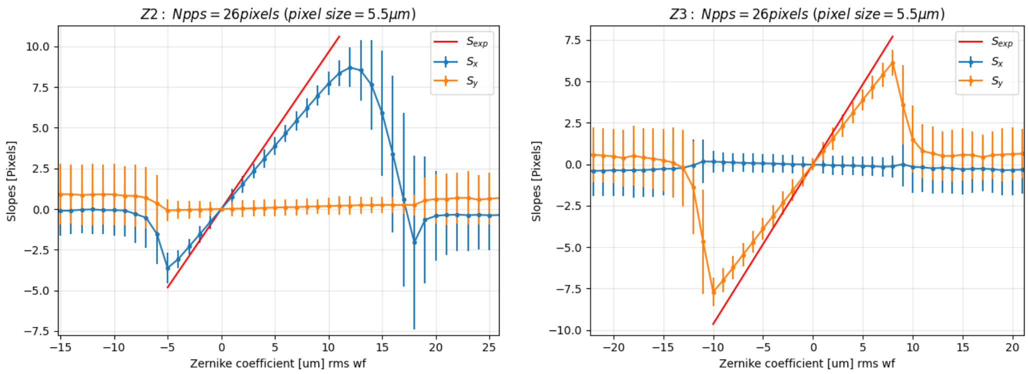

Figure 3.19. Response of the SHWFS to commanded Tip-Tilt (Z_2 and Z_3). On the left panel, the mean slopes signals are shown as a function of the Tip coefficient. On the right panel, are shown the ones measured as a function on the Tilt coefficient. The red line shows the expected centroid shift in the ideal case. In blue and orange are shown the measured slope signals x- and y- components, respectively. The error bars are the standard deviations of the measured signals across the subapertures. The SHWFS exhibits a linear response within a limited dynamic range, with a gain of 0.8. Outside the linear domain, the slopes go to zero as the beam is blocked by the field stop.

To conclude, the outcome analysis shows that the SHWFS has an effective gain $g_{eff} = 0.80 \pm 0.02$, computed as weighted mean of the measured gains g_2 and g_3. We measure a centroid shift that is $\sim 20\%$ smaller than the expected ideal case in both directions. This loss of gain is caused by the thresholded centre of gravity that cuts off the sidelobes of the spot [42], resulting in a reduction of the SHWFS dynamic range, while preventing subaperture cross-talk. In practice, synthetic control matrices are used in real AO systems: in this case, the gain compensation is needed in the wavefront reconstruction. In the present work, as we will see in the following, we rely on measured reconstruction matrices. Thus, no gain compensation is required and since we use calibrated interaction matrices.

3.2.3 Slope-to-command noise propagation

In this section, we provide a description of the characterised SHWFS noise. Particularly, to estimate how the slope noise is propagated to the reconstructed modal coefficients, we compute the temporal variation of the reconstructed modes for each dataset, when the SLM is set to a fixed flat command.

To do so, we perform a series of open-loops to sense and reconstruct the aberration coefficients of a chosen modal base from the measured slopes that are projected onto the reconstruction matrix. In this phase of the analysis, we reconstruct the system's aberrations by executing SCAO open-loops of N =1000 steps, setting the exposure time of the WFS at 8 ms and the SLM fixed to the flat command all over the loops. For the present analysis, we choose a Zernike modal base of 200 modes as we will see in Sec. 4.1 and open the loop setting the modal gain to zero, to avoid the modal command integration of the reconstructed modes between successive iterations. Thus, in each loop, the SHWFS computes the slope vector $\boldsymbol{s}(t)$ from the sensed absolute wavefront at each instant t, and it is then decomposed into the modal coefficients to infer the reconstructed modal coefficients vector $\boldsymbol{\Delta c}(t) = \{c_i(t)\}$, as follows:

$$\boldsymbol{\Delta c}(t) = R\, \boldsymbol{s}(t)\,, \tag{3.49}$$

where R is a measured Zernike reconstruction matrix. These datasets are used to characterised the static aberration of the test-bed, that will be discuss in Sec. 3.3.

Figure 3.20 shows the per-mode temporal evolution for different open-loops runs. The temporal variability of each reconstructed mode for a given dataset is computed as the standard deviation of the reconstructed coefficients $c_i(t)$. Finally, the slope-to-modal command noise σ_{s2c} is computed as the root-sum-squared of the per-mode standard deviation. Considering the average across the datasets, the slope noise propagation through the reconstructed modes contributes with $\sigma_{s2c} = (7.0 \pm 0.8)$nm. The present analysis is repeated by using a KL modal base of 200 modes, showing a compatible noise propagation of $\sigma_{s2c}^{KL} = 6.0 \pm 0.6$ nm rms wf.

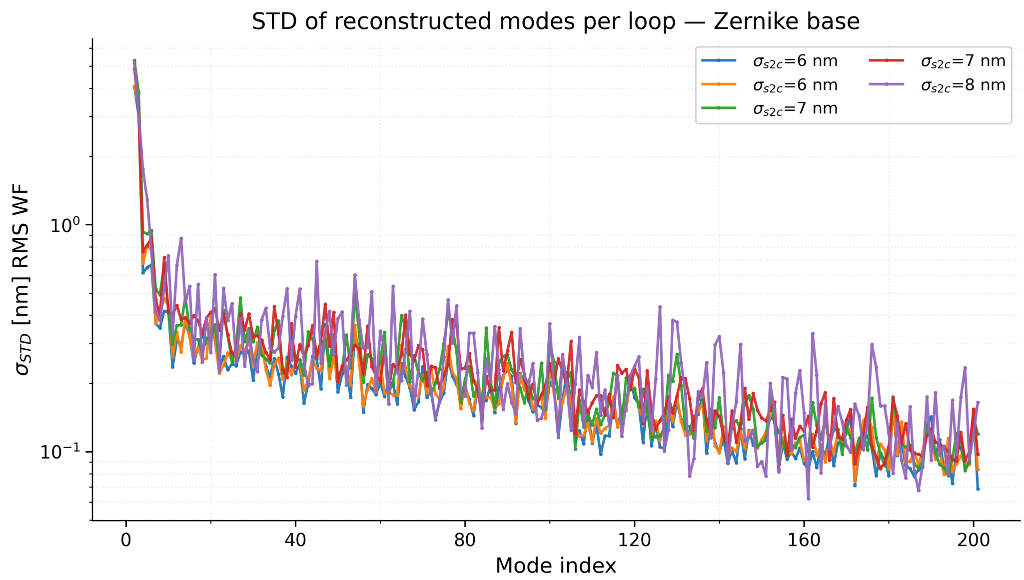

Figure 3.20. Temporal variability of the reconstructed Zernike coefficients in open-loops, with the SLM set to a fixed flat command and 8 ms of exposure time. The plot shows the per-mode standard deviation of a given open-loop. The colours correspond to different datasets acquired at intervals of ~ 2 weeks between each other, where the legend shows the measured slope-to-command noise for the corresponding dataset. Considering the average across the datasets, the propagated slope-to-command noise is $\sigma_{s2c} = (7 \pm 0.8)$ nm rms wf.

3.3 System's aberration characterisation

We want to estimate the static aberrations of the test-bench. These aberrations arise from residual alignment and manufacturing errors in the optical elements present in the bench, as well as from the intrinsic structure and properties of the SLM. In the following, we evaluate the system's aberration by means of the SHWFS.

3.3.1 Open-loop on system's aberration

We estimated and characterised the static aberrations of the test-bench, measuring directly the absolute wavefront in SCAO mode. To do so, we analysed the same open-loops reconstructed modes as described in Sec.3.2.3. Furthermore, we evaluated the temporal stability of the bench, analysing the temporal evolution of the measured aberrations.

To estimate the static aberration modal components, we computed the average $\langle \Delta\mathbf{c}(t) \rangle$ of the reconstructed modal vectors $\Delta\mathbf{c}(t)$ (the same from Eq.(3.49)) over time. Figure 3.21 shows the mean reconstructed coefficients c_i from the average vector $\langle \Delta\mathbf{c}(t) \rangle$, inferred from different open-loop acquired at intervals of ~ 2 weeks between each other. In the latter figure, we reported the mean (in magenta) and standard deviation (light blue interval) of the c_i coefficients estimated across the different datasets. The main contribution to the system's aberration is located in the low-order modes (left panel of the aforementioned figure), which are more sensible to misalignment between loop sessions. Particularly, we reported the measured mean Tip, Tilt and Focus coefficients across the different datasets in Table 3.2. The table shows that the Tip and Focus modes are stable between successive loops, with a temporal relative variability of $\lesssim 3\%$ and $\lesssim 1\%$ for the Tip and Focus modes, respectively. On the other side, the Tilt exhibits higher sensibility between the loop sessions, showing a relative temporal variability of $\sim 18\%$.

Mode	Coefficient c_j [nm] RMS WF
Tip ($j = 2$)	2560 ± 68
Tilt ($j = 3$)	-397 ± 73
Focus ($j = 4$)	-1478 ± 13

Table 3.2. Measured coefficients c_j on the low-order modes. The reported values correspond to the mean and standard deviation across the different datasets.

To quantify the test-bench temporal stability, we compute the wavefront error (WFE) measured on the reconstructed coefficients in each executed loop. We compute the WFE as the sum-root-squared of the mean modal coefficients c_i from the average vector $\langle \Delta\mathbf{c}(t) \rangle$:

$$\mathrm{WFE} = \sqrt{\sum_i c_i^2} \tag{3.50}$$

Figure 3.22 shows the cumulative RMS coefficients, namely the per-mode accumulated WFE, for the acquired open-loop datasets. The plot shows that most of the system's aberrations are distributed in the low-order modes, Tip, Tilt and Defocus. As shown in the latter figure, these 3 modes contributes for the 99.89% of the total WFE due to the static aberrations of the bench. Finally, the mean (and standard deviation) of the WFE measured across the dataset is 2986 ± 72 nm RMS WF: this shows that the bench has a relative temporal stability within $\sim 2.4\%$ in 10 weeks. Finally, after filtering the low-order modes (Tip, Tilt and Defocus) the residual WFE due to the alignment is 134 ± 3nm rms wf, with a temporal variability of 2%.

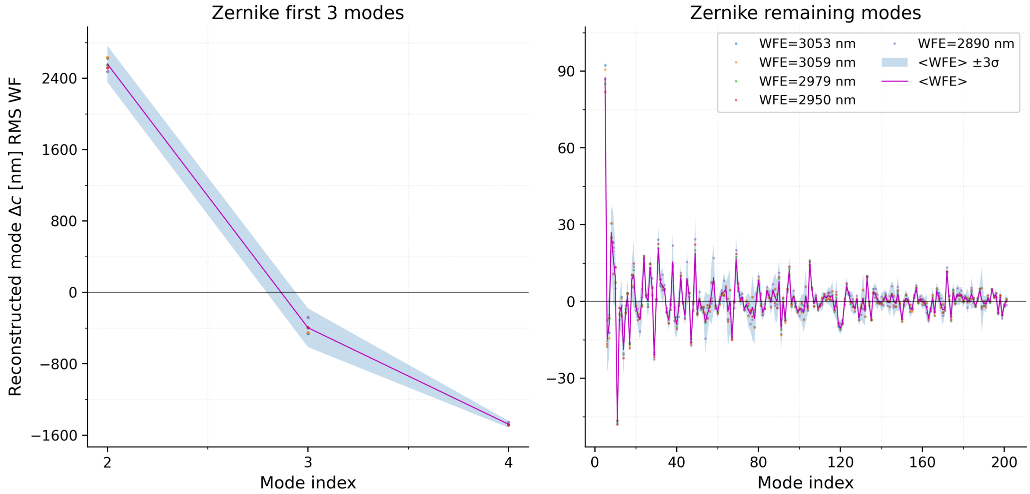

Figure 3.21. Reconstructed Zernike coefficients c_i from SCAO open-loops without turbulence to estimate test-bench's aberrations. The datasets are separated into two plots (on the left panel only Tip, Tilt and Defocus are shown, while on the right one the remaining others) for better visualisation. The coloured dots are the modal coefficients c_i measured from the average open-loop reconstructed modal vector $\langle \Delta \mathbf{c}(t) \rangle$ for different datasets. The magenta line is the mean of the measured coefficients c_i across the different dataset, while the light blue band is the interval region $\pm 3\sigma$ around the mean, where σ is standard deviation of the measured coefficients c_i across the dataset. The legend reports the measured wavefront error (WFE) for each dataset. Each dataset is acquired at intervals of ~ 2 weeks.

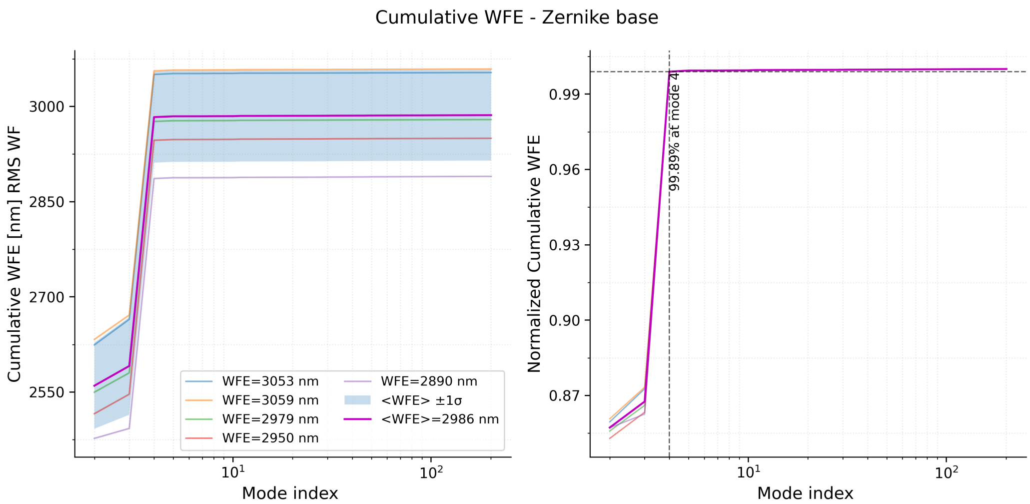

Figure 3.22. Per-mode WFE cumulative. On the left the measured cumulative WFE for each dataset. On the right, the same data normalized to the respective WFE. The static aberrations are mainly due to the Tip, Tilt and Defocus modes that contribute for the 99.89% of the total.

To conclude, the same presented analysis is repeated by projecting the measured slope vectors of the open-loop datasets onto the KL modal basis of 200 modes, whose measured WFEs are reported in the latter table.

	WFE [nm]	TTF filtered [nm]
Zernike	2986 ± 72	134 ± 3
KL	3009 ± 72	102 ± 2

Table 3.3. Comparison of the measured WFE of the bench static aberrations using Zernike and KL bases. The right column corresponds to the WFE computed by filtering Tip, Tilt and Defocus. The values are the RMS WF mean ± standard deviation computed across datasets.

Chapter 4

Testing AO Loops

After the characterisation of the SLM-based SCAO test-bench, in this chapter, we describe the analysis and tests aimed to prototype hardware-in-the-loop simulations. Particularly, in Sec.4.1 we measured and test the control matrices to be used in the AO loops. In Sec.4.2, we compensated for the static aberration affecting the bench by a sensorless and SCAO closed-loop approach. Finally, in Sec.4.3 we discussed the test performed to compensate for atmospheric turbulence in SCAO closed-loops.

4.1 Control matrices calibration

The estimate of the control matrices consists of measuring the interaction matrix $\boldsymbol{H}$ that maps modal commands to the sensor outputs, in this case, the slopes. As seen in Sec.1.2.4, in a modal control, each column of $\boldsymbol{H}$ is the SHWFS response in the slope space to a commanded mode. Similarly to the zonal control, we measured the modal "influence functions" in the WFS space, by applying individual Zernike modes and recording the corresponding slope signals. For each Zernike mode j, we applied a push-pull sequence and measured the corresponding SHWFS slopes. The WFS response is acquired by measuring the slope signal after applying on the SLM a given Z_j Zernike mode with a known rms amplitude α_j. Particularly the push-pull signals, $\boldsymbol{s}_j^{push}$ and $\boldsymbol{s}_j^{pull}$, are the SHWFS' responses due to the application of $\pm\alpha_j Z_j$ on the SLM. The difference of the two signals is normalized to the applied modal coefficient as follow:

$$\hat{\boldsymbol{s}}_{\boldsymbol{j}} = \frac{\boldsymbol{s}_j^{push} - \boldsymbol{s}_j^{pull}}{2\,\alpha_j} \tag{4.1}$$

The difference between the 2 slope signals allows to subtract any static aberration and allows to maximise the WFS's response, to the advantage of the SNR. The 2 measurements taken in a rapid sequence allow for the rejection of slow drifts in the system. The rms amplitude α_j is empirically chosen small enough to remain in the linear regime of the SHWFS and large enough to dominate sensor's and slope noise. Finally, the interaction matrix $\boldsymbol{H}$ is computed by stacking all the measured response $\hat{\boldsymbol{s}}_{\boldsymbol{j}}$ to the commanded polynomials:

$$\boldsymbol{H} = [\hat{\boldsymbol{s}}_{\boldsymbol{2}}, \hat{\boldsymbol{s}}_{\boldsymbol{3}}, ..., \hat{\boldsymbol{s}}_{\boldsymbol{J}}]\,, \tag{4.2}$$

while the reconstruction matrix $\boldsymbol{R}$ is computed with its pseudo-inverse as seen in Sec.1.2.4. We measured the control matrices of the first 200 Zernike modes, with a push-pull rms amplitude that scales with the Zernike radial order. This choice is due to the fact that, as seen in Sec.1.1.2, the atmospheric PSD decreases with the Zernike polynomial radial order: so calibrating with smaller amplitudes is physically representative. Furthermore, high-order Zernikes are characterised by steeper local phase gradients: high rms amplitudes may cause large local Tilts that are cropped by the field stop, losing flux on the subapertures set.

So, a first calibration was performed assuming a push-pull vector such that commanded rms amplitude $\alpha_j = 2\mu m/n$, where n is the radial order of the Zernike polynomial. However, this results in a huge modal command for high-order polynomials (high spatial frequency structure with huge local slopes) that causes overshadowing of several subapertures, especially at the edge of the pupil. So another attempt was to reduce the amplitude of the push-pull vector, scaling with the radial order squared, such that $\alpha_j = 5\mu m/n^2$. However, as shown in Figure 4.1, only a few low-order modes show a good slope signal while the others are not sensed by the SHWFS.

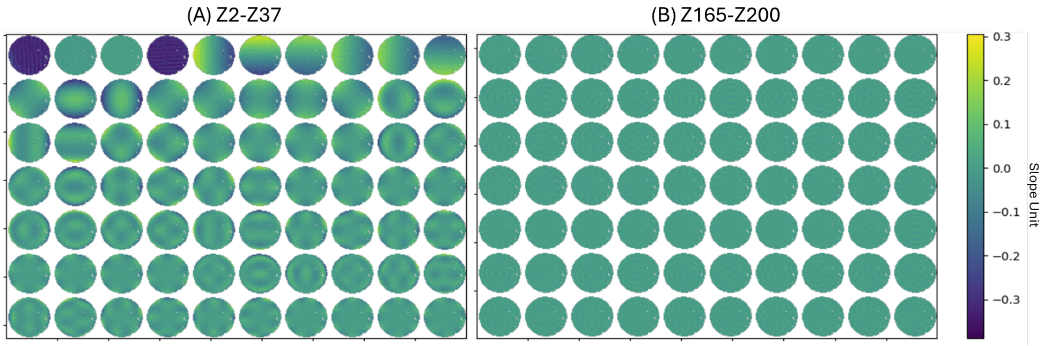

Figure 4.1. Slope maps obtained from the push-pull calibration (i.e. the map for the vector $\hat{\boldsymbol{s}}_{\boldsymbol{j}}$). On the left (panel A), low-order modes show a good signal response. On the right (panel B), high-order modes are not sensed by the SHWFS. In the two panels are shown the X and Y slopes maps for mode. The slope maps are obtained by applying a push-pull sequence of rms amplitudes $\alpha_j = 5\mu m/n^2$, where n is the radial order of the polynomial.

Thus, to estimate a proper push-pull command that is sensed by the SHWFS we adopt an iterative approach. To quantify the per-mode signal visibility to a commanded push-pull sequence, we compute the standard deviation of the measured response signals $\hat{\boldsymbol{s}}_{\boldsymbol{j}}$. Figure 4.2 (left) shows the per-mode signals visibility for different calibrations. To improve the signal, we rescaled the rms amplitude push-pull of each coefficient by setting a target value for the expected standard deviation of the slope on the standard deviation across the elements of $\hat{\boldsymbol{s}}_{\boldsymbol{j}}$. We selected a target value $\sigma_t = 0.1$ (in slope units, i.e. defined in unitary circle that represents the lenslet aperture) for all the modes except for Tip and Tilt. Thus, the rescaled push-pull amplitudes are computed iteratively as follows:

$$\alpha_j^{k+1} = \frac{\sigma_t}{\sigma_j^k}\alpha_j^k\,, \tag{4.3}$$

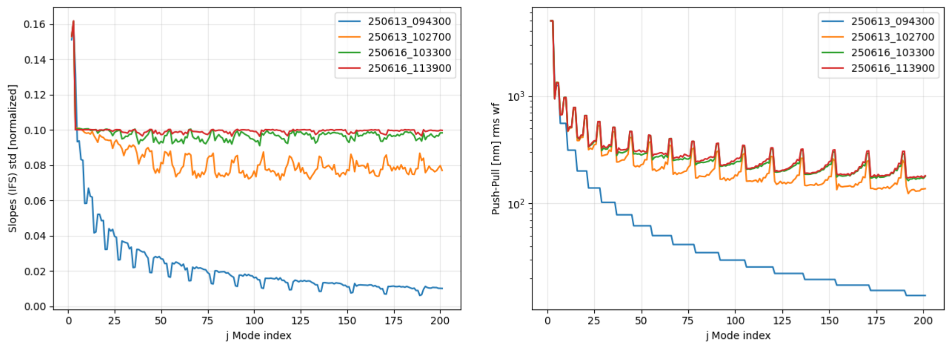

Figure 4.2. Optimisation of the signals measured by the SHWFS by the rescaling of the rms amplitude of the push-pull sequence. On the left panel the standard deviation of the signals in $\hat{\boldsymbol{s}}_{\boldsymbol{j}}$ for each mode. On the right the corresponding per-mode push-pull commands. The coloured curves correspond to the optimised measured signals and the corresponding push-pull command.

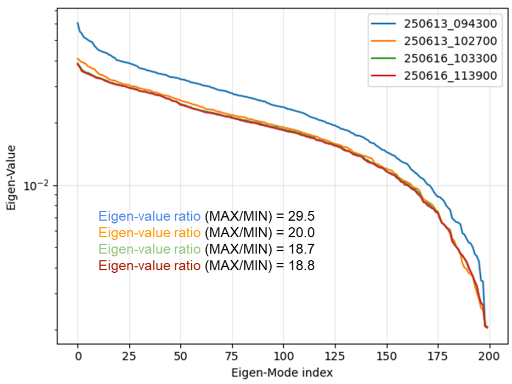

Figure 4.3. Estimated singular values λ_i from the different optimised calibrations. λ_i has the units of [slope unit/m^2].

where k is the iteration step and σ_j^k is the standard deviation across components of the measured signal $\hat{\boldsymbol{s}}_{\boldsymbol{j}}^{\boldsymbol{k}}$. The right panel shows the rescaled push-pull rms amplitude command. The multiple iterations converged to the selected target. Finally, as for smaller λ_i greater is the noise propagation on the reconstruction, we quantify the ratio of the maximum to the minimum eigenvalue for each optimisation. A larger ratio implies greater noise amplification and poorer visibility of some modes that are combined, whereas a smaller ratio indicates well conditioned and robust sensing.

As a cross-check, as seen in Sec.1.2.4, we analyse the eigen-values λ_i from the SVD, since they provide how well the SHWFS has been able to distinguish the eigenmodes. Figure 4.3 shows the computed eigen-values for the different measured interaction matrices. Thus, as shown in Figure 4.4, the optimisation provided a better conditioning with lower noise propagation and increasing SHWFS visibility, especially to higher order modes. From the optimised push-pull command, we measured the final Zernike control matrices.

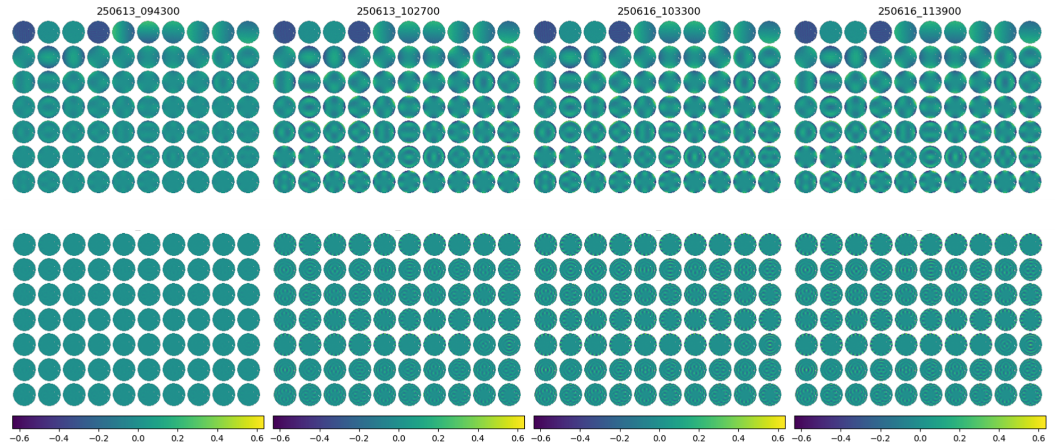

Figure 4.4. Improvement of the push-pull command rescaling on the slopes maps. On the first row the X and Y slopes maps are reported for the polynomial Z_2 to Z_{37}. While on the last row the higher order modes are shown from Z_{165} to Z_{200}. The rescaled calibrations (from the second column) exhibit a clear improvement on the high-order modes sensed by the SHWFS, in contrast to the first one (on the first column, which is the same set shown in Figure 4.1.

4.2 System's aberration compensation

We want to compensate for the static aberrations of the test-bench. However, these may differ from the sensing path due to the optical path difference between the science and SHWFS camera. In the following sections, we describe two different approaches: the first through a sensorless approach, which evaluates the system's aberration from the PSF response to known aberrations, and the second one performing a SCAO closed-loops.

4.2.1 Sensorless approach

We want to estimate and compensate for the static aberrations of the test-bench in the science camera optical path, relying on a sensorless approach. Without using the WFS, the aberrations are estimated from the PSF response to known injected modes in the bench. For the present analysis, we considered low-order Zernike polynomials, as these are directly related to the main alignment and manufacturing aberrations (such as focus, coma, astigmatism, among others). The PSF response to the explored aberrations is quantified through the SR metrics, as a function of the injected modal command $c = \{c_j\}$. The aim is to find the best modal command vector $\hat{c} = \{\hat{c}_j\}$ that maximise the SR.

To do so, we measured the SR for each selected Zernike mode Z_j as a function of the commanded RMS amplitude c_j on the SLM. For a given mode, we acquired the on-axis PSF and computed the SR as follows:

$$\mathrm{SR}(c_j) \; = \; \frac{I^{meas}_{peak}(c_j)}{I^{DL}_{peak}} \, , \tag{4.4}$$

where I^{meas}_{peak} and I^{DL}_{peak} are the peaks of the measured and diffraction-limited PSF (for further details see Appendix C). The optimised coefficient $\hat{c}_j$ is inferred from the cubic-spline interpolation $S_j(c)$ computed on the measured SR(c_j) points and it is defined on a dense grid $[c_{min}, c_{max}]$ of step $\Delta c = 5\ nm$. We estimated $\hat{c_j}$ as the amplitude corresponding to the maximum value of the SR interpolated function:

$$\hat{c_j} \;=\; \arg\max_c \; S_j(c) \qquad \text{with } c \in [c_{min}, c_{max}] \tag{4.5}$$

Once the optimised coefficient $\hat{c}_j$ is computed, this was set as an offset on the commanded phase, while scanning the SR as a function of the RMS amplitude for the next explored Zernike modes.

To quantify the uncertainty on estimated $\hat{c}_j$, we used the local curvature of the interpolated function $S_j(c)$ around its maximum. For c amplitudes close to $\hat{c}_j$, the interpolated function $S_j(c)$ is well approximated by its second-order Taylor expansion:

$$S_j(c) \;\approx\; S_j(\hat{c}_j) \;-\; \frac{\kappa_j}{2}\,(c-\hat{c}_j)^2 \tag{4.6}$$

where κ_j is the local curvature $\kappa_j = -S_j''(\hat{c}_j) > 0$. A variation in SR corresponds to:

$$\delta S \;\approx\; \frac{\kappa_j}{2}\;\delta c^2 \; .$$

Thus, for $\delta S \sim \sigma_{SR}$, we obtain a coefficient variation $\delta c \sim \sigma_c$ equal to:

$$\sigma_c \;\approx\; \sqrt{\frac{2\;\sigma_{SR}}{\kappa_j}} \; . \tag{4.7}$$

Finally, the error on the estimated mode coefficient $\hat{c_j}$ is given by:

$$\sigma_{\hat{c}_j} \;=\; \sqrt{\frac{2\,\sigma_{\mathrm{SR}}}{\kappa_j} \;+\; \frac{\Delta c^2}{12}} \; . \tag{4.8}$$

In practice, κ_j is computed from the second derivative of the spline and σ_{SR} is to the mean of the errors $\sigma_{\mathrm{SR},k}$ of the measured K points (typically $K = 3$–5) with largest SR and close to the maximux. Since $\hat{c}_j$ is obtained by evaluating S_j on a dense grid $[c_{min}, c_{max}]$ of step Δc, we accounted for the quantisation error by adding in quadrature the contribution $\sigma_q = \Delta c/\sqrt{12}$.

Figure 4.5 (top panel), shows the measured SR for the Defocus (Z_4) to Spherical (Z_{11}) modes, defined in a circular pupil of diameter 1090 pixel in the SLM. The applied modal command spanned in a range with RMS amplitude $c_j \;\in [-2.5, +2.5]\ \mu m$ wavefront, with sampling steps 100 nm.

To get a better estimation of $\{\hat{c}_j\}$, we iterated the optimisation exploring the PSF response to the same modes and loading the estimated coefficients in Table 4.1 as an offset command on the SLM. As shown in Figure 4.5 (middle panel), we reduced the range of the injected RMS amplitudes, with $c_j \;\in [-100, +100]\ nm$ rms wavefront using increments of 20 nm.

Loading the estimated optimised coefficients from the data set sampled at $\Delta c = 10$ nm as offset command, we compensated for higher order modes to observe improvements on the PSF compensation from residual static aberrations. In the bottom panel of the latter figure are shown the measured SR for the optimisation

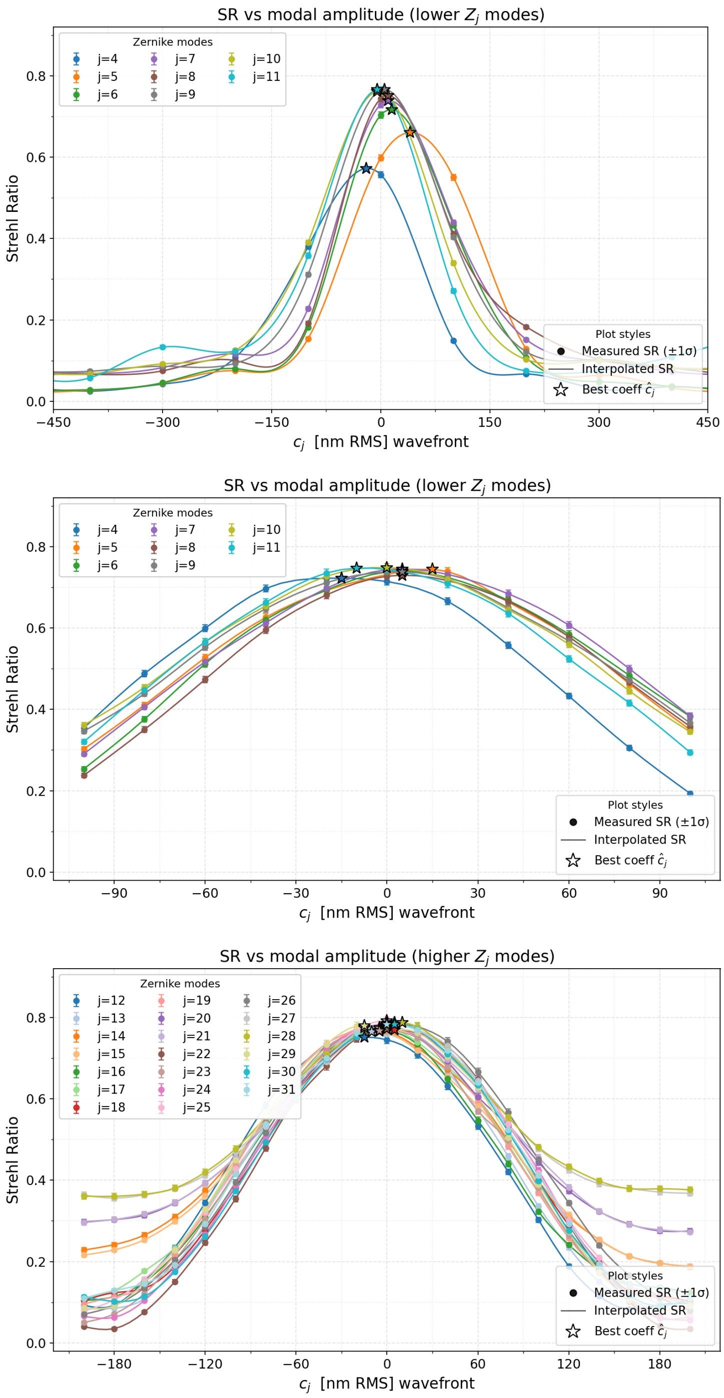

Figure 4.5. Measured SR as a function of the commanded rms amplitude for each mode. From the top panel, the measured SR (dots) and interpolations (curves) are shown as a function of the injected rms amplitude of a given mode Z_j, for the coarser and finer sampling of low-order modes and the one for the higher order modes.

Mode	$\hat{c}_j$ [nm] ($c_j \in \pm 2.5$ μm @ 100 nm)	$\hat{c}_j$ [nm] ($c_j \in \pm 100$ nm @ 20 nm)
$j = 4$	-20 ± 10	-15 ± 19
$j = 5$	40 ± 12	15 ± 9
$j = 6$	15 ± 9	5 ± 11
$j = 7$	10 ± 9	5 ± 11
$j = 8$	10 ± 8	5 ± 11
$j = 9$	5 ± 9	5 ± 13
$j = 10$	-5 ± 9	0 ± 13
$j = 11$	-5 ± 10	-10 ± 11

Table 4.1. Best coefficients $\hat{c}_j$ (nm RMS) per Zernike mode for optimisation on the lower order modes.

of the higher order modes, from Z_{12} to Z_{33}. Figure 4.6 summarises the estimated coefficients of the previews datasets (panel a) and shows the ones obtained from the injection of the polynomials Z_{12} to Z_{33} (panel b), with RMS amplitude $c_j \in [-200, +200]$ nm wavefront, with steps of 20 nm.

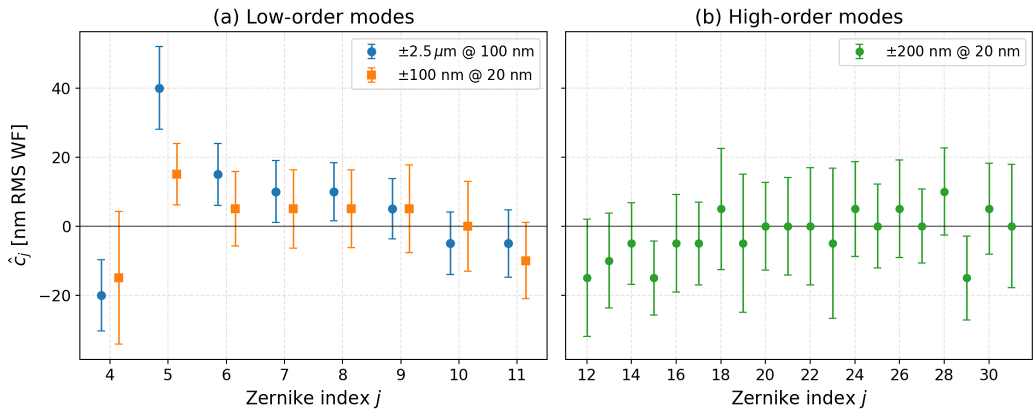

Figure 4.6. Best Zernike coefficients $\hat{c}_j$ (nm RMS WF) with 1σ uncertainties from the SR-based sensorless procedure. (a) Low-order modes: comparison between a coarse, wide sampling (± 2.5 μm @ 100 nm) and a fine, focused scan (± 100 nm @ 20 nm). (b) High-order modes from a ± 200 nm @ 20 nm sampling

To estimate the effectiveness of the optimised coefficients, we measured the SR temporal evolution under the fixed optimised modal command $c = \{\hat{c}_j\}$ applied on the SLM. For each command, we acquired $N = 1000$ frames at an exposure time of $t_{\rm exp} = 6$ ms and a frame rate of 18 Hz. The SR is measured on each frame t using the same ROI. In Table 4.2 the time average SR and standard deviation for the different optimised modal commands are reported. The results show a large improvement in SR of about 60% with respect to one related to the flat command when correcting low-order modes up to Z_{11}. However, iterating the optimisation on the lower and then extending to higher orders (Z_4–Z_{31}) doesn't show any improvement on the time-averaged SR (from 80.8% to 81.0%, which is well within the observed temporal dispersion $\sim 1\%$). On the other side, the sensorless optimisation provided a PSF

SLM command	$\langle \mathrm{SR} \rangle_t$ [%]	$\langle \mathrm{FWHM} \rangle_t$ [px]
Flat $c = \{0\}$	54.7 ± 0.8	4.20 ± 0.02
$c = \{\hat{c}_j\}$ from Z_4–Z_{11} (*coarse scan*)	79.9 ± 0.9	3.64 ± 0.01
$c = \{\hat{c}_j\}$ from Z_4–Z_{11} (*fine scan*)	80.8 ± 0.9	3.64 ± 0.01
$c = \{\hat{c}_j\}$ from Z_4–Z_{31}	81.0 ± 1.0	3.66 ± 0.01

Table 4.2. Time-averaged SR and FWHM over $N = 1000$ frames ($t_{\mathrm{exp}} = 6$ ms, 18 Hz) for different optimised coefficient sets $\hat{c}_j$ commanded on the SLM. We remind that the camera pixels pitch is 4.65 μm and the DL FWHM is 3.49 pixels.

with an average FWHM of 3.64 pixel that remains 4.3% broader than the DL value ($\mathrm{FWHM}_{DL} = 3.49 \pm 0.03$ pixel), with a discrepancy of $\sim 5\sigma$, despite the $\sim 15\%$ improvement with respect to the flat case. Figure 4.7 gives a summary and a visual description of the outcome analysis.

Thus, we concluded that correcting beyond Z_{11} does not provide a significant gain in SR for which the residual variability is dominated by temporal fluctuations rather than by uncorrected low-order static aberrations. In addition, extending the optimisation to Z_{31} does not bring a statistically meaningful improvement in FWHM under our operating conditions. Further improvements can be achieved by compensating for higher-order aberrations.

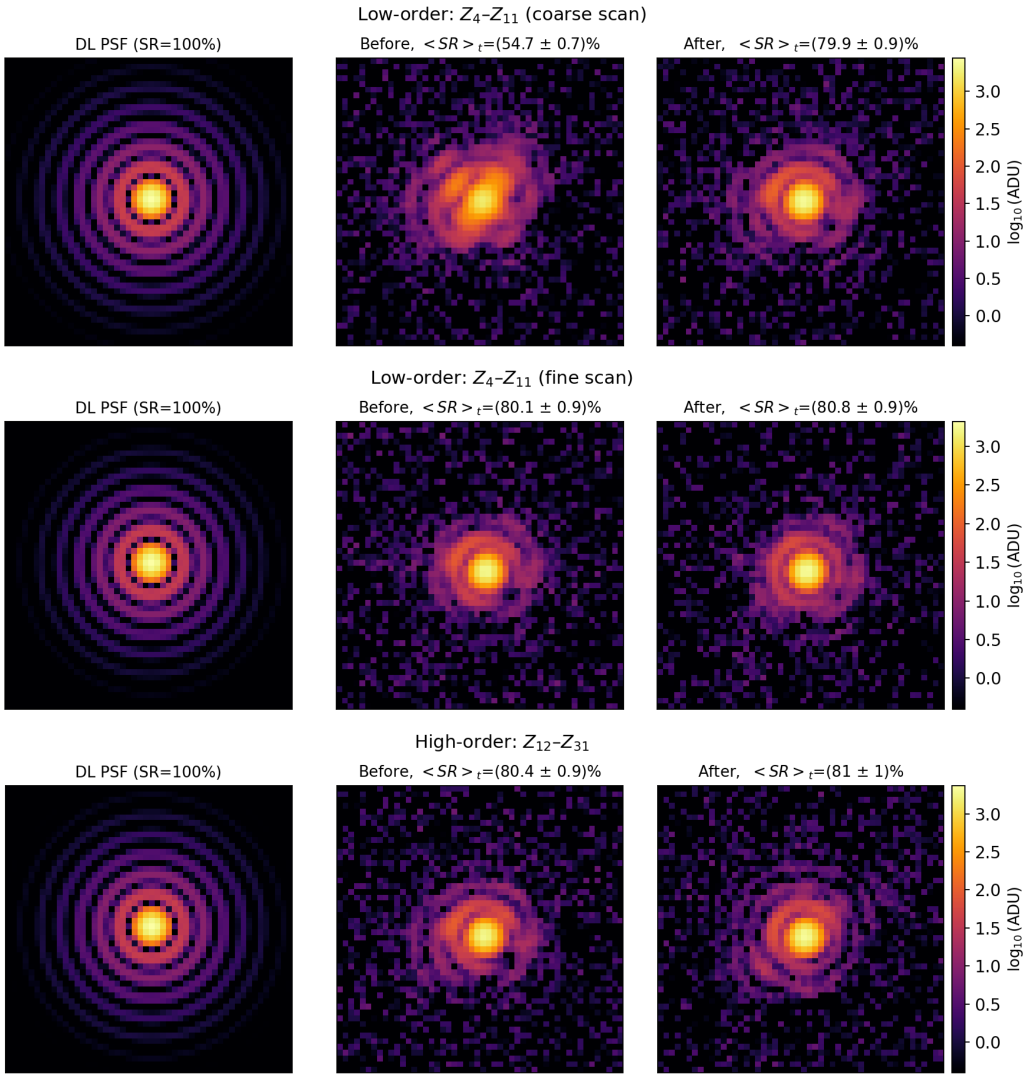

Figure 4.7. PSF response to sensorless compensation. From the top to the bottom panels are reported the optimisation cases injecting low (with a coarse and finer sampling, corresponding to the top and middle panels, respectively) and higher order modes. In each panel, the DL and measured PSF before and after the compensation are shown from the left to the right. The measured PSF are computed as average of 10 frames (for expository reasons), while the SR is estimated from mean of measured SR frame by frame.

4.2.2 SCAO closed-loop

To compensate for the static aberrations of the bench, we performed closed SCAO loop. This process consists to estimate the modal commands that nulls the WFS. As a cross-check for the measured and optimised calibration, we expect that the residual of the compensated aberration is within the slope-to-command noise seen in Sec.3.2.3. Adopting a simple integrator, at each step of the loop the measured slope $\boldsymbol{s_t}$ are projected onto the reconstruction matrix to obtain the modal corresponding vector of the modal coefficient as follows:

$$\Delta \boldsymbol{c} = \boldsymbol{R}\, \boldsymbol{s_t}\,, \tag{4.9}$$

then the modal command is integrated as follows:

$$\boldsymbol{c}_{t+1} \;=\; \boldsymbol{c}_t - g\, \Delta \boldsymbol{c} \tag{4.10}$$

where g is the gain. Finally, we reconstructed the integrated wavefront W_{t+1} that is commanded on the SLM as follows:

$$W_{t+1} \;= \boldsymbol{H}_s\; \boldsymbol{c}_{t+1}\,, \tag{4.11}$$

where $\boldsymbol{H}_s$ is a numerical computed interaction matrix, that mimics an ideal WFS sensible to the first derivative of the wavefront (i.e the columns of $\boldsymbol{H}_s$ are the column stacked numerical derivatives of the modal base). So, we performed a closed-loop on the static aberration with a measured calibrated reconstruction matrix of the 200 Zernike modes. We set the SLM to the flat command and set a gain $g = 0.2$ and iterate the loop in 300 steps. With reference to Figure 4.8, the outcome analysis

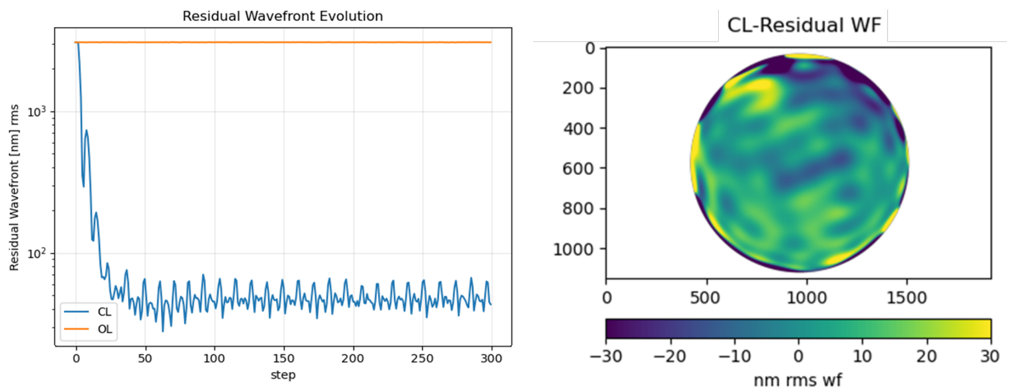

Figure 4.8. Results for closing the loops on the static aberrations. On the left panel, the measured WFE in closed-loop (blue) is shown as a function of the time step. In orange the WFE measured on open-loops. The image is saturated for expository reasons. At convergence the residual error is 46 nm rms wf. On the right panel, the wavefront residual map at the end of the loop. The wavefront is of few nm in the inner regions of the pupil while has steep gradient at the edge that are responsible of a PtV of$\sim 2\mu$m wf.

shows that the residual wavefront error is 48 nm rms wf. However, the residual wavefront shows a PtV of 2083 nm wf. This is due to the edges of the residual wavefront, that typically occurs when using Zernike polynomials. As discussed, high-order polynomials are responsible of steep local gradients that, increasing with the radial order of the Zernike, moved to the pupils' edge with structure at high spatial frequency that the SHWFS is not capable to sense.

For this reason, for the following discussion we adopted and measured a Karhunen-Loève (KL) basis [32]. This is optimised for the turbulence statistics and the geometry and implementation of the phase compensator. It diagonalizes the phase covariance and minimises the residual variance for a given number of degrees of freedom. This base is numerically computed from the zonal influence function of numerically simulated 41×41 actuators on a circular pupil of 8.2 m. We repeated the closed-loop using a KL modal base of 200 modes setting a gain of $g = 0.3$. In this case we measured a residual wavefront error of 6 nm rms, which is within the slope-to-command noise. Figure 4.9 shows an example of a wavefront resulting from the open and closed-loop of the static aberration. The residual wavefront has an rms amplitude of 5 nm and a PtV of 26 nm wf.

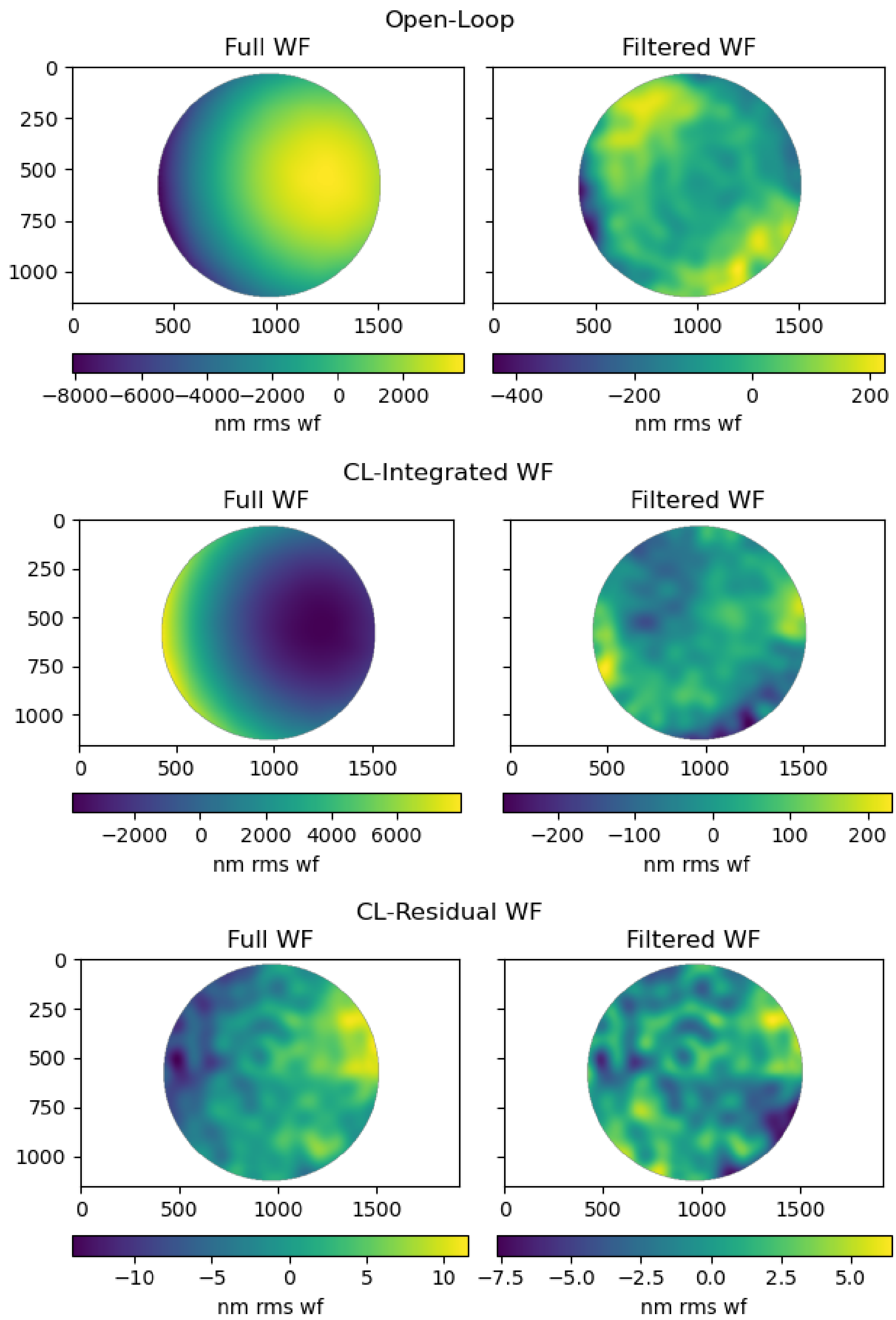

Figure 4.9. Compensation of the static aberrations. From the top to the bottom panels a measured open-loop wavefront, the integrated wavefront applied on the SLM, and residual at convergence of the closed-loop are reported. For all cases, the full and filtered (Tip-Tilt-Defocus removed) are shown. Compared to the Zernike case, we measured a PtV of only 26 nm wf on the residual wavefront.

4.3 Compensating for the atmospheric turbulence

In this section, we describe the analysis performed to properly inject and compensate for the atmospheric turbulence on the SLM-based testbench. In particular, in Sec.4.3.1 we tested the accuracy of SPECULA in reproducing turbulent wavefronts over a ELT- and VLT-like pupil diameters. Finally, in Sec.4.3.2, we described the results of the prototyped SCAO closed-loop in compensating for the atmospheric turbulence. As discussed in Sec.2.4.1, it is worth noting that, in this stage of the project, we were not interested to reproduce the same ELT's turbulence and MORFEO's WFS sampling and compensation conditions on the test bench. This would required a 68×68 SHWFS, as the one foreseen for MORFEO, and the simulation of a DM with ~ 5000 actuators, such as M4 on ELT. Instead, the work was aimed at prototyping hardware-in-the-loop simulation. Thus, although the employed SHWFS's subaperture set of ~ 41 lenslet along the diameter undersamples the turbulent wavefront in VLT- and ELT-like pupils, and the simulated DM has 41×41 actuators, the SCAO closed-loops were restricted to good-seeing conditions in a pupil of 8.2 m at the working wavelength of 633 nm. This choice defines the subaperture size on the pupil plane to be $\lesssim r_0$, partially mitigating the WFS aliasing and fitting error (seen in Sec.1.2.5) but still allowed us to test and validated the prototyped SCAO closed-loop. Further details will be discussed in Sec.4.3.2.

4.3.1 Testing SPECULA generated turbulent phase

Before executing AO simulation by means of the SLM-based SCAO, we performed numerical simulations to check the accuracy of the generated phase screen by SPECULA. To do so, we reproduced the atmospheric temporal evolution on a numerically simulated open-loop without the WFS sensing measurement and DM compensation. At each time step of the atmospheric turbulence evolution, the phase map is decomposed into modal coefficients through its projection on a synthetic reconstruction matrix (i.e. the one obtained from the pseudo-inverse of the synthetic interaction matrix of an ideal first derivative WFS). The modal decomposition is performed after the numerically simulated propagation of the phase screen on the telescope pupil. For the present analysis, we decomposed the atmospheric turbulent phase on a Zernike modal base of 200 polynomials, on a circular pupil without any obstructions. As seen in Sec.1.1.2, the variance of each Zernike is related to the turbulence statistics. The turbulent phase propagation is realised by considering an on-axis propagation of the turbulence on the telescope pupil and a constant wind speed of 5 ms along the x direction of the pupil plane of size D. We performed a series of 300 open-loop runs, simulating the turbulence evolution over 5 s with a time step of 1 ms. For each run, a randomly generated seed is used. In Table 4.3 are shown the parameters used for the different examined case to test Von Karman and Kolmogorov PSD models generated by SPECULA. The seeing ϵ is defined at $\lambda = 500$nm. Particularly, we measured the per-mode variance of the reconstructed modes and compared it to the expected one from theory. To quantify the discrepancy between the phase screen generated by SPECULA and the theory, we computed the

Table 4.3. Parameters used for the simulations for the different cases. The seeing ϵ is defined for the visible ($\lambda = 500$nm), and the turbulence is propagated on the telescope pupil with diameter D on the on-axis direction, assuming an given outer scale L_0. We assume a single turbulent layer over the pupil and a constant wind speed of 5 m/s. The simulation time is of T=3 s with a time step of 1 ms.

Case	ϵ [arcsec]	L_0 [m]	D [m]
A	0.3	23	40
B	1.0	40	8
C	1.0	∞	8

root mean square error (RMSE) as follows:

$$\sigma_{RMSE} = \sqrt{\frac{1}{N}\sum_j \left(\frac{c_j^{ol} - c_j^{th}}{c_j^{th}}\right)^2}\,, \tag{4.12}$$

where N is the number of modes, c_j^{ol} is the jth decomposed coefficient and c_j^{th} is the one expected.

Figure 4.10 shows the per-mode temporal standard deviation for each run. With reference to the latter table, when simulating the atmospheric turbulence on 8 and 40 m of pupil using Von Karman PSD, we measured a RMSE of $\sim 5\%$ and $\sim 6\%$ for the case A and B, respectively. On the other side, when we assumed the Kolmogorov model (Case C), we incurred in numerical errors. Further studies are required to understand the nature of these outliers in the low-order modes. From now on, we will assume the Von Karmat PSD model to simulate turbulence propagation with SPECULA. The RMSE values obtained in cases A and B can be mitigated by increasing the number of simulations and increasing the simulation time, taking into account the decorrelation of the low-order modes as seen in Sec.1.1.3.

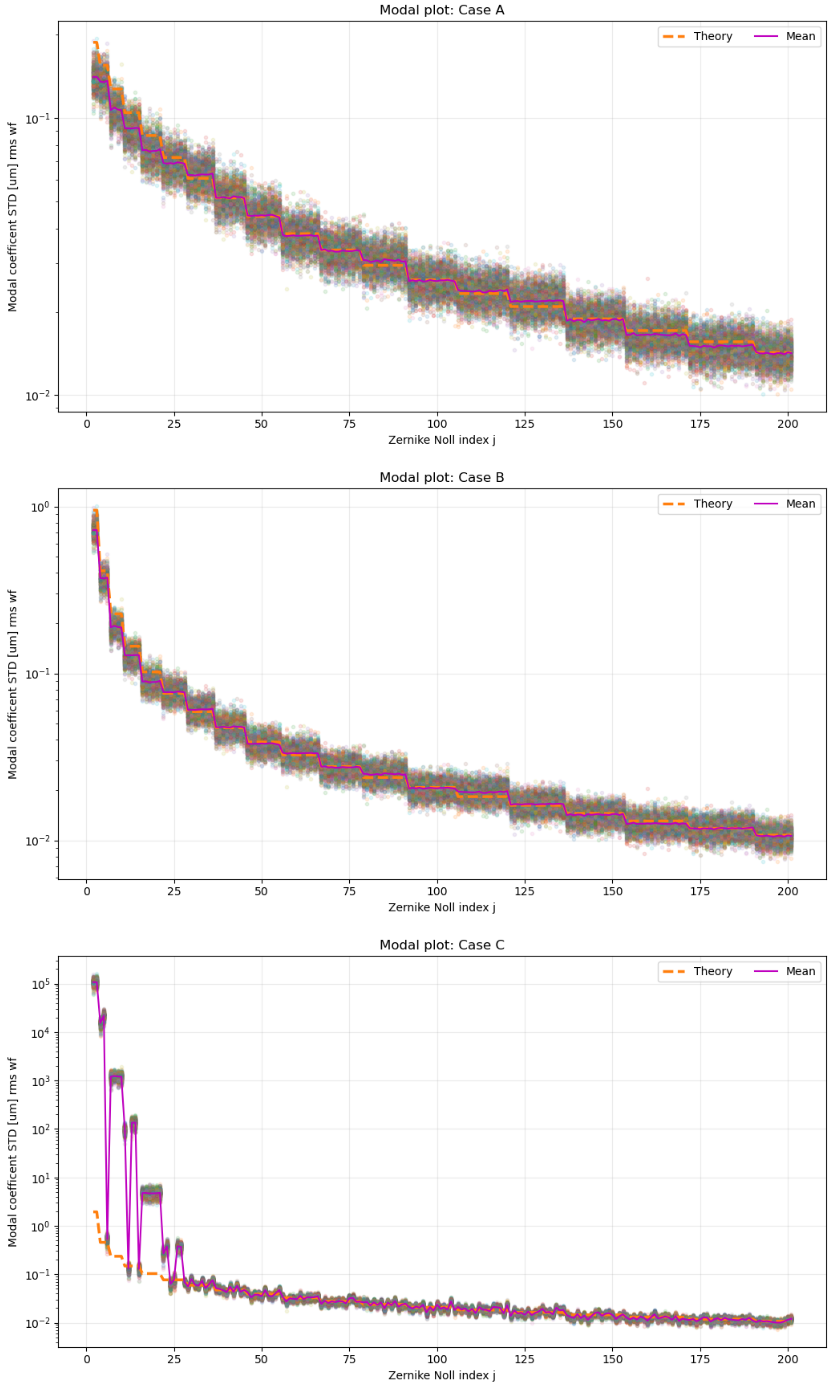

Figure 4.10. Modal plot from the simulated turbulent phase for the case reported in Table4.3. The dots are the decomposed coefficients' temporal standard deviation from each run, while solid and dashed lines are the per-mode mean (across data sets) and the theoretical standard deviation values, respectively. The case A and B shows a discrepancy of $\lesssim 6\%$, while assuming a Kolmogorov PSD model numerical errors occur in SPECULA generated phase screen: the low-order modes shows out-of-scale values of the order of fractions of meters.

4.3.2 Closed-loop on atmospheric turbulence

In the present discussion, we describe the tests performed and the outcome analysis from the simulated (hardware-in-the-loop) SCAO, which compensates for the atmospheric turbulence by means of the SLM-based testbed. To do so, we used a KL modal base of 200 modes on a circular pupil without any obstruction, and, by means of SPECULA, we numerically simulated and injected on the SLM's test-bench the propagated phase. The turbulent phase propagation is realised by considering an on-axis propagation of the turbulence on the telescope pupil of 8.2 m, an outer scale $L_0 = 25$ m, and a Fried parameter $r_0 = 15$ cm (at $\lambda_V = 500$ nm), which corresponds to a (good) seeing of $\epsilon \simeq 0.68$ arcsec. Since the test-bench has a different working wavelength and from Eq.(1.6), the rescaled Fried parameter at given λ is given by:

$$r_0(\lambda) \, = \, r_0(\lambda_V) \, (\lambda/\lambda_V)^{6/5} \, . \tag{4.13}$$

Thus, at $\lambda = 633$ nm, the Fried parameter is $r_0(\lambda = 633nm) = 20$ cm. As seen in Sec.2.4.1, the corresponding subaperture pitch d on the pupil plane of the adopted subaperture set (of $\sim$ 41 lenslet along the diameter) is $d = 8.2m/41 \approx 20\,cm$, which leads to wavefront undersampling and, consequently, WFS aliasing. Since the SHWFS spatial cut-off is $f_c \simeq 1/(2d)$ and in the we are in the regime for which $f_c\, L_0 \gg 1$ the Von Kármán phase PSD can be approximated by the Kolmogorov one over the spatial-frequency range that contributes to WFS aliasing. In particular, from Eq.(1.17) and Eq.(1.18), the ratio of the two PSD of the wavefront phase distortions is given by:

$$\frac{\Phi^{\mathrm{VK}}(f)}{\Phi^{\mathrm{K}}(f)} = \left(1 + \frac{1}{(f L_0)^2}\right)^{-11/6} ,$$

where $\Phi^{\mathrm{VK}}(f)$ and $\Phi^{\mathrm{K}}(f)$ are the Von Kármán and Kolmogorov PSD, respectively. So, at the cut-off frequency $f_c = 2.5\,m^{-1}$ and for $L_0 = 25\,m$, the ratio is equal to $\Phi^{\mathrm{VK}}(f_c)/\Phi^{\mathrm{K}}(f_c) \approx 0.9995$ and the relative difference is $\lesssim 0.05\%$. Thus, we neglected the outer scale correction since the aliasing is dominated at frequencies $f > f_c$, where the von Kármán and Kolmogorov spectra are virtually the same. Based on these considerations, we computed the expected error contribution due aliasing following [50]. The associated variance under the assumption of the Kolmogorov model is given by:

$$\sigma^2_{aliasing} \, = \, 0.08 \, (d/r_0)^{5/3} \, .$$

Thus, for $r_0 = 20\,cm$ at 633 nm, and $d = 20$cm, we expected an error contribution due to the aliasing of ~ 30 nm rms wf.

The closed-loop is made of 1000 iterations with a time step of 1 ms. We set a delay between the sensing and the actuation of the simulated DM command of 2 iterative steps. The closed-loop control introduces a delay that filters the phase decorrelation, leading to a servo-lag error as seen in Sec.1.2.5. For a control integrator with a rejection bandwidth f_{3dB}, Eq.(1.69) can be written as [24]:

$$\sigma^2_{bw} \, = \, \left(\frac{f_g}{f_{3dB}}\right)^{5/3} \quad \text{with} \quad f_g \, = \, 0.426\, r_0/v \tag{4.14}$$

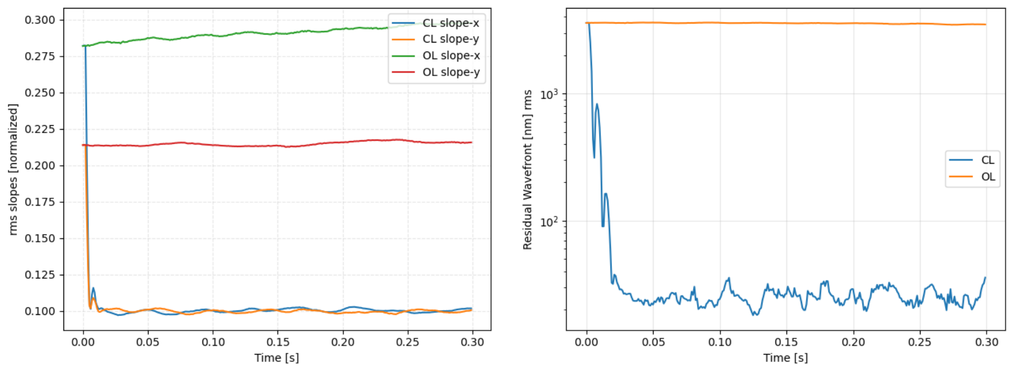

Figure 4.11. Temporal evolution of the root-mean-square of the measured slopes (on the left panel) and the residual wavefront (on the right panel). Open- and closed-loop quantities are shown. The simulated SCAO closed-loop converges. The residual wavefront on 200 modes is 25 nm rms wf.

where f_g is the Greenwood frequency, and v is the mean wind velocity. To get a first-order estimate of the expected bandwidth error of the simulated SCAO closed-loop, we assumed the empirical approximation for which $f_{3dB} \sim f_s/10 =$, where $f_s = 1/T_s$ is the sampling time of the SCAO simulation, namely T_s is the sampling time of the simulated WFS, in our case 1 ms. Thus, for $v = 5\,m/s$, $T_s = 1\,ms$, and $r_0 = 20\,cm$, we expected a servo-lag error σ_{bw} of ~ 16 nm rms wf.

Finally, we set an equal gain on the reconstructed modal command as seen in Eq.(4.10) of $g = 0.3$. This choice was empirically selected by performing preliminary SCAO closed-loop to infer the suitable gain value: stable closed-loops were achieved for $g \leq 0.3$, whereas larger gains led to instability and divergence of the loop under the simulated same operative conditions. For $g > 0.3$, the reconstructed modal commands exceeded the range required to guarantee linear response of the SHWFS. The consequent loss of flux in a fraction of subapertures reduced the slopes estimation reliability and increased measurement noise. As a result, the control progressively reconstructs larger commands, driving the integrator into a positive-feedback instability and, thus, resulting in a loop divergence.

Before closing the loop, we performed open-loops with the same conditions to compare and estimate the performance of the correction. It's worth noting that the static components of the optical bench seen in Sec.3.3.1 are included in the loops.

Figure 4.11 shows the temporal evolution of the residual wavefront measured on the 200 modes and the root-mean-square of the measured slopes from the SHWFS of the testbench. The loop converged in ~ 20 steps and both the residual wavefront and slopes rms remained stable. At convergence, the residual wavefront is of 25 nm rms on the reconstructed 200 modes.

To quantify the temporal variability of the SCAO control and the turbulence evolution, we computed the open- and closed-loop temporal standard deviation of the reconstructed modal coefficients. In particular, the closed-loop temporal variability is computed on the convergence regime of the loop. Figure 4.12 shows the temporal standard deviations of open and closed-loop reconstructed coefficients. This plot shows how the SCAO system is capable of rejecting each mode.

To quantify the total rejection on the 200 reconstructed modes, we computed

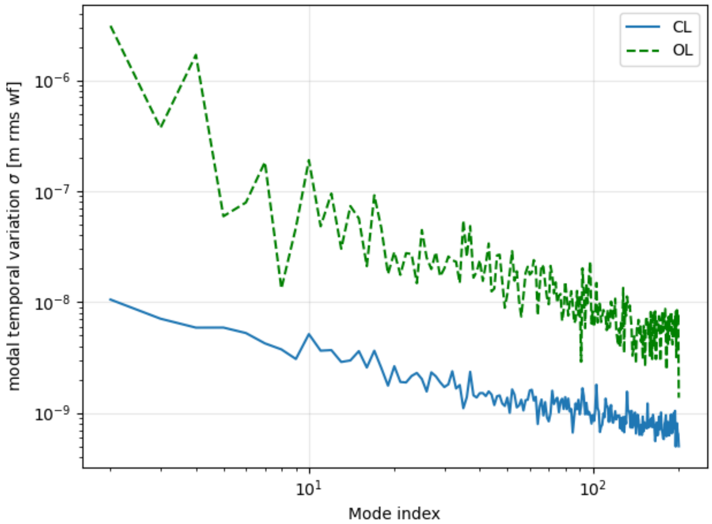

Figure 4.12. Modal plot of the SCAO loop. It shows the temporal variability of the open (OL) and closed (CL) loop reconstruction coefficient. It is computed as the standard deviation of reconstructed coefficients. The control rejects the injected turbulence.

the total rejection ratio as follows:

$$R_{var} = \frac{\sigma^2_{OL}}{\sigma^2_{CL}}\,, \tag{4.15}$$

where the σ^2_{OL} and σ^2_{CL} are the sum square of the reconstructed coefficient in open and closed-loop, respectively. The outcome analysis shows that the overall RMS, R_{RMS}, of the corrected 200 modes is reduced of a factor $R_{RMS} = \sqrt{R_{var}} = \sqrt{19319} \approx 140$.

To compute the temporal evolution of the wavefront error over the simulated loop, we decomposed the residual wavefront due to the compensation of the turbulence. To do so, from the applied wavefront maps on the SLM, we removed the compensation of the static aberrations of the bench. Since the simulated DM will apply the commands to compensate for both turbulent and static aberrations of the bench, reproducing a wavefront map given by:

$$\varphi_{DM} = \tilde{\varphi}_{turb} + \tilde{\varphi}_{static}\,, \tag{4.16}$$

where the $\tilde{\varphi}$ is the required wavefront computed to compensate for the turbulence, $\tilde{\varphi}_{turb}$, or the static aberration of the bench, $\tilde{\varphi}_{static}$.

At each time, the loop iteration on the SLM reproduced the following wavefront:

$$\varphi^t_{SLM} = \varphi^t_{turb} + \varphi^{t-1}_{DM}\,. \tag{4.17}$$

Thus, the residual wavefront map at a given time step t, due to the only effects of the turbulence and the compensation, is given by:

$$\varphi^t_{res} = \varphi^t_{turb} + \tilde{\varphi}_{turb} = \varphi^t_{SLM} - \tilde{\varphi}_{static}\,. \tag{4.18}$$

Finally, the residual wavefront map due to the turbulence and the DM compensation is obtained by its projection onto a synthetic reconstruction matrix to reconstruct

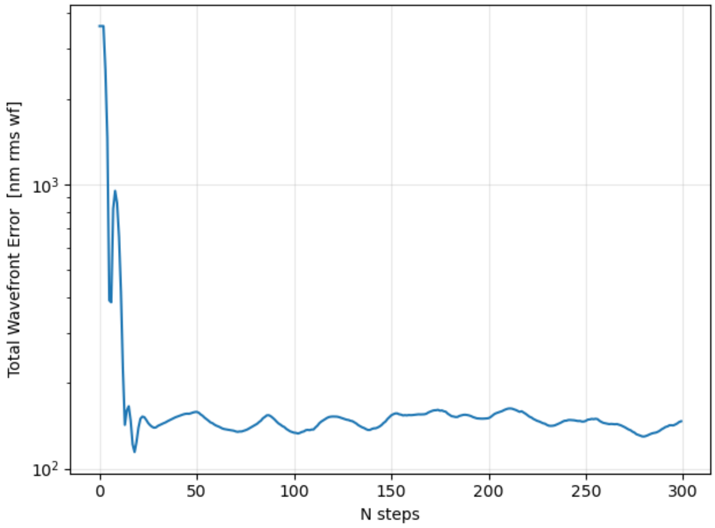

Figure 4.13. Wavefront error evolution on the simulated SCAO loop. At convergence the WFE has a mean value of 146 nm rms wf.

the associated modal coefficients $\boldsymbol{c}^t_{res} = R\,\varphi^t_{res}$. Finally, the wavefront error is computed as the root-sum-squared of the coefficients in $\boldsymbol{c}^t_{res}$. Figure 4.13 shows the estimated wavefront error at each step of the loop. At convergence the wavefront error is $WFE = 146$ nm rms.

We modelled the residual wavefront outside the controlled modal base ("modal truncation error") by integrating the von Kármán phase PSD beyond an equivalent spatial cut-off $f_c = 1/(2d_{eq})$, where $d_{eq} = D/\sqrt{N}$ where N is the actuator equivalent pitch matching N controlled modes on the pupil area. For the parameters used to simulate the SCAO closed-loop, we expect a modal truncation error of 128 nm rms wf. Thus, the closed-loop shows a residual error due to the other sources of error is $\sqrt{146^2 - 25^2 - 128^2} \approx 66$nm rms wf. However, the estimation of the modal truncation error considers the phase corrector as an ideal high-pass band filter, providing perfect compensation below the f_c and none above. However, real DMs on defined grid are characterised by a non-ideal spatial transfer function $H(\boldsymbol{f})$: the spatial transfer function is not exactly 1 below the cut-off frequency and it doesn't drop instantly to zero above f_c, leaving some leakage. Furthermore due to the DM's geometry and IFS shapes, there is a loss of efficiency on the compensation as we get close to f_c. Thus the overall effect is an increase in modal truncation the estimated variance and is given by:

$$\sigma^2 = \int_{\mathbb{R}^2} |\,1 - H(\boldsymbol{f})\,|^2\ \Phi_\phi(\boldsymbol{f})\,\mathrm{d}^2\boldsymbol{f} \tag{4.19}$$

where, $\Phi_\phi(f)$ is defined in Eq.(1.18). If we consider from [89] an increment on the estimated modal truncation variance due to the DM's IFS of 9%, this leads to a residual of ≈ 33 nm rms wf.

To conclude, we verified the quality of the image correction by checking the SR evolution over the loop. Using the Marechal approximation, the expected SR at $\lambda = 500\,nm$ for a wavefront error of 146 nm is $\sim 3.5\%$, and when it is rescaled to

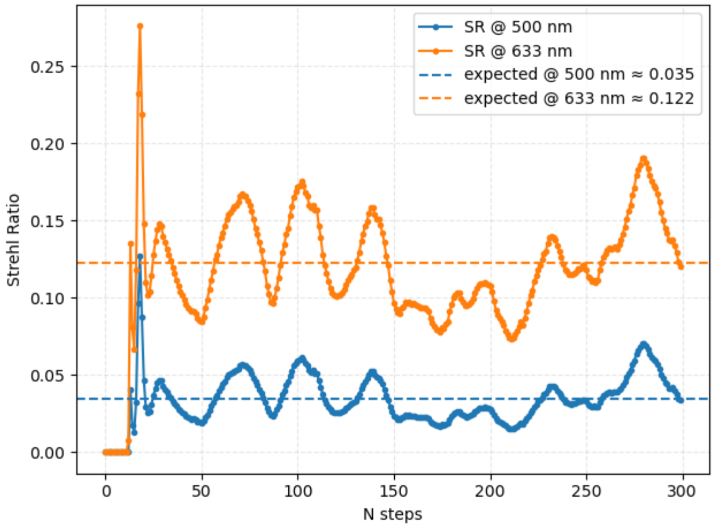

Figure 4.14. Estimated SR as a function of the time step. In blue dotted curve the SR actually measured on the bench at the working wavelength of 633nm, while the orange dotted curve is computed by rescaling the measured SR to 500nm. At convergence, the estimated SRs are consistent with the expected ones (dashed lines). At the first steps of the loop, the SR values are apparent equal to zero due to the choice of the ROI in which the SR is evaluated. This was optimised for the expected position of the closed-loop PSF in the science camera.

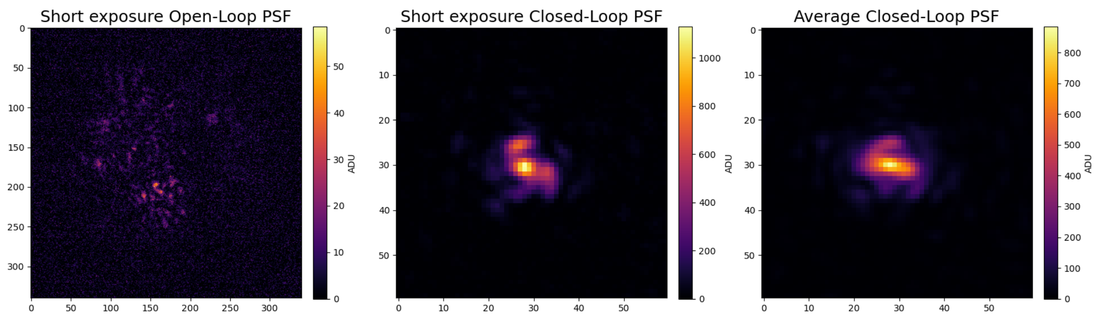

Figure 4.15. Examples of acquired frame from the science camera in SCAO loop simulation executed on the test bench. On the left panel, a frame of a short exposure seeing-limited PSF acquired in a SCAO open-loop run, with a measured SR of $\sim 4\%$. On the middle panel, a frame of a short exposure compensated PSF acquired in the SCAO closed-loop run, with a measured SR of $\sim 16\%$. On the right panel, average closed-loop PSF of the same closed-loop run, computed as the mean of the compensated PSFs in the loop convergence regime, corresponding to a measured SR of $\sim 13\%$.

the working wavelength at 633 nm is of $\sim 12.2\%$. The outcome analysis are shown in Figure 4.14 and Figure 4.15. In particular, Figure 4.14 shows the measured and rescaled SR, respectively at 633 and 500 nm. It is worth noting that the SR values reported on the figure are equal to zero during the first iterations of the closed-loop. This is due to the fact that the PSF is initially seeing-limited and significantly tilted with respect to the ROI used for SR estimation. Since the ROI is centred at the expected closed-loop PSF position on the science camera and kept constant across the loop, a most fraction of the PSF energy fell outside the chosen ROI at the first iterations of the loop, leading to an apparent SR equal to zero. The outcome analysis showed that the measured SR are consistent with the expected values, showing fluctuations of $\sim 3\%$ and $\sim 1\%$ at 633 and 500 nm, respectively. Finally, Figure 4.15 provides a visual representation of the quality correction of the executed SCAO closed-loop, comparing the acquired PSF in seeing-limited (on the left panel of the latter figure) and AO-assisted conditions (on the remaining panels of the same figure). Although the closed-loop PSF remained far from the diffraction limit resolution, from the outcome analysis we concluded that the prototyped SCAO closed-loop converged, with measured SR values consistent with the expectations.

Chapter 5

Conclusions

The presented work was aimed at the development of test-bed that reduces complexity of a real Multi-Conjugate Adaptive Optics (MCAO) system, such as Multi-conjugate adaptive Optics Relay For ELT Observations (MORFEO), and still allows to assess the performance and critical aspects of the MORFEO reconstruction and control algorithms. This test facility, in collaboration with the Adaptive Optics (AO) group of the Arcetri Astrophysical Observatory, is part of the MORFEO work packages. As discussed so far, the high spatial resolution, with thousands of pixels, makes Spatial Light Modulators (SLMs) a promising phase modulator for reproducing atmospheric turbulence and compensation on Extremely Large Telescopes' (ELTs) complex pupil. This makes them valuable tools for testing and characterisation of upcoming AO facilities for ELTs in laboratory test-beds. However, such devices are known to have several limitations compared to ordinary deformable mirrors (DMs). In this context, we presented the efforts of the development and characterisation of an SLM-based SCAO test-bench, decomposed and sequentially executed SCAO loop to reproduce the real MCAO system. By prototyping the coupling between the hardware and the end-to-end simulations, this project is aimed at testing the MORFEO's reconstruction and control algorithms.

As seen in Chapter 2, we developed a control software and interface for the SLM, from the SDK provided by the manufacturer. This has been integrated to PLICO, a Python framework used for controlling the commonly used devices in optical laboratories, with a specific application to adaptive optics facilities. The developed software allows to apply on the SLM display any user-defined image, to reproduce the wanted aberration on the bench. Furthermore, we developed a dedicated software that interfaces the test-bench hardware to SPECULA, a Python package dedicated to AO simulations. This constructed processing object put the fundamentals of hybrid AO simulations, which couples real AO hardware with end-to-end AO simulations, giving rise to a dedicated package called SPECULA-Lab. All these packages are designed in a Python environment and are available on GitHub. In addition, we showed how wide field AO test facilities can be realised by breaking down the complex MCAO's systems, still assessing the critical aspects in reconstruction and control algorithms. Without using multiple Wavefront Sensors (WFSs) and a phase corrector to mimic the real simultaneous probing and compensation of the turbulent volume, we decomposed the MCAO process into a sequentially executed SCAO loop.

In particular, the phase residual in each direction of the guide star in numerically computed and applied one per time on the SLM. For each applied residual phase a single Shack Hartmann WFS (SHWFS) is used to measure the corresponding slopes. Once probed the residual phase in all the guide star directions, the measured slopes are used to numerically compute the DMs required commands for optimising the compensation. Finally, to test the quality of the correction, the updated residual phase propagated along the science target direction is applied on the SLM and the resulting Strehl Ratio (SR) is computed by means of the Point Spread Function (PSF) acquired by the test-bench science camera. The whole process is repeated iteratively by shifting the turbulent layers previously simulated, in order to take into account the temporal evolution effects between successive iterations of the control loop. This sequentially executed MCAO relies on SPECULA for the numerical computation aspect of the atmospheric turbulence and its compensation, while PLICO is used to control the hardware in the loop.

As seen in Chapter 3, the MORFEO's test facility for the test and validation of the reconstruction and control algorithms has been designed and integrated. The key elements of the testing setup has been deeply characterised, establishing a solid experimental reference needed for the testing control strategies and closed-loop simulations, and the hardware-in-the-loop control optimisation. Greater attention has been placed on the characterisation of SLM, which is a promising phase modulator to reproduce phase residuals on ELTs' complex pupil thanks to its resolution. However, such devices are known to produce side effects compared to ordinary DMs. We quantified the effects of the pixelated structure and phase quantisation of such devices. The effect of reproducing a given aberration on 8-bit phase level contributes to a loss in SR less than $\lesssim 0.005\%$. The pixelated structure of the SLM acts like a classical diffraction grating, which compared to ordinary DMs, is responsible of a loss of power on the reflected beam of the $\simeq 8\%$, due to the pixel fill factor.

We showed that the SLM's reflected beam is characterised by a non-negligible fraction of light which prevents a full phase modulation. The result is an unmodulated spot in the specular reflection of the SLM, that pollutes the available field of view. Analysing the different contributions that may concur, the magnitude of the unmodulated spot is 4.5 ± 0.4 % of the total SLM reflected power. This unmodulated power, remains constant for the applied Tip-Tilt commands that span the available field of view. We measured the SLM response to commanded Tip-Tilt by checking the PSF displacement linearity. The outcome analysis showed that the SLM has a linear response with a relative error of $\lesssim 2\%$, which is mainly due to the fact that for high Tip-Tilt commands the PSF is affected by off-axis aberrations, biasing the estimation of the PSF centroid. Furthermore, we described one of the most critical aspect of the SLM, which deals with its complex modulation and high sensibility to calibration. We quantified the effects of any deviation from a precise 2π phase wrapping. These effects have been quantified by studying how a Tilt phase is reproduced by the SLM. The outcome analysis showed that for phase wrapping values $\phi_w < 2\pi$, the commanded Tilt behaves like a stepped phase grating. Thus, diffractive spots may appear on the focal plane, scattering the light into the diffraction spots and polluting the available field of view. We saw that the separation of the diffractive orders is equal to the PSF displacement expected for the commanded Tilt. Furthermore, we analysed the effects of reproducing complex

ELT-pupils by means of a huge Tilt, applied in the SLM pixel area outside the pupil active area. The simulations showed that for a phase wrapping deviation from 2π of the order of 10%, the specular reflected beam by the SLM (the zero-diffraction order) is characterised by an efficiency loss that remains less than 3% for all the explored range of applied Tilt. Considering the presence of the physical aperture stop upon the SLM, the area of the simulated complex pupil is negligible compared to the active pupil area where phase aberrations are displayed. Finally, we quantified another feature which distinguishes the SLM compared to ordinary DM. We analysed the SLM's temporal response to the applied command. The outcome analysis showed that the liquid crystal response time is 1.80 ± 0.07 ms and its compatible to the one provided by the manufacturer. In addition, we measured the command settling time, which is of 2.74 ± 0.09 ms.

After the SLM analysis, we characterised the SHWFS and the effects of the adopted centroid algorithm for the slopes estimation. We observed that the WFS has a loss of gain of 20%. However, as we used measured control matrices there is no need to compensate in the reconstruction process. In addition, we quantified the slopes to reconstructed modal command noise for the chosen exposure time of 7.0 ± 0.8 nm rms wf.

Then, we characterised the static aberrations of the bench. Once the bench is integrated and aligned, the measured wavefront error, after Tip-Tilt-Defocus modes filtering, is of 134 ± 3nm rms wf. The outcome analysis shown that the integrated bench and its static aberrations are stable within a temporal variability of $\sim 2\%$.

Finally, in Chapter 4, we described the test performed to prototype and execute hardware-in-the-loop simulations. At this stage of the MORFEO work package, we were not interested to reproduce the same ELT's turbulence and MORFEO's WFS sampling and compensation conditions on the test bench. Instead, the work was aimed at the development and characterisation of the hardware and software support for the SLM-based testbech, prototyping the coupling between hardware to end-to-end simulations in AO loops. Thus, although the employed SHWFS's subaperture set of $\sim$ 41 lenslet along the diameter undersamples the turbulent wavefront in VLT- and ELT-like pupils, and the simulated DM has 41×41 actuators, the SCAO closed-loops were restricted to good-seeing conditions in a pupil of 8.2 m at the working wavelength of 633 nm. Before closing the SCAO loop on the turbulence, we measured and tested the control matrices calibrations using both a Zernike and Karhunen-Loève (KL) modal base. As expected, the Zernike modal base has shown constraints in wavefront reconstruction, particularly in SCAO closed-loop with atmospheric turbulence. This is due to the fact that the high-order Zernike modes show steep local gradient that the SHWFS is not capable to sense due its sampling and which induces to nonlinear response on the WFS. Noting that, we used a KL modal base of 200 modes, computed from numerically computed zonal influence function of 41×41 actuators on a circular pupil of 8 m. Finally, we performed closed-loop simulating the atmospheric turbulence on an 8.2 m telescope with $r_0(500\,\mathrm{nm}) = 15$cm. The SLM-based SCAO was capable to reproduce the loop and to converge, providing measured SR compatible with the expected ones. Particularly, we measured a wavefront error of $WFE = 146$ nm rms wf, and a residual of 25 nm on a base of 200 KL modes, at convergence of the loop. From the inferred WFE, we expected a SR at 500 nm of $\sim 3.5\%$, that when it is rescaled to the working wavelength of the test bench, is equal to $\sim 12.2\%$. Thus, in the prototyped SCAO closed-loop, we measured SR values consistent with the expectations, with fluctuations of $\sim 3\%$ and $\sim 1\%$ at 633 nm and 500 nm, respectively.

To conclude, the first runs of hybrid AO simulation that couples hardware alongside end-to-end simulations have shown promising results. This work represents the first and necessary efforts in prototyping hybrid AO simulations: this approach of using hardware alongside simulation enables more reliable system validation by addressing problems close to those in the real system like WFS noise, alignment, and sensor imperfections, providing more reliable performance validation compared to pure end-to-end simulations. Even though further efforts must be made to complete and validate this hybrid approach, the developed SLM-based testbed is still a promising and useful test facility to inspect all the critical aspects of MORFEO's. Furthermore, it can be used to prototype and characterise the WFSs planned for MORFEO, before going on sky and to test novel techniques foreseen of the next generation of AO modules, such as the so-called *super-resolution* [64]. This technique combines slightly shifted WFS measurements (e.g. through micro-dithering of the WFS) to reconstruct spatial components beyond the former sampling of the single fixed subaperture, decoupling its size from the effective resolution and mitigating losses due to edge vignetting. In other words, super-resolution reduces the aliasing error, improving the reconstruction at higher frequencies due to the finer sampling of the wavefront.

Beyond the development of the SLM-based test-bed presented in this manuscript, I have also contributed to several related activities and projects in the broader context of AO for ELTs. These works reflect my collaborative efforts with the AO group in Arcetri and the one at the Laboratoire d'Astrophysique de Marseille, and highlight the importance of developing test devices for the next generation of AO facilities for ELTs, like MORFEO and HARMONI. A brief overview of these activities and the related publications is provided in Appendix D.

Appendix A

Defocus mode due to pixel/subaperture size

As discussed in Sec. 2.4.1, a mismatch between the detector's pixel size and the subaperture size of the SHWFS , results in an apparent Defocus reconstructed signal. In the present discussion, we described and quantified this effect linking the isotropic scaling error to reconstructed Defocus Zernike coefficient c_4. We assumed the Noll notation for the defocus mode:

$$W_4(\rho) = c_4\sqrt{3}\,(2\rho^2 - 1) \qquad \text{with } \rho = \frac{r}{R},$$

where W_4 is defined over a circular of radius R. Since the SHWFS measures the wavefront gradient, we computed the partial derivatives:

$$\frac{\partial W_4}{\partial x} = \frac{4\sqrt{3}\,c_4}{R^2}\,x, \qquad \frac{\partial W_4}{\partial y} = \frac{4\sqrt{3}\,c_4}{R^2}\,y\,.$$

The latter equations show that the gradient is a linear slope vector field in (x, y).

A mismatch between the assumed and the actual sampling (pixels per subaperture) produces a small linear drift of spot positions across the pupil. We defined $\delta_{\mathrm{px/SA}}$ be the incremental shift (in pixels) that is accumulated when moving by one subaperture. If we define Δx_{px} as the centroid shift in pixels, and p as the camera pixel pitch and f_{la} as the lenslet focal length, the slope is $s = \Delta x_{\mathrm{px}}\,p/f_{la}$. Thus, the linear slope field has a coefficient:

$$\alpha \;\equiv\; \frac{\partial s_x}{\partial x} \;=\; \frac{p}{f_{la}}\,\frac{\delta_{\mathrm{px/SA}}}{d_{\mathrm{step}}},$$

where d_{la} is the lenslet aperture.

Finally, equating the linear Defocus gradient to the measured linear slope gives the desired estimate:

$$c_4 \;=\; \frac{\alpha R^2}{4\sqrt{3}} \;=\; \frac{p\,R^2}{4\sqrt{3}\,f_{la}\,d_{la}}\,\delta_{\mathrm{px/SA}}\,.$$

If N_{actual} and N_0 are the actual and assumed pixels-per-subaperture, respectively, then we can write the incremental shift as follows:

$$\delta_{\mathrm{px/SA}} = N_{\mathrm{actual}} - N_0,$$

To conclude, for our SHWFS, considering the demagnification of the SLM pupil due to the relay of L2 and L3 lenses, and $N_0 = 26$ and $N_{\mathrm{actual}} = d_{la}/p$, we obtained a coefficient of $c_4 = 1.09 \pm 0.03\,\mu$m rms wf. The error computed coefficient is obtained from the error propagation considering only the error contribution of focal length and aperture size of the lenslet.

Appendix B

Behaviour of $\langle e^{j\phi} \rangle$

Hereafter are presented considerations about the mean complex of the phasor $e^{j\phi}$ discussed in Sec.3.1.3 as a function of the commanded phase $\phi(\xi, \eta)$:

$$\langle e^{j\phi} \rangle \;=\; \frac{1}{A_{act}} \iint_{A_{act}} e^{j\phi(\xi,\eta)}\; d\xi d\eta \;=\; \frac{1}{A_{act}} \iint_{\mathbb{R}^2} M(\xi,\eta)\; e^{j\phi(\xi,\eta)}\; d\xi d\eta \tag{B.1}$$

with $M = M(\xi, \eta) \in \{0, 1\}$ the pupil function, where $M = 1$ on the phase modulated area and $M = 0$ elsewhere. The following case is discussed:

(i) Tip-Tilt. For a commanded Tip-Tilt phase $\phi(\xi, \eta) = 2\pi(\nu_x\xi + \nu_y\eta)$, Eq(B.1) becomes the Fourier transform of the aperture:

$$\langle e^{j\phi} \rangle \;=\; \frac{1}{A_{\text{act}}} \iint_{A_{\text{act}}} e^{j2\pi(\nu_x\xi+\nu_y\eta)}\, d\xi d\eta \;=\; \frac{\mathcal{F}\{M(-\nu_x, -\nu_y)\}}{A_{act}}$$

If we consider real and symmetrical apertures $\mathcal{F}\{M\}$ is an even function. If we consider a rectangular aperture of size $D_x{\times}D_y$ or a circular one with diameter D:

$$\begin{aligned} \langle e^{j\phi} \rangle_{rect} &= \text{sinc}(\nu_x D_x)\ \text{sinc}(\nu_y D_y) \\ \langle e^{j\phi} \rangle_{circ} &= 2J_1(\pi\nu D)/(\pi\nu D) \end{aligned} \tag{B.2}$$

where $\nu = \sqrt{\nu_x^2 + \nu_y^2}$ and $\text{sinc}(x) = \sin(\pi x)/(\pi x)$. So, with only few cycles $N = \nu D \gtrsim 3 - 4$ over the aperture, $\langle e^{j\phi} \rangle$ is about few percent $\sim 0.05 - 0.1$. Thus for steep Tip-Tilts the mean complex phasor on the active area approaches to 0.

Appendix C

Strehl Ratio

As discussed in Sec.1.2.6 and Sec.4.2.1, the image quality and correction performance of any AO system are mainly quantified through the Strehl Ratio (SR) metric:

$$\mathrm{SR} \;=\; \frac{I_{\mathrm{peak}}^{\mathrm{meas}}}{I_{\mathrm{peak}}^{\mathrm{DL}}}\,, \tag{C.1}$$

where $I_{\mathrm{peak}}^{\mathrm{meas}}$ and $I_{\mathrm{peak}}^{\mathrm{DL}}$ are the peak values of the measured and diffraction-limited (DL) PSF, respectively, evaluated on the same sampling and over the same region of interest (ROI). Hereafter, we describe the adopted method and quantities used to estimate the SR and the associated error from the measured PSF in a given ROI. The following discussion assumes that the background is carefully subtracted from the acquired frame.

SR estimation:

The diffraction-limited PSF is numerically computed from a circular pupil, where a flat wavefront is propagated to the focal plane according to Eq.(3.7) with a 2D Fast-Fourier Transform (FFT). Before the FFT, the electric field is zero-padded. This operation allows to define the sampling of the Fourier plane without changing the optical resolution. Indeed, the pixels in the Fourier plane become smaller in angular (or linear) units while the field of view remains the same. This allows to crop the diffraction-limited PSF in a sub-frame that matches the ROI of the measured PSF in size and sampling. To reduce pixel-grid bias in the DL peak estimate, a 2D Airy model is fitted on the simulated PSF, and the inferred maximum is taken as the DL peak, $I_{\mathrm{peak}}^{\mathrm{DL}}$.

The DL PSF is then normalized to the measured flux in the acquired frame, by computing the total counts in the measured ROI and scaling the DL PSF so that the total flux in an equally centred, same-size ROI is equal to the measured one. This normalization ensures that the comparison is insensitive to exposure time or throughput fluctuations and depends only on PSF sharpness.

Particularly, we define

$$I_{tot}^{DL} \;=\; \sum_{(x,y)\in\mathrm{ROI}} I(x,y) \qquad \text{and} \qquad I_{peak}^{DL} \;=\; \max_{(x,y)\in\mathrm{ROI}} I(x,y)\,,$$

the total flux and the intensity peak of the DL PSF $I(x, y)$ respectively, both computed numerically in arbitrary units. For a given measured PSF, $I_m(x, y)$ (in units of ADU), defined in a square ROI, we denote:

$$A_{\mathrm{ROI}} = \sum_{(x,y)\in\mathrm{ROI}} I_m(x, y) \qquad \text{and} \qquad A_p = \max_{(x,y)\in\mathrm{ROI}} I_m(x, y)$$

as the measured total flux and intensity peak respectively, both computed in the ROI of the acquired frame. In practice, A_p is obtained with a sub-pixel 2D quadratic fit on a small patch (e.g., 3×3) centred on the brightest pixel to mitigate grid quantisation. After normalizing the DL PSF to have the same total ROI flux as the one in the measured ROI, the expected DL peak in ADU at equal flux is given by:

$$I^{DL}_{peak}[ADU] = \beta\, A_{\mathrm{ROI}} \qquad \text{with} \qquad \beta = \frac{I^{DL}_{peak}}{I^{DL}_{tot}} .$$

Finally, by writing Eq.(C.1) in units of ADU, the estimated SR is defined as follows:

$$\mathrm{SR} = \frac{A_p}{\beta\, A_{\mathrm{ROI}}} . \tag{C.2}$$

SR error modelling:

The associated error σ_{SR} is estimated from a first-order error propagation of Eq.(C.2). Assuming as the main source of noise the Poisson photon noise and the Gaussian read-out noise, the variance related to the measured peak A_p and the measured flux A_{ROI} are respectively described as follows:

$$\begin{aligned} \sigma^2_{A_p} &= \frac{A_p}{g} + r^2 \\ \sigma^2_{A_{\mathrm{ROI}}} &= \frac{A_{\mathrm{ROI}}}{g} + N_{\mathrm{ROI}}\, r^2 \end{aligned} \tag{C.3}$$

where g is the gain of the camera (expressed in units of e^-/ADU), r the RON (in ADU units), and N_{ROI} the number of pixels in the ROI. Since the ROI sum contains the peak ($A_{\mathrm{ROI}} = A_p + \sum_{q\neq\mathrm{peak}} I_q$), and the remaining pixels are independent from the peak, the covariance between the measured peak and flux is given by:

$$\mathrm{Cov}(A_p, A_{\mathrm{ROI}}) = \sigma_{A_p, A_{\mathrm{ROI}}} = \sigma^2_{A_p} \tag{C.4}$$

Thus, assuming β as known, the variance on the SR is given by:

$$\sigma^2_{\mathrm{SR}} = \left(\frac{\partial \mathrm{SR}}{\partial A_p}\right)^2 \sigma^2_{A_p} + \left(\frac{\partial \mathrm{SR}}{\partial A_{\mathrm{ROI}}}\right)^2 \sigma^2_{A_{\mathrm{ROI}}} + 2\, \frac{\partial \mathrm{SR}}{\partial A_p} \frac{\partial \mathrm{SR}}{\partial A_{\mathrm{ROI}}}\, \sigma_{A_p, A_{\mathrm{ROI}}} . \tag{C.5}$$

Finally, by replacing the variances from Eq.(C.5) and the partial derivatives:

$$\frac{\partial \mathrm{SR}}{\partial A_p} = \frac{1}{\beta A_{\mathrm{ROI}}}, \qquad \frac{\partial \mathrm{SR}}{\partial A_{\mathrm{ROI}}} = -\frac{A_p}{\beta A^2_{\mathrm{ROI}}} = -\frac{\mathrm{SR}}{A_{\mathrm{ROI}}},$$

in Eq.(C.5), the error on the estimated SR is given by:

$$\sigma_{\mathrm{SR}} = \mathrm{SR}\sqrt{\frac{\frac{A_p}{g}+r^2}{A_p^2}+\frac{\frac{A_{\mathrm{ROI}}}{g}+N_{\mathrm{ROI}}r^2}{A_{\mathrm{ROI}}^2}-2\,\frac{\frac{A_p}{g}+r^2}{A_p\,A_{\mathrm{ROI}}}}\,. \tag{C.6}$$

The negative covariance contribution reduces the SR uncertainty compared to the sum of the only peak and flux terms. Intuitively, any fluctuation that increases the peak will also increase the sum of the ROI, which will partially cancel out in the ratio.

As discussed in the present discussion, β is obtained once from a DL Airy fit and treated as known. Its modelling uncertainty (errors from aperture shape, quantisation, ROI truncation, among the others) is a systematic not included in (C.6). However, it can be bounded by re-fitting the DL under mild perturbations and analysing the spread/variations on β.

Thus, considering the systematic contribution of the peak-to-flux ratio of the simulated DL PSF in Eq.(C.5), with

$$\frac{\partial \mathrm{SR}}{\partial \beta} = -\frac{A_p}{\beta^2 A_{\mathrm{ROI}}} = -\frac{\mathrm{SR}}{\beta},$$

the final expression for the SR error is given by:

$$\sigma_{\mathrm{SR}} \;=\; \mathrm{SR}\sqrt{\frac{\frac{A_p}{g}+r^2}{A_p^2}+\frac{\frac{A_{\mathrm{ROI}}}{g}+N_{\mathrm{ROI}}r^2}{A_{\mathrm{ROI}}^2}-2\,\frac{\frac{A_p}{g}+r^2}{A_p\,A_{\mathrm{ROI}}}+\left(\frac{\sigma_\beta}{\beta}\right)^2}\,. \tag{C.7}$$

To quantify the relative error σ_β/β on the DL peak-to-flux ratio β induced by the tolerances and variations on the main optical parameters, we perform a Monte Carlo (MC) simulation [90]. The DL peak-to-flux ratio $\beta = \beta(\lambda,\, D,\, f)$ is mainly a function of the working wavelength λ, the pupil size D and the focal length of the objective lens (L2, in Figure 2.2) f. In the following analysis, we considered the camera and SLM pixel size (4.65 μm and 9.2 μm, respectively) as exact.

Parameter	**Nominal value (μ)**	**Uncertainty (σ)**	**Priors $\mathcal{P}$**
λ	632.8 nm	$\pm$ 0.2 nm	$\mathcal{N}(\mu,\sigma)$
D	10.028 mm	$\pm$ 0.003 mm	$\mathcal{U}(\mu \pm 4.6\ \mu\mathrm{m})$
f	250 mm	$\pm$ 2.5 mm	$\mathcal{N}(\mu,\sigma)$

Table C.1. Nominal optical parameters with associated 1σ uncertainties and adopted distribution for the Monte Carlo analysis. For D, the uncertainty corresponds to SLM sampling quantisation (pixel pitch $\Delta = 9.2\ \mu$m): a uniform half-width $\Delta/2 = 4.6\ \mu$m implies $\sigma_D = \Delta/\sqrt{12} \approx 3\ \mu$m.

Table C.1 describes the adopted priors on the explored parameters. The working wavelength and focal length are modelled as independent normal/Gaussian distribution $\mathcal{N}(\mu,\sigma)$ where μ and σ are the nominal and tolerance values provided by the manufacturer. Since the circular pupil is realised by loading on the SLM a huge Tilt outside the active phase modulation domain, the pupil diameter D is characterised by the SLM pixel quantisation and is therefore modelled as a symmetric uniform distribution $\mathcal{U}(D, \Delta/2)$ with half-width $\Delta = 9.2\ \mu$m. To note that although the the focal length is wavelength dependent, the assumption on f and λ as random variables is justified because the objective lens is an achromatic doublet and the laser source is highly monochromatic: this makes the residual chromatic drift negligible compared with the $\sim$1% mechanical tolerance; therefore λ and f are treated as independent parameters.

For each MC simulation, we compute N independent samples $(\lambda_k, D_k, f_k) \sim \mathcal{P}_\lambda \times \mathcal{P}_D \times \mathcal{P}_f$ from their priors. For each sample, the DL PSF and its peak–to–flux ratio β_k are computed:

$$\beta_k \ = \ \frac{I^{DL}_{peak}(\lambda_k, D_k, f_k)}{I^{DL}_{tot}(\lambda_k, D_k, f_k)} \, ,$$

keeping the same FFT padding and ROI sampling. Figure C.1 shows the dispersion of the inferred β_k values as a function of the explored parameters. As the occurrences of β show a Gaussian pattern, the final MC estimate $\hat{\sigma}_\beta$ of the uncertainty on β, is computed as the standard deviation of the samples $\{\beta_k\}$.

To evaluate the goodness of the simulations, we analysed the convergence by increasing the number of samples N until the relative change of $\hat{\sigma}_\beta$ between successive runs is below a chosen threshold of $\lesssim 1\%$. In addition, to ensure that sampling noise is negligible at the targeted precision, we tracked the MC standard error (i.e. sampling noise) [90] of the standard deviation $\hat{\sigma}_\beta$ between successive runs:

$$\mathrm{SE_{MC}}(\hat{\sigma}_\beta) \ \approx \ \frac{\hat{\sigma}_\beta}{\sqrt{2\,(N-1)}} \, .$$

With reference to Figure C.2, the MC simulations converged to a relative error on β, $\hat{\sigma}_\beta/\ \bar{\beta}$, of $\simeq 2\%$. This estimate is stable for N $\geq 5 \times 10^3$ samples, while the normalized MC sampling noise on $\hat{\sigma}_\beta$ is less than 1% at $N > 10^4$, thus negligible at outcome precision.

For a qualitative cross-check, we compute the one–at–a–time local sensitivity [91] of $\beta(x)$ around the nominal point $x_0 = (\lambda_0, D_0, f_0)$. To do so, we estimate the local sensitivity as a finite difference $\Delta\beta$ due the variation on a single parameter of $\pm\sigma_x$, while the other are fixed to the nominal value:

$$\left.\frac{|\Delta\beta|}{\beta_0}\right|_{\pm 1\sigma} \ = \ \frac{1}{2\beta_0}\Big(\left|\beta(x_0+\sigma_x) - \beta_0\right| + \left|\beta(x_0-\sigma_x) - \beta_0\right|\Big),$$

where $x = (\lambda,\ D,\ f)$ and $\beta_0 = \beta(x_0)$ is the nominal value, and $\sigma_x = \sigma_i\, \hat{e}_i$ for $i = 1, 2, 3$.

The diagram in Figure C.3 shows that the one–at–a–time sensitivities are $\simeq 0.15\%$ for λ and D, and $\simeq 1.92\%$ for f, showing that the focal length tolerance dominates the uncertainty on β. These estimates, for which $\sqrt{0.192^2 + 0.015^2 + 0.015^2} \approx 0.0193$, are consistent with the MC result. Thus, the non-linear and cross relations between parameters are negligible, and the error on β is dominated by the focal length f.

To conclude, from the MC simulation, we adopt $\frac{\sigma_\beta}{\beta} \ = \ 2\%$ to be combined in quadrature with the peak and flux measurement terms in the SR noise model as described in Eq. (C.7).

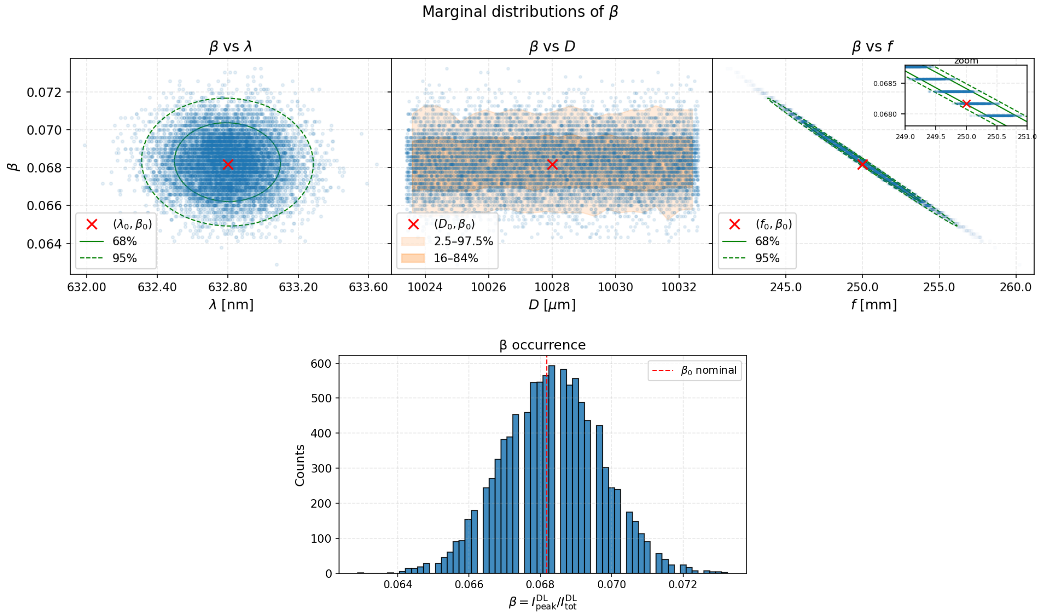

Figure C.1. Results from the MC simulation with a randomly generated seed and 10^4 samples. On the top panels, the marginal distributions of β, showing the MC samples of β for the explored parameters. The red marks show the nominal pair (x_0, β_0) in each panel. On the left and right panels, the green curves show 68% and 95% confidence levels obtained from the empirical mean and covariance of the bivariate sample (x, β).In the middle panel, the orange bands are non-parametric conditional quantile envelopes: the 16–84% (darker) and 2.5–97.5% (lighter) percentiles of β are shown. The right panel also includes a small inset to highlight the location of the nominal point relative to the confidence levels and the effect of the quantisation on the simulated DL PSF. Overall, β is nearly insensitive to D, only mildly affected by λ, and varies almost linearly with f, consistent with the sensitivity ranking. On the bottom panel, the distribution of the diffraction–limited peak–to–flux ratio $\beta = I^{\mathrm{DL}}_{\mathrm{peak}}/I^{\mathrm{DL}}_{\mathrm{tot}}$ obtained from the MC is shown. The red dashed line marks the nominal value β_0 computed at the nominal (λ_0, D_0, f_0). The distribution has a Gaussian pattern, where binning reveals the underlying discretisations induced by the fixed sampling of the DL PSF (FFT grid, zero–padding and ROI integration). For the run shown we obtain $\bar{\beta} \approx 6.83 \times 10^{-2}$, $\hat{\sigma}_\beta \approx 1.38 \times 10^{-3}$, with a relative error $\hat{\sigma}_\beta/\bar{\beta} \simeq 2\%$.

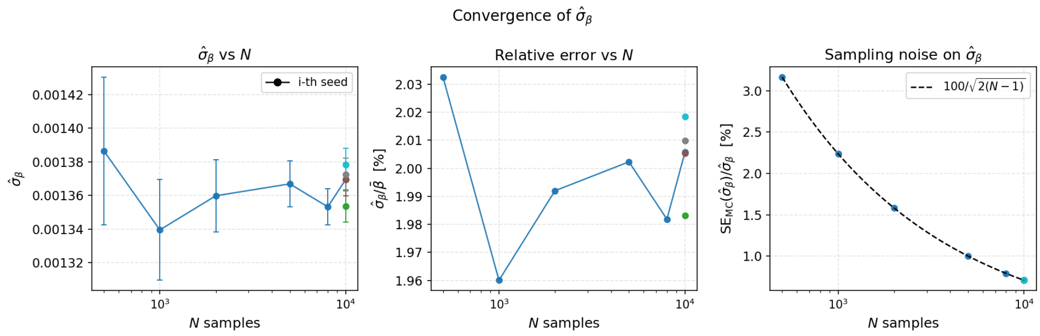

Figure C.2. Convergence of the estimated $\hat{\sigma}_\beta$ as a function of the number of samples and randomly generated seeds of the different MC runs. Each dot colour corresponds to a specific seed value, identical for all the plots. On the left, estimate of the standard deviation of β versus the number of Monte Carlo samples N. The error bars show the MC sampling error of the standard deviation estimator, $\mathrm{SE_{MC}}(\hat{\sigma}_\beta)$. In the middle: relative uncertainty $\hat{\sigma}_\beta/\bar{\beta}$ (in %) stabilizes at $\approx 2\%$. On the right: the estimated ratios $\mathrm{SE_{MC}}(\hat{\sigma}_\beta)/\hat{\sigma}_\beta$ (points) follow the theoretical $100/\sqrt{2(N-1)}$ dashed curve dashed. This confirms the expected $1/\sqrt{N}$ MC scaling and that $N \sim 10^4$ is enough for a stable estimate of $\hat{\sigma}_\beta$.

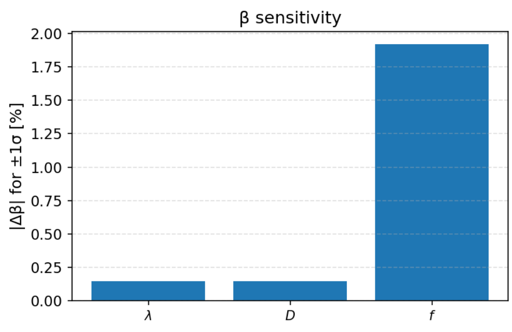

Figure C.3. One at a time local sensitivity of the DL peak–to–flux ratio β on λ, D, f parameters, evaluated around the nominal values. The bars report the relative change for a $\pm 1\sigma_x$ perturbation on a parameter while the others are fixed to the nominal value. The sensitivity is dominated by the focal length error.

Appendix D

Publications to highlight

The development of SLM-based test-bed for sequential simulation of wide field AO systems is an integral part of the MORFEO project. This test facility is carried out in collaboration with the AO group at the Arcetri Astrophysical Observatory, as primarily responsible for the design and implementation of MORFEO. The AO group in Arcetri is working with its counterparts at the Laboratoire d'Astrophysique de Marseille (LAM), who are responsible for developing the AO facility for the HARMONI [21], the integral field spectrograph on ELT. Despite their AO configurations, MORFEO and HARMONI are considered AO system twins due to their shared wavefront sensing hardware, both relying on SHWFSs.
During my research activity, I had the opportunity to take part in a collaboration of six months at LAM, working on the characterisation of the LGS-WFS prototype in the context of HARMONI's wavefront sensing [92, 93, 94]. This collaboration allowed me to work on the same hardware and software used to develop my test-bench in the MORFEO project, strengthening the links between these twin systems. During this period, I also had the chance to work on Provence Adaptive-optics PYramidRUnSystem (PAPYRUS) [95], an AO system installed at the Coudé focus of the T152 telescope (diameter of 1.52 m) at Observatoire de Haute-Provence (OHP). This AO system is used to test and characterise the hardware and software that will be used on HARMONI. PAPYRUS is the only operational on-sky AO facility designed specifically for early-career researchers in Europe. This was an unique opportunity to gain hands-on experience on an operational AO system, providing invaluable insights into the challenges of real AO systems.
During my PhD, I have contributed to the following publications that reflect both my contribution to MORFEO and broader collaboration in developing test devices for the next generation of AO systems for ELTs:

- *C. Selmi et al.*, (2023) [65]: we developed a software package to interface and control the SLM, which has been integrated into PLICO (Python Laboratory Instrumentation COntrol), available on GitHub [67]. This framework is designed to assist developers of instrument control applications, with a focus on interfacing with the most frequently utilized devices in AO laboratories.

- *E. Bellone de Grecis et al.*, (2023) [96]: we describe the aim of my PhD research project in the context of MORFEO reconstruction and control algorithms validation, describing the testing setup and the first results of the SLM characterisation.

- *M. Bonaglia et al.*, (2024) [97]: we show the current status of hardware and functionalities on the Natural GS WFSs of MORFEO, aimed to sense the lower order of atmospheric turbulence.

- *E. Bellone de Grecis et al.*, (2024) [83]: we present the results of the characterisation of the SLM used in MORFEO and HARMONI AO test-beds. The work is aimed to maximise the SLM phase modulation response to reproduce atmospheric phase screens and the relative compensation on ELT's complex pupil. We describe and quantify the magnitude of the spurious effects due to the pixelated structure and complex phase modulation of such device, which lead to diffractive effects and phase wrapping issues that could trick the WFS in the wavefront reconstruction.

- *R. Fétick et al.*, (2024) [98]: during my stay at LAM, I have contribute to the design and integration of the NIR science path of PAPYRUS. It consists of: a fibre injection module for VIPA [99] high resolution spectrograph; a second stage AO system using an infrared Zernike WFS [100] to prepare future extreme AO instruments for exoplanets detection; and finally, an imager to measure of the AO performances and to image extended objects. Figure D.1 shows the results of the correction after the commissioning.

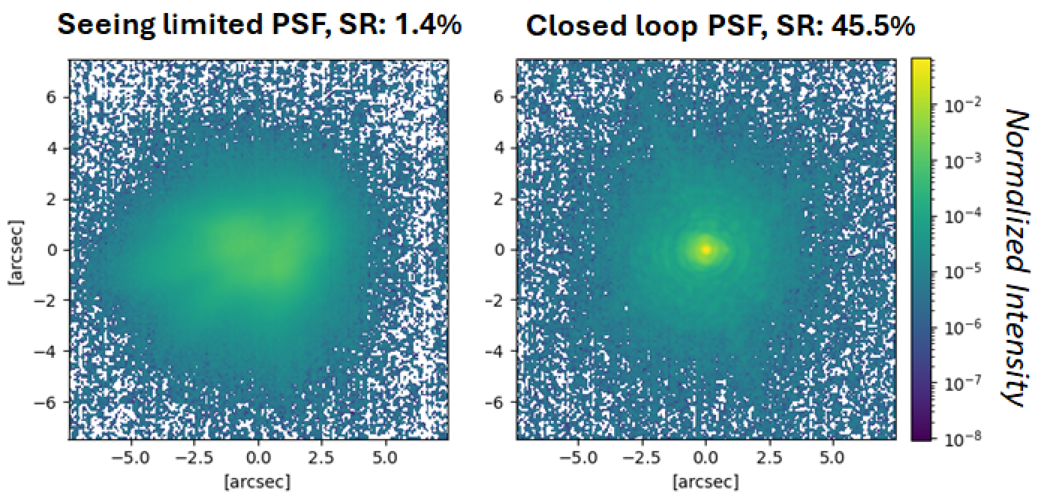

Figure D.1. Comparison between seeing-limited and closed-loop PSF on a single star, during the commissioning of the NIR imager on PAPYRUS. Courtesy of R. Fétick.

These works reflect my collaborative efforts with the AO group in Arcetri and the one at LAM, underlying the importance of developing test devices for the next generation of AO facilities on ELTs, like MORFEO and HARMONI.

Bibliography

[1] François Roddier. *Adaptive Optics in Astronomy.* 2004.

[2] Richard Davies and Markus Kasper. "Adaptive Optics for Astronomy". In: 50 (Sept. 2012), pp. 305–351. DOI: 10.1146/annurev-astro-081811-125447. arXiv: 1201.5741 [astro-ph.IM].

[3] François Rigaut and Benoit Neichel. "Multiconjugate Adaptive Optics for Astronomy". In: 56 (Sept. 2018), pp. 277–314. DOI: 10.1146/annurev-astro-091916-055320.

[4] Paolo Ciliegi et al. "MAORY: the adaptive optics module for the Extremely Large Telescope (ELT)". In: *Adaptive Optics Systems VII.* Ed. by Laura Schreiber, Dirk Schmidt, and Elise Vernet. Vol. 11448. Society of Photo-Optical Instrumentation Engineers (SPIE) Conference Series. Dec. 2020, 114480Y, 114480Y. DOI: 10.1117/12.2561754.

[5] Roberto Tamai et al. "The ESO's ELT construction progress". In: *Ground-based and Airborne Telescopes VIII.* Ed. by Heather K. Marshall, Jason Spyromilio, and Tomonori Usuda. Vol. 11445. Society of Photo-Optical Instrumentation Engineers (SPIE) Conference Series. Dec. 2020, 114451E, 114451E. DOI: 10.1117/12.2562828.

[6] Yann Clénet et al. "The MICADO first light imager for the ELT: overview of the SCAO module at its final design". In: *Adaptive Optics Systems VIII.* Ed. by Laura Schreiber, Dirk Schmidt, and Elise Vernet. Vol. 12185. Society of Photo-Optical Instrumentation Engineers (SPIE) Conference Series. Aug. 2022, 121854S, 121854S. DOI: 10.1117/12.2629856.

[7] L. Busoni. "MORFEO enters final design phase". In: Adaptive Optics for Extremely Large Telescopes 7th Edition. 2023.

[8] Thierry Fusco et al. "Multiconjugate adaptive optics: comparison of phase reconstruction approaches for large field of view". In: *Atmospheric Propagation, Adaptive Systems, and Laser Radar Technology for Remote Sensing.* Ed. by John D. Gonglewski et al. Vol. 4167. International Society for Optics and Photonics. SPIE, 2001, pp. 168–179. DOI: 10.1117/12.413820. URL: https://doi.org/10.1117/12.413820.

[9] Thierry Fusco et al. "Optimal wave-front reconstruction strategies for multi-conjugate adaptive optics". In: *Journal of the Optical Society of America A* 18.10 (Oct. 2001), pp. 2527–2538. DOI: 10.1364/JOSAA.18.002527.

[10] Brent L. Ellerbroek and Curtis R. Vogel. "Simulations of closed-loop wavefront reconstruction for multiconjugate adaptive optics on giant telescopes". In: *Astronomical Adaptive Optics Systems and Applications*. Ed. by Robert K. Tyson and Michael Lloyd-Hart. Vol. 5169. Society of Photo-Optical Instrumentation Engineers (SPIE) Conference Series. Dec. 2003, pp. 206–217. DOI: 10.1117/12.506580.

[11] François Rigaut et al. "Gemini multiconjugate adaptive optics system review - I. Design, trade-offs and integration". In: 437.3 (Jan. 2014), pp. 2361–2375. DOI: 10.1093/mnras/stt2054. arXiv: 1310.6199 [astro-ph.IM].

[12] Benoit Neichel, Thierry Fusco, and Jean-Marc Conan. "Tomographic reconstruction for wide-field adaptive optics systems: Fourier domain analysis and fundamental limitations". In: *J. Opt. Soc. Am. A* 26.1 (Jan. 2009), pp. 219–235. DOI: 10.1364/JOSAA.26.000219. URL: https://opg.optica.org/josaa/abstract.cfm?URI=josaa-26-1-219.

[13] Zichen Zhang, Zheng You, and Daping Chu. "Fundamentals of phase-only liquid crystal on silicon (LCOS) devices". In: *Light: Science and Applications* 3 (Oct. 2014). DOI: 10.1038/lsa.2014.94.

[14] H. W. Babcock. "THE POSSIBILITY OF COMPENSATING ASTRONOMICAL SEEING". In: *Publications of the Astronomical Society of the Pacific* 65.386 (Oct. 1953), p. 229. DOI: 10.1086/126606. URL: https://doi.org/10.1086/126606.

[15] F. Merkle et al. "Successful tests of adaptive optics." In: *The Messenger* 58 (Dec. 1989), pp. 1–4.

[16] J.-L. Beuzit et al. "SPHERE: the exoplanet imager for the Very Large Telescope". In: 631, A155 (Nov. 2019), A155. DOI: 10.1051/0004-6361/201935251. arXiv: 1902.04080 [astro-ph.IM].

[17] M. Tarenghi. "The VLT Site at Paranal: September 1994". In: *The Messenger* 78 (Dec. 1994), pp. 27–29.

[18] Meiji N. Nguyen et al. "GPI 2.0: optical designs for the upgrade of the Gemini Planet Imager coronagraphic system". In: *Advances in Optical and Mechanical Technologies for Telescopes and Instrumentation*. Vol. 12188. Society of Photo-Optical Instrumentation Engineers (SPIE) Conference Series. Aug. 2022, 121884K, 121884K. DOI: 10.1117/12.2630675. arXiv: 2209.12955 [astro-ph.IM].

[19] C. Matt Mountain, Fred C. Gillett, and Jim M. Oschmann. "Gemini 8-m telescopes". In: *Advanced Technology Optical/IR Telescopes VI*. Ed. by Larry M. Stepp. Vol. 3352. Society of Photo-Optical Instrumentation Engineers (SPIE) Conference Series. Aug. 1998, pp. 2–13. DOI: 10.1117/12.319254.

[20] Bernhard R. Brandl et al. "Final design and status of the Mid-IR ELT Imager and Spectrograph, METIS". In: *Ground-based and Airborne Instrumentation for Astronomy X*. Ed. by Julia J. Bryant, Kentaro Motohara, and Joël R. D. Vernet. Vol. 13096. International Society for Optics and Photonics. SPIE, 2024, p. 1309612. DOI: 10.1117/12.3018975. URL: https://doi.org/10.1117/12.3018975.

[21] Niranjan A. Thatte et al. “HARMONI at ELT: overview of the capabilities and expected performance of the ELT’s first light, adaptive optics assisted integral field spectrograph.” In: *Ground-based and Airborne Instrumentation for Astronomy IX*. Ed. by Christopher J. Evans, Julia J. Bryant, and Kentaro Motohara. Vol. 12184. Society of Photo-Optical Instrumentation Engineers (SPIE) Conference Series. Aug. 2022, 1218420, p. 1218420. DOI: 10.1117/12.2628834.

[22] Valerian Ilich Tatarskii. *Wave Propagation in Turbulent Medium*. 1961.

[23] John W. Hardy. *Adaptive Optics for Astronomical Telescopes*. 1998.

[24] Francois Roddier. *Adaptive optics in astronomy*. 1999.

[25] E. Masciadri et al. “Optical turbulence vertical distribution with standard and high resolution at Mt Graham”. In: 404.1 (May 2010), pp. 144–158. DOI: 10.1111/j.1365-2966.2010.16313.x. arXiv: 1001.1304 [astro-ph.IM].

[26] Joseph W. Goodman. *Statistical Optics*. 2000.

[27] Andrey Nikolaevich Kolmogorov. “Dissipation of Energy in Locally Isotropic Turbulence”. In: *Akademiia Nauk SSSR Doklady* 32 (Apr. 1941), p. 16.

[28] Vasudevan Lakshminarayanan and Andre Fleck. “Zernike polynomials: A guide”. In: *Journal of Modern Optics - J MOD OPTIC* 58 (Apr. 2011), pp. 1678–1678. DOI: 10.1080/09500340.2011.633763.

[29] Robert C. Cannon. “Optimal bases for wave-front simulation and reconstruction on annular apertures”. In: *J. Opt. Soc. Am. A* 13.4 (Apr. 1996), pp. 862–867. DOI: 10.1364/JOSAA.13.000862. URL: https://opg.optica.org/josaa/abstract.cfm?URI=josaa-13-4-862.

[30] Noah Schwartz et al. “Sensing and control of segmented mirrors with a pyramid wavefront sensor in the presence of spiders”. In: *arXiv e-prints*, arXiv:1809.08839 (Sept. 2018), arXiv:1809.08839. DOI: 10.48550/arXiv.1809.08839. arXiv: 1809.08839 [astro-ph.IM].

[31] R. J. Noll. “Zernike polynomials and atmospheric turbulence.” In: *Journal of the Optical Society of America (1917-1983)* 66 (Mar. 1976), pp. 207–211. DOI: 10.1364/JOSA.66.000207.

[32] J. Y. Wang and J. K. Markey. “Modal compensation of atmospheric turbulence phase distortion.” In: *Journal of the Optical Society of America (1917-1983)* 68 (Jan. 1978), pp. 78–87. DOI: 10.1364/JOSA.68.000078.

[33] J.-M. Conan, G. Rousset, and P.-Y. Madec. “Wave-front temporal spectra in high-resolution imaging through turbulence.” In: *Journal of the Optical Society of America A* 12.7 (July 1995), pp. 1559–1570. DOI: 10.1364/JOSAA.12.001559.

[34] F. Roddier et al. “One-dimensional spectra of turbulence-induced Zernike aberrations: time-delay and isoplanicity error in partial adaptive compensation”. In: *Journal of the Optical Society of America A* 10.5 (May 1993), pp. 957–965. DOI: 10.1364/JOSAA.10.000957.

[35] B. L. Ellerbroek and D. W. Tyler. "Adaptive Optics Sky Coverage Calculations for the Gemini-North Telescope". In: 110.744 (Feb. 1998), pp. 165–185. DOI: 10.1086/316120.

[36] R. Foy and A. Labeyrie. "Feasibility of adaptive telescope with laser probe". In: 152.2 (Nov. 1985), pp. L29–L31.

[37] Ronald R. Parenti and Richard J. Sasiela. "Laser-guide-star systems for astronomical applications". In: *J. Opt. Soc. Am. A* 11.1 (Jan. 1994), pp. 288–309. DOI: 10.1364/JOSAA.11.000288. URL: https://opg.optica.org/josaa/abstract.cfm?URI=josaa-11-1-288.

[38] F. Rigaut and E. Gendron. "Laser guide star in adaptive optics: the tilt determination problem." In: 261 (Aug. 1992), pp. 677–684.

[39] R. V. Shack. "Production and Use of a Lenticular Hartmann Screen". In: *Journal of the Optical Society of America* 61 (1971), pp. 656–661.

[40] Roberto Ragazzoni. "Pupil plane wavefront sensing with an oscillating prism". In: *Journal of Modern Optics* 43.2 (Feb. 1996), pp. 289–293. DOI: 10.1080/09500349608232742.

[41] Simone Esposito, Orla Feeney, and Armando Riccardi. "Laboratory test of a pyramid wavefront sensor". In: *Adaptive Optical Systems Technology*. Ed. by Peter L. Wizinowich. Vol. 4007. International Society for Optics and Photonics. SPIE, 2000, pp. 416–422. DOI: 10.1117/12.390322. URL: https://doi.org/10.1117/12.390322.

[42] S. Thomas et al. "Comparison of centroid computation algorithms in a Shack-Hartmann sensor". In: 371.1 (Sept. 2006), pp. 323–336. DOI: 10.1111/j.1365-2966.2006.10661.x.

[43] E. Pinna. "Applicazione del sensore a piramide alla misura di discontinuità del fronte d'onda". M.Sc. thesis. Firenze, Italia: Università degli Studi di Firenze, 2003.

[44] Lisa A. Poyneer et al. "The use of a high-order MEMS deformable mirror in the Gemini Planet Imager". In: *MEMS Adaptive Optics V*. Ed. by Scot S. Olivier, Thomas G. Bifano, and Joel A. Kubby. Vol. 7931. International Society for Optics and Photonics. SPIE, 2011, p. 793104. DOI: 10.1117/12.876496. URL: https://doi.org/10.1117/12.876496.

[45] P.-Y. Madec. "Overview of deformable mirror technologies for adaptive optics and astronomy". In: *Adaptive Optics Systems III*. Ed. by Brent L. Ellerbroek, Enrico Marchetti, and Jean-Pierre Véran. Vol. 8447. International Society for Optics and Photonics. SPIE, 2012, p. 844705. DOI: 10.1117/12.924892. URL: https://doi.org/10.1117/12.924892.

[46] P.-Y. Madec. "Control techniques". In: *Adaptive Optics in Astronomy*. Ed. by François Roddier. Cambridge: Cambridge University Press, 1999, p. 131.

[47] R. Penrose. "A generalized inverse for matrices". In: *Proceedings of the Cambridge Philosophical Society* 51.3 (July 1955), pp. 406–413. DOI: 10.1017/S0305004100030401.

[48] G. H. Golub and C. Reinsch. "Singular value decomposition and least squares solutions". In: *Numerische Mathematik* 14.5 (Apr. 1970), pp. 403–420. ISSN: 0945-3245. DOI: 10.1007/BF02163027. URL: https://doi.org/10.1007/BF02163027.

[49] Per Christian Hansen. "The truncated SVD as a method for regularization". In: *BIT Numerical Mathematics* 27.4 (Dec. 1987), pp. 534–553. ISSN: 1572-9125. DOI: 10.1007/BF01937276. URL: https://doi.org/10.1007/BF01937276.

[50] Francois J. Rigaut, Jean-Pierre Veran, and Olivier Lai. "Analytical model for Shack-Hartmann-based adaptive optics systems". In: *Adaptive Optical System Technologies*. Ed. by Domenico Bonaccini and Robert K. Tyson. Vol. 3353. Society of Photo-Optical Instrumentation Engineers (SPIE) Conference Series. Sept. 1998, pp. 1038–1048. DOI: 10.1117/12.321649.

[51] Carlos M. Correia and Joel Teixeira. "Anti-aliasing Wiener filtering for wave-front reconstruction in the spatial-frequency domain for high-order astronomical adaptive-optics systems". In: *Journal of the Optical Society of America A* 31.12 (Dec. 2014), p. 2763. DOI: 10.1364/JOSAA.31.002763. arXiv: 1410.6055 [astro-ph.IM].

[52] T. Sean Ross. "Limitations and applicability of the Maréchal approximation". In: 48.10 (Mar. 2009), p. 1812. DOI: 10.1364/AO.48.001812.

[53] J. M. Beckers. "Increasing the Size of the Isoplanatic Patch with Multiconjugate Adaptive Optics". In: *Very Large Telescopes and their Instrumentation, Volume 2*. Ed. by M. -H. Ulrich. Vol. 30. European Southern Observatory Conference and Workshop Proceedings. Oct. 1988, p. 693.

[54] Simone Esposito. "Introduction to Multi-Conjugate Adaptive Optics systems". In: *Comptes Rendus Physique* 6.10 (Dec. 2005), pp. 1039–1048. DOI: 10.1016/j.crhy.2005.11.016.

[55] M. Tallon and R. Foy. "Adaptive telescope with laser probe: isoplanatism and cone effect." In: 235 (Aug. 1990), pp. 549–557.

[56] Roberto Ragazzoni, Enrico Marchetti, and François Rigaut. "Modal tomography for adaptive optics". In: 342 (Feb. 1999), pp. L53–L56.

[57] François Rigaut et al. "GeMS: first on-sky results". In: *Adaptive Optics Systems III*. Ed. by Brent L. Ellerbroek, Enrico Marchetti, and Jean-Pierre Véran. Vol. 8447. Society of Photo-Optical Instrumentation Engineers (SPIE) Conference Series. July 2012, 84470I, p. 84470I. DOI: 10.1117/12.927061.

[58] François Rigaut et al. "MAVIS conceptual design". In: *Ground-based and Airborne Instrumentation for Astronomy VIII*. Ed. by Christopher J. Evans, Julia J. Bryant, and Kentaro Motohara. Vol. 11447. Society of Photo-Optical Instrumentation Engineers (SPIE) Conference Series. Dec. 2020, 114471R, 114471R. DOI: 10.1117/12.2561886.

[59] Jeffrey Crane et al. "NFIRAOS adaptive optics for the Thirty Meter Telescope". In: *Adaptive Optics Systems VI*. Ed. by Laird M. Close, Laura Schreiber, and Dirk Schmidt. Vol. 10703. Society of Photo-Optical Instrumentation Engineers (SPIE) Conference Series. July 2018, 107033V, p. 107033V. DOI: 10.1117/12.2314341.

[60] Paolo Ciliegi et al. “MAORY/MORFEO at ELT: general overview up to the preliminary design and a look towards the final design”. In: *Adaptive Optics Systems VIII*. Ed. by Laura Schreiber, Dirk Schmidt, and Elise Vernet. Vol. 12185. Society of Photo-Optical Instrumentation Engineers (SPIE) Conference Series. Aug. 2022, 1218514, p. 1218514. DOI: 10.1117/12.2628969.

[61] E. Vernet et al. “ELT M4 — The Largest Adaptive Mirror Ever Built”. In: *The Messenger* 178 (Dec. 2019), pp. 3–4. DOI: 10.18727/0722-6691/5162.

[62] Lorenzo Busoni et al. “MAORY/MORFEO at ELT: preliminary design of the adaptive optics subsystem”. In: *Adaptive Optics Systems VIII*. Ed. by Laura Schreiber, Dirk Schmidt, and Elise Vernet. Vol. 12185. Society of Photo-Optical Instrumentation Engineers (SPIE) Conference Series. Aug. 2022, 121854R, 121854R. DOI: 10.1117/12.2629606.

[63] Valentina Viotto et al. “MATTO: Multi-conjugate Adaptive Techniques Test Optics”. In: *Adaptive Optics for Extremely Large Telescopes (AO4ELT7)*. June 2023, 63, p. 63. DOI: 10.13009/AO4ELT7-2023-065.

[64] Sylvain Oberti et al. “Super-resolution wavefront reconstruction”. In: 667, A48 (Nov. 2022), A48. DOI: 10.1051/0004-6361/202243954. arXiv: 2208.12052 [astro-ph.IM].

[65] C. Selmi et al. “PLICO: a framework for Adaptive Optics laboratory experiments”. In: Adaptive Optics for Extremely Large Telescopes 7th Edition. 2023.

[66] F. Rossi, A. Puglisi, and G. Agapito. *SPECULA: Documentation*. https://specula.readthedocs.io/en/latest/. INAF–Osservatorio Astrofisico di Arcetri. Accessed: 28 Oct 2025. 2025.

[67] *PLICO Repository on GitHub*. https://github.com/ArcetriAdaptiveOptics/plico.

[68] *SPECULA Repository on GitHub*. https://github.com/ArcetriAdaptiveOptics/SPECULA.

[69] G. Agapito, A. Puglisi, and S. Esposito. “PASSATA: object oriented numerical simulation software for adaptive optics”. In: *Adaptive Optics Systems V*. Ed. by Enrico Marchetti, Laird M. Close, and Jean-Pierre Véran. Vol. 9909. Society of Photo-Optical Instrumentation Engineers (SPIE) Conference Series. July 2016, 99097E, 99097E. DOI: 10.1117/12.2233963. arXiv: 1607.07624 [astro-ph.IM].

[70] Advanced Microoptic Systems Gmbh. *AMUS Website*. https://amus.de/index.html.

[71] I. H. Malitson. “Interspecimen Comparison of the Refractive Index of Fused Silica∗,†”. In: *J. Opt. Soc. Am.* 55.10 (Oct. 1965), pp. 1205–1209. DOI: 10.1364/JOSA.55.001205. URL: https://opg.optica.org/abstract.cfm?URI=josa-55-10-1205.

[72] Yiqian Yang, Andrew Forbes, and Liangcai Cao. “A review of liquid crystal spatial light modulators: devices and applications”. In: *Opto-Electronic Science* 2.8 (2023), pp. 230026-1-230026–29. ISSN: 2097-0382. DOI: 10.29026/oes.2023.230026. URL: https://www.oejournal.org/oes/en/article/doi/10.29026/oes.2023.230026.

[73] Deng-Ke Yang and Shin-Tson Wu. *Fundamentals of liquid crystal devices*. John Wiley & Sons, 2014.

[74] A. A Pushkina et al. “Comprehensive model and performance optimization of phase-only spatial light modulators”. In: *Measurement Science and Technology* 31.12, 125202 (Dec. 2020), p. 125202. DOI: 10.1088/1361-6501/aba56b. arXiv: 2005.01561 [physics.optics].

[75] Meadowlark Optics. *User Manual XY Phase Series Spatial Light Modulatos With PCIe Controller*. Version Rev. 1.07. Meadowlark Optics, Inc. 52 pp.

[76] Joseph W. Goodman. *Introduction to Fourier optics*. 1995.

[77] A. Lizana et al. “Influence of the incident angle in the performance of Liquid Crystal on Silicon displays”. In: *Optics Express* 17.10 (May 2009), p. 8491. DOI: 10.1364/OE.17.008491.

[78] A. Márquez et al. “Mueller-Stokes characterization and optimization of a liquid crystal on silicon display showing depolarization”. In: *Optics Express* 16.3 (Jan. 2008), p. 1669. DOI: 10.1364/OE.16.001669.

[79] Justin E. Wolfe and Russell A. Chipman. “Polarimetric characterization of liquid-crystal-on-silicon panels”. In: 45.8 (Mar. 2006), pp. 1688–1703. DOI: 10.1364/AO.45.001688.

[80] Ignacio Moreno et al. “Diffraction efficiency of stepped gratings using high phase-modulation spatial light modulators”. In: *Optics and Lasers in Engineering* 126, 105910 (Mar. 2020), p. 105910. DOI: 10.1016/j.optlaseng.2019.105910.

[81] A. Lizana et al. “Time fluctuations of the phase modulation in a liquid crystal on silicon display: characterization and effects in diffractive optics”. In: *Opt. Express* 16.21 (Oct. 2008), pp. 16711–16722. DOI: 10.1364/OE.16.016711. URL: https://opg.optica.org/oe/abstract.cfm?URI=oe-16-21-16711.

[82] Wynn Improso, Giovanni Tapang, and Caesar Saloma. “Suppression of Zeroth-Order Diffraction in Phase-Only Spatial Light Modulator”. In: May 2019, pp. 1–30. ISBN: 978-3-030-12691-9. DOI: 10.1007/978-3-030-12692-6_1.

[83] Edoardo Bellone de Grecis and Paul Rouquette. “Characterization of a spatial light modulator for MORFEO and HARMONI adaptive optics test devices”. In: *Adaptive Optics Systems IX*. Ed. by Kathryn J. Jackson, Dirk Schmidt, and Elise Vernet. Vol. 13097. International Society for Optics and Photonics. SPIE, 2024, p. 130975D. DOI: 10.1117/12.3019084. URL: https://doi.org/10.1117/12.3019084.

[84] Jean-Baptiste Le Bouquin et al. "Characterization of ALPAO deformable mirrors for the NAOMI VLTI Auxiliary Telescopes adaptive optics". In: *Adaptive Optics Systems VI*. Ed. by Laird M. Close, Laura Schreiber, and Dirk Schmidt. Vol. 10703. International Society for Optics and Photonics. SPIE, 2018, p. 1070371. DOI: 10.1117/12.2313442. URL: https://doi.org/10.1117/12.2313442.

[85] T. G. Bifano and J. B. Stewart. "High-speed wavefront control using MEMS micromirrors". In: *Target-in-the-Loop: Atmospheric Tracking, Imaging, and Compensation II*. Ed. by Michael T. Valley and Mikhail A. Vorontsov. Vol. 5895. International Society for Optics and Photonics. SPIE, 2005, 58950Q. DOI: 10.1117/12.619355. URL: https://doi.org/10.1117/12.619355.

[86] Junyu Zou et al. "Fast-Response Liquid Crystal for Spatial Light Modulator and LiDAR Applications". In: *Crystals* 11.2 (2021). ISSN: 2073-4352. DOI: 10.3390/cryst11020093. URL: https://www.mdpi.com/2073-4352/11/2/93.

[87] Mike Pivnenko, Kun Li, and Daping Chu. "Sub-millisecond switching of multi-level liquid crystal on silicon spatial light modulators for increased information bandwidth". In: *Opt. Express* 29.16 (Aug. 2021), pp. 24614–24628. DOI: 10.1364/OE.429992. URL: https://opg.optica.org/oe/abstract.cfm?URI=oe-29-16-24614.

[88] Analog Devices. *Data Sheet AD8541/AD8542/AD8544*. Analog Devices, Inc. 18 pp.

[89] Armando Riccardi, Marco Xompero, and Lorenzo Busoni. "Fitting error analysis for the VLT deformable secondary mirror". In: *Advances in Adaptive Optics II*. Ed. by Brent L. Ellerbroek and Domenico Bonaccini Calia. Vol. 6272. Proc. SPIE. 2006, 627240. DOI: 10.1117/12.673517. URL: https://www.spiedigitallibrary.org/conference-proceedings-of-spie/6272/1/Fitting-error-analysis-for-the-VLT-deformable-secondary-mirror/10.1117/12.673517.full.

[90] C.P. Robert and G. Casella. *Monte Carlo statistical methods*. Springer Verlag, 2004.

[91] Shuangzhe Liu. "Global Sensitivity Analysis: The Primer by Andrea Saltelli, Marco Ratto, Terry Andres, Francesca Campolongo, Jessica Cariboni, Debora Gatelli, Michaela Saisana, Stefano Tarantola". In: *International Statistical Review* 76 (Feb. 2008), pp. 452–452. DOI: 10.1111/j.1751-5823.2008.00062_17.x.

[92] Anne Costille et al. "HARMONI at ELT: designing a laser guide star wavefront sensors for the ELT". In: *Adaptive Optics Systems VIII*. Ed. by Laura Schreiber, Dirk Schmidt, and Elise Vernet. Vol. 12185. Society of Photo-Optical Instrumentation Engineers (SPIE) Conference Series. Aug. 2022, 121854L, p. 121854L. DOI: 10.1117/12.2627644. arXiv: 2207.08451 [astro-ph.IM].

[93] G. de Saint Salvy et al. "HARMONI at ELT: a telescope simulator for laser tomographic AO". In: *Adaptive Optics Systems VIII*. Ed. by Laura Schreiber, Dirk Schmidt, and Elise Vernet. Vol. 12185. Society of Photo-Optical Instrumentation Engineers (SPIE) Conference Series. Aug. 2022, 121856E, 121856E. DOI: 10.1117/12.2629301.

[94] Pierre Jouve et al. "HARMONI at ELT: full scale prototype of the laser guide star wavefront sensor". In: *Adaptive Optics Systems VIII*. Ed. by Laura Schreiber, Dirk Schmidt, and Elise Vernet. Vol. 12185. Society of Photo-Optical Instrumentation Engineers (SPIE) Conference Series. Aug. 2022, 121854M, p. 121854M. DOI: 10.1117/12.2627934.

[95] Romain Fetick et al. "PAPYRUS: one year of on-sky operations". In: *Adaptive Optics for Extremely Large Telescopes (AO4ELT7)*. June 2023, 13, p. 13. DOI: 10.13009/AO4ELT7-2023-014.

[96] Edoardo Bellone de Grecis, Giulia Carlà, and Lorenzo Busoni. "Development of test devices for the validation of MORFEO's reconstruction and control algorithms". In: *Adaptive Optics for Extremely Large Telescopes (AO4ELT7)*. June 2023, 92, p. 92. DOI: 10.13009/AO4ELT7-2023-094.

[97] Marco Bonaglia et al. "MORFEO: status of the low-order and reference (LOR) NGS WFS module". In: *Adaptive Optics Systems IX*. Ed. by Kathryn J. Jackson, Dirk Schmidt, and Elise Vernet. Vol. 13097. International Society for Optics and Photonics. SPIE, 2024, p. 1309750. DOI: 10.1117/12.3019174. URL: https://doi.org/10.1117/12.3019174.

[98] Romain J. L. Fétick et al. "PAPYRUS: from an adaptive optics system to an instrumental platform". In: *Adaptive Optics Systems IX*. Ed. by Kathryn J. Jackson, Dirk Schmidt, and Elise Vernet. Vol. 13097. International Society for Optics and Photonics. SPIE, 2024, p. 1309716. DOI: 10.1117/12.3019758. URL: https://doi.org/10.1117/12.3019758.

[99] Alexis Carlotti et al. "On-sky demonstration at Palomar Observatory of the near-IR, high-resolution VIPA spectrometer". In: *Ground-based and Airborne Instrumentation for Astronomy IX*. Ed. by Christopher J. Evans, Julia J. Bryant, and Kentaro Motohara. Vol. 12184. Society of Photo-Optical Instrumentation Engineers (SPIE) Conference Series. Aug. 2022, 121841I, p. 121841I. DOI: 10.1117/12.2628937. arXiv: 2305.19736 [astro-ph.IM].

[100] Mahawa Cisse et al. "PAPYRUS: Second stage adaptive optics with a vector Zernike wavefront sensor". In: *Adaptive Optics for Extremely Large Telescopes (AO4ELT7)*. June 2023, 58, p. 58. DOI: 10.13009/AO4ELT7-2023-060.